Light-Controlled Nanostructuring of Plasmonic Metasurfaces

Ivan Shutsko

2023

Light-Controlled Nanostructuring of Plasmonic Metasurfaces

Dissertation
for attaining the degree of a
Doctor of Engineering
in the School of
Electrical, Information and Media Engineering
at the University of Wuppertal

by

M. Sc. Ivan Shutsko

Referee: Prof. Dr.-Ing. Patrick Görrn

Co-referee: Prof. Dr. rer. nat. Thomas Riedl

Date of the oral examination: 12.01.2024

Acknowledgements

I would like to express my heartfelt gratitude and appreciation to the people who have played a significant role in completing my Ph.D. thesis.

First and foremost, I would like to express my sincere gratefulness to my supervisor, Prof. Patrick Görrn. Your guidance and scientific expertise have been exceptional. Your commitment to academic excellence, profound insights, and constant invaluable feedback have shaped my research work and significantly improved the quality of the results presented in the current thesis. I am also very grateful to Prof. Patrick Görrn for his time and efforts in reviewing this dissertation. I also thank Prof. Thomas Riedl for our productive collaboration on research projects over the years and for his valuable feedback during my thesis evaluation.

To the colleagues who have become my friends, thank you all for your help throughout this journey. Your brainstorming sessions, intense scientific discussions, and shared experiences have enriched my research and made my workflow more enjoyable. Specifically, I would like to express my profound thanks to my colleague Maximilian Buchmüller for his invaluable support and our fruitful collaboration on scientific papers over the past years. Furthermore, I would like to thank the European Research Council and the Chair of Large Area Optoelectronics, which financially supported my research and made it possible to work on fascinating scientific projects.

I would like to extend my most profound appreciation to my family. Their love, patience, and understanding have been my constant source of strength throughout this challenging endeavor. Their belief in me and constant encouragement propelled me forward, even during moments of self-doubt. I am truly grateful for their sacrifices, understanding, and endless support.

"Everybody can handle order, but only a genius can master chaos."

Albert Einstein

Contents

Chapter I Introduction

Optical structures have been used to manipulate light propagation since the 19th century. These structures are typically constructed using either ordered or disordered arrangements of refractive and diffractive building elements. A common challenge with most disordered optical structures is achieving reliable reproducibility[1]. This is due to the fact that the disordered arrangement of their building elements makes it difficult to predict and control their optical properties. As a result, extensive characterization processes are required, which can be time-consuming and costly[2]. Moreover, disordered structures typically lack long-range order compared to ordered structures, which can result in the lack of a sharp and predictable optical response. Nevertheless, recent research has unveiled a fascinating aspect: certain disordered structures possess a hidden short-range order and exhibit unique optical properties absent in both ordered and disordered structures[3–5]. This fact opens new ways for designing and fabricating novel materials with enhanced optical functionality, giving rise to a class of structures known as structures of engineered disorder[4].

Over millions of years, nature fine-tuned materials and structures through natural selection, resulting in nano- and microstructures optimized for efficient light-matter interactions. One remarkable manifestation of this are structures of engineered disorder[5] found in various natural systems. For instance, certain flowers possess disordered nanostructures that produce visual signals particularly attractive to bees[6]. The vibrant colors of the plumage of many birds are not solely the result of pigmentation but rather due to the short-range order in the arrangement of their spongy keratin in the feather barbs[7]. Similarly, the white scales of some beetles exhibit a disordered network of chitin filaments that enables bright white scattering using a minimal amount of

material and relatively low refractive index contrast[8]. In contrast, the wings of butterflies with distributed disordered nanoholes appear black and can capture sunlight across a broad spectral and angular range[9].

Studying these natural examples can provide valuable insights for designing and fabricating novel materials. Inspired by natural examples[8], researchers have applied the concept of engineered disorder to explore a range of fascinating optical phenomena, such as structural coloring[5], material's visual appearance[10], and even induction of material transparency[11]. Moreover, the engineered disorder is widely applied in planar optics to design the features inside reciprocal space for the dielectric[5,12–14] or plasmonic[1,15–18] metasurface, enabling precise manipulation of light amplitude, phase, and polarization at nanoscale interaction lengths. This allows for significant improvement in the performance of optoelectronic devices. For instance, the engineered disorder has been shown to enable efficient management and harvesting of sunlight in solar cells. The absorption of 66.5% for the spectral range of 400 to 1050 nm was achieved in a 1 μm free-standing silicon layers using surface texturing based on engineered disordered patterns[19]. Furthermore, the experimental enhancement of light extraction from light-emitting devices was achieved by significantly reducing losses due to total internal reflection. This was accomplished using dielectric nanoparticles arranged spatially to introduce a dominant scattering direction, facilitating the formation of ring-shaped features within the reciprocal space[20]. Some laser structures were also implemented using engineered disorder[21]. The first experiments showed very promising results. The disordered disk pattern was transferred on the top surface of the active region of the quantum cascade laser. Although long-range order was suppressed, the pattern still exhibits a photonic band gap. Moreover, the structure demonstrated a low lasing

threshold and angular emission bistability, which can be controlled by the size and position of the scatters of disordered structures. Next, such optical structures also found their application in the field of displays. Recently, the large-area holographic display with a wide viewing angle has been introduced based on an engineered disorder of photon sieve[22].

Particular emphasis has recently been put on the sensitive optical response of structures with the engineered disorder. The disordered network of subwavelength scatterers exhibits strong angular sensitivity for the illuminating waves, enabling a sharp change of the radiation profile in near and far-field regions[23]. Moreover, the plasmonic structures with features of engineered disorder fabricated via low-cost and immediate synthesis make it possible to produce a highly reproducible surface-enhanced Raman scattering response over the centimeter length scale[1].

As can be seen, extensive research on the disordered engineered structure has just begun but already shows a variety of breakthroughs in designing state-of-the-art optical devices, gradually erasing the distinction between order and disorder[3,5]. Considering the vast inspiration drawn from applications, developing robust and cost-efficient fabrication methods for such structures has become the primary focus in the field of disorder engineering.

At first glance, disorder intuitively implies a more facile way of technological implementation due to the high tolerance to fabrication imperfection in contrast to the optical structure possessing an order in the distribution of building elements. However, the optical response of engineered disordered structures also strongly depends on the position accuracy of building elements. In fact, structures of engineered disorder are even more challenging to fabricate due to the high complexity of the corresponding design

routines and complex numerical computation[24–26]. Thus, developing robust and scalable fabrication methods for these structures is critical for unlocking their full potential in future optical applications.

Disorder engineering can be achieved through top-down or bottom-up approaches. Top-down methods[27], such as electron beam or focused ion beam lithography, can produce high-quality structures with precise features[28] and accurate positioning of building elements[29]. However, these methods have limitations in terms of resolution, scalability, and material range. Furthermore, replicating building elements over a large area is also restricted as it can result in the unintended formation of order and corresponding Bragg peaks due to scalability constraints. While top-down[15] or hybrid[13] methods are still commonly used[4], bottom-up approaches are better suited for robust, large-scale, cost-effective fabrication.

The scientific investigation of engineered disorder in optics is still in its early stages, with limited research and a dearth of well-established, robust bottom-up fabrication methods. Developing such methods is challenging, as it requires precise control over several parameters, including composition, size, shape, and spatial arrangement. Only a few research groups have successfully demonstrated the bottom-up fabrication of structures of engineered disorder using self-assembly[30], spinodal dewetting[31], or printing[32] approaches. Despite these advances, achieving precise in situ control of features inside the reciprocal space of disordered structures remains a significant challenge.

Using plasmonic nanostructures[33] as building blocks holds significant interest for optical structures as it can significantly influence light propagation properties[27]. By employing plasmonic nanostructures, researchers achieved remarkable capabilities such as enabling negative refraction[34], achieving aberration-free imaging[35], and exerting control over

surface plasmon waves in the near-field regime[36]. Moreover, plasmonic nanostructures also overcome diffraction limits, allowing precise manipulation of light at the nanometer scale. These unique properties make plasmonic nanostructures highly advantageous for various applications, including light harvesting[37], next-generation photonics circuits[38], optical computing[39], and sensing[40].

It is essential to carefully control the morphology of the plasmonic nanostructure linked to its reciprocal space when constructing a functional plasmonic metasurface to achieve the desired optical properties. The reciprocal space reflects valuable information about the interaction of light with the plasmonic nanostructure. The specific disordered arrangement of building elements, their shape, and size in real space correspond to certain diffraction patterns and characteristic features inside the reciprocal space.

Controlled manipulation of silver-based plasmonic nanostructure morphology was the main focus in previous works[41–44]. This is done by modifying either adhesion to a substrate or the ambient atmosphere. The surface adhesion of the substrate can be modified by light before the deposition via wet chemical synthesis of plasmonic nanostructures, enabling silver patterning.[44] During deposition, the adhesion of silver nanoparticles can be increased by exposure to visible light[41], energetically favoring their further growth. After growth, silver nanoparticles exposed to visible light in the oxidizing atmosphere showed an enhancement of adhesion to the polymer surface. In this case, the coalescence of silver nanoparticles on the polymer surface can be tuned by adjusting the exposure dose. This enables a new type of photolithography by precisely tuning the morphology of silver nanoparticles. Recently, it was shown that control of the nanoparticle morphology can not only be achieved by surface treatment and tuning of the substrate adhesion but also by direct exposure to light during growth[43].

This thesis presents a facile, and scalable bottom-up approach to fabricating plasmonic metasurfaces with engineered disorder induced and controlled by light. The electroless deposition technique[43–45] serves as the foundation for the fabrication process. The metasurfaces are formed based on plasmonic nanoparticles growing from a solution under light-controlled deposition. In this way, the disorder of nanoparticles is induced and can be tuned by different growth scenarios implemented by tailoring both the key light parameters and the electromagnetic environment. In the end, the information regarding the optical properties of the used light source and the electromagnetic environment in which nanoparticles are grown is permanently stored in the form of nanoparticle morphology and their distribution over a surface. The great versatility of excitation photonic and plasmonic schemes, in conjunction with growth parameters, provides ample opportunities for the tailored design of sharp[46] and broad[47] features inside the reciprocal space. Remarkably, the formation of sharp characteristics inside the reciprocal space of the metasurface serves as a basis for creating optical refractive index sensors with performance comparable with state-of-the-art optical structures fabricated using top-down approaches[48]. Moreover, this method can be extended to fabricating the periodic nanoparticle structures on top of the thin film resonators[45] or waveguides. The suggested mechanism is based on the superposition of scattered and incident waves similar to the laser-induced periodic surface structures known as LIPSS[49–51].

The thesis is structured as follows: Chapter I serves as the introduction, providing context for the research topic and highlighting current challenges in the field. Chapter II gives the theoretical basis and mathematical tools for studying the fabricated plasmonic metasurfaces, including the concept of hyperuniformity as a direct manifestation of the induced engineered disorder. Chapter III explains the methods for fabricating,

characterizing, and simulating plasmonic metasurfaces with engineered disorder. Chapter IV presents the results divided into four parts: the first part focuses on engineering features inside the reciprocal space, including the fabrication of metasurfaces with hyperuniform features; the second part presents the first experimental demonstration of an optical refractive index sensor based on exploring sharp characteristics inside the reciprocal space; and the third part explores the versatility of this approach by fabricating a hybrid optical structure with well-ordered plasmonic elements, enabling enhanced interaction between plasmonic and dielectric parts. In the fourth part, surface plasmons assistant formation of the grating with the period close to the used wavelength is demonstrated.

Chapter II Fundamentals

This chapter is dedicated to the theoretical fundamentals needed to understand methods and results in the thesis at hand. Optics fundamentals are presented in the first section. Subsequently, theoretical basics on nanoparticle growth and alignment with light are provided. In the end, engineering based on disordered structures is discussed, and the concept of hyperuniformity is introduced.

2.1 Optics Fundamentals

Metal interaction with electromagnetic fields is described in a framework of Maxwell's equations. Maxwell's equations in macroscopic electromagnetism can be expressed as [33]:

$$\boldsymbol{\nabla} \cdot \boldsymbol{D} = \rho_{ext}, \tag{1.1a}$$

$$\boldsymbol{\nabla} \cdot \boldsymbol{B} = 0, \tag{1.1b}$$

$$\boldsymbol{\nabla} \times \boldsymbol{E} = -\frac{\partial \boldsymbol{B}}{\partial t}, \tag{1.1c}$$

$$\boldsymbol{\nabla} \times \boldsymbol{H} = \boldsymbol{J_{ext}} + \frac{\partial \boldsymbol{D}}{\partial t}, \tag{1.1d}$$

where $\boldsymbol{\nabla}$ stands for the Nabla operator, $\boldsymbol{D}$ for dielectric displacement, $\boldsymbol{E}$ for electric field, $\boldsymbol{H}$ for magnetic field, $\boldsymbol{B}$ for magnetic induction, ρ_{ext} for external charge density, and $\boldsymbol{J_{ext}}$ for current density. In this thesis, a vector is represented by a **bold** letter if no additional explanations or footnotes are provided. Equations (1.1a) to (1.1.d) are a system of coupled linear differential equations enabling the field superposition principle. Four macroscopic fields are connected via polarization $\boldsymbol{P}$ and magnetization $\boldsymbol{M}$ through the material equations:

$$\boldsymbol{D} = \varepsilon_o \boldsymbol{E} + \boldsymbol{P}, \tag{1.2a}$$

$$\boldsymbol{H} = \frac{1}{\mu_0} \boldsymbol{B} - \boldsymbol{M}, \tag{1.2b}$$

where ε_0 and μ_0 are the electric and magnetic permeability of vacuum, respectively. For the case of linear, isotropic, and non-magnetic media, (1.2a) and (1.2b) can be rewritten as:

$$\boldsymbol{D} = \varepsilon_0 \varepsilon \boldsymbol{E}, \tag{1.2c}$$

$$\boldsymbol{B} = \mu_0 \boldsymbol{H}, \tag{1.2d}$$

where ε stands for relative permittivity or dielectric constant, which, in general, is a complex frequency-dependent value $\varepsilon(\omega) = \varepsilon' + i\varepsilon''$. The dielectric constant is linked to the refractive index via $n = \sqrt{\varepsilon} = n' + in''$. The real part ($n'$) indicates the phase velocity v_p via $v_p = \frac{c_0}{n'}$ with c_0 as a vacuum speed of light, while the imaginary part (n'') is the extinction coefficient, which is positive for an absorbing medium, zero for a transparent medium, and negative for a medium with optical gain. The extinction coefficient is an important parameter to describe the exponential decay of light intensity in a medium like $I(z) = I_0 e^{-\alpha z}$ (Beer's law)[52]. The absorption coefficient α is defined as $\alpha = 2n''\omega/c_0$.

2.1.1 Localized Surface Plasmon Resonance

Optical properties of metals are commonly derived from a plasma model, where gas of free electrons moves against fixed positive ion cores. The quanta of the charge oscillation are called plasmons. The electrons oscillate in response to the applied electromagnetic field with the time phasor $e^{-i\omega t}$: $\boldsymbol{E} = \boldsymbol{E_0} e^{-i\omega t}$. Their motion is attenuated via collisions with a characteristic collision frequency of $\gamma = 1/\tau$, where τ is the relaxation time of the free electron gas. The motion differential equation of an effective optical mass m_e of each electron can be expressed as[33]:

$$m_e \ddot{\boldsymbol{r}} + m_e \gamma \dot{\boldsymbol{r}} + e\boldsymbol{E} = 0, \tag{1.3}$$

where e is the elementary charge. The solution of equation (1.3) is:

$$\boldsymbol{r}(t) = \frac{e}{m_e(\omega^2 + i\gamma\omega)}\boldsymbol{E}(t). \tag{1.4}$$

By substituting the displacement $\boldsymbol{r}$ by macroscopic polarization, defined as $\boldsymbol{P} = -N_e e\boldsymbol{r}$, equation (1.4) can be rewritten as:

$$\boldsymbol{P} = -\frac{N_e e^2}{m_e(\omega^2 + i\gamma\omega)}\boldsymbol{E}(t), \tag{1.5}$$

where N_e is the electron density. By using equation (1.2a), (1.5) is rewritten then as:

$$\boldsymbol{D} = \varepsilon_o\left(1 - \frac{\omega_p^2}{\omega^2 + i\gamma\omega}\right)\boldsymbol{E}(t), \tag{1.6}$$

where $\omega_p = \frac{N_e e^2}{\varepsilon_0 m_e}$ is the plasma frequency of the free electron gas. The dielectric function of the free electron gas is:

$$\varepsilon(\omega) = 1 - \frac{\omega_p^2}{\omega^2 + i\gamma\omega}. \tag{1.7}$$

Equation (1.7) describes the reaction of electrons of a metal to an external time-harmonic electric field. Particularly, resonance oscillation of conduction electrons in metal nanoparticles induced by an external electromagnetic field leads to the emergence of resonance localized mode or localized surface plasmon (LSP) resonance (Figure 1). An effective restoring force is applied to driven electrons at the resonance, leading to field amplification inside and outside the nanoparticle. The curved surface of the nanoparticle allows exciting resonance by direct light illumination without the need for phase-matching conditions. Mathematically, the interaction between nanoparticles of radius R and the applied external electromagnetic field can be studied by a quasi-static approximation where the nanoparticle radius must be much lower than the wavelength of the incident electromagnetic wave (λ_0).

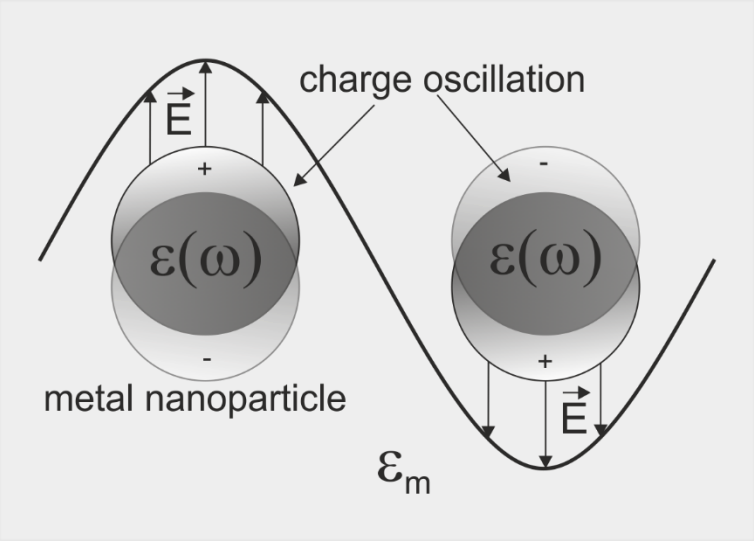

Figure 1: A metallic nanoparticle of radius R placed in the dielectric medium ε_m is excited by the external electromagnetic field. It is drawn according to reference[53].

In this case, the nanoparticle is considered an oscillating electric dipole. The total electric field scattered by a dipole is expressed as[54]:

$$E_{scat}(r,t) = e^{-i\omega t}\frac{e^{ikr}}{\boldsymbol{r}^3}(k^2\boldsymbol{r}\times(\boldsymbol{p}\times\boldsymbol{r}) + \frac{1-ik\boldsymbol{r}}{\boldsymbol{r}^2}[3\boldsymbol{r}(\boldsymbol{r}\cdot\boldsymbol{p}) - \boldsymbol{r}^2\boldsymbol{p}]), \qquad (1.8)$$

where $\boldsymbol{k}$ is a wave vector, $\boldsymbol{r}$ is a unit vector directed to the point of consideration, and $\boldsymbol{p}$ is a dipole moment defined through nanoparticle polarizability $\varkappa$ as[55]:

$$\varkappa = 4\pi R^3\frac{\varepsilon-\varepsilon_m}{\varepsilon+2\varepsilon_m}, \qquad (1.9)$$

$$\boldsymbol{p} = \varepsilon_o\varepsilon_m\varkappa\boldsymbol{E}. \qquad (1.10)$$

From expression (1.9), it can be seen that polarizability undergoes a resonant enhancement when $Re(\varepsilon) = -2\varepsilon_m$. At resonant frequency, the absorption is maximized, and the electric field near the nanoparticle's surface is significantly enhanced. Such resonant behavior of metallic nanoparticles is widely used in many optical devices, e.g., for developing highly sensitive chemical and biological sensors. In particular, silver and

gold nanoparticles (AgNPs and AuNPs) experience LSP resonance in the visible region of the spectrum. Moreover, AgNPs are particularly interesting due to their extraordinary ability of strong absorption and scattering of incident light. As a result, AgNPs can significantly enhance the efficiency of optoelectronic devices. In addition, silver exhibits the highest electrical and thermal conductivity among metals at room temperature. In Figure 2, the real part of the AgNP polarizability at different radii is displayed.

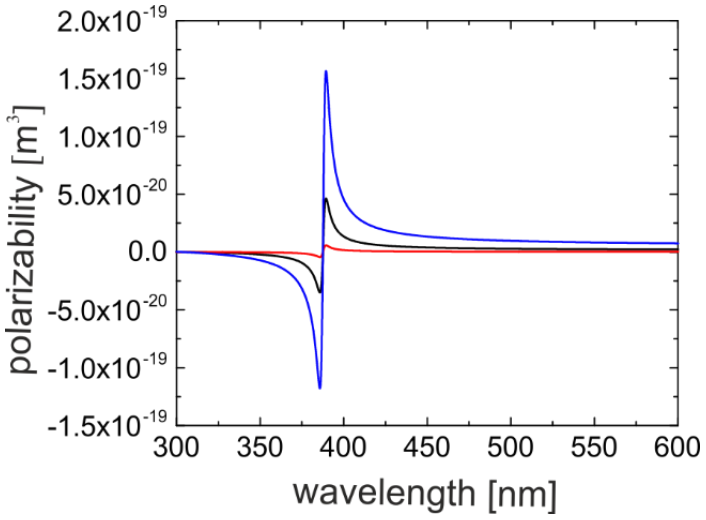

Figure 2: Real part of the polarizability of AgNPs with a radius of 25 nm, 50 nm, and 75 nm (red, black, and blue accordingly) placed in water ($\varepsilon_m \approx 1.776$) environment.

The wavelength at which LSP resonance takes place strongly depends on the size, shape, and electromagnetic environment[56] of the nanoparticle.

2.1.2 Delocalized Surface Plasmon Polaritons and Hybridization in Thin Metal Films

This section introduces a second fundamental excitation of plasmonics – delocalized surface plasmon polaritons (SPPs). SPPs are surface wave modes that propagate at the interface between a dielectric and metal[57]. They originate from the strong interaction

between light and metal-free electrons. SPPs offer strong field confinement and enhancement on metal surfaces[58]. In order to describe SPPs mathematically, wave equation is used. It can be shown[59] from Maxwell's equations that in the absence of external charges ($\rho_{ext} = 0$) and currents ($J_{ext} = 0$), the wave equstion can be expressed in the following form:

$$\boldsymbol{\nabla}^2\boldsymbol{E} - \frac{1}{c^2}\frac{\partial^2\boldsymbol{E}}{\partial t^2} = 0, \tag{1.11}$$

with the Laplace operator $\boldsymbol{\nabla}^2$, and $c = \frac{1}{\sqrt{\varepsilon\mu}} = \frac{c_o}{n}$, where n is the refractive index. By applying the phasor ansatz to equation (1.11), the time derivative is transformed into a multiplicative factor ($\partial/\partial t \rightarrow -i\omega$), enabling the rewriting of equation (1.11) in the form of the Helmholtz equation

$$\boldsymbol{\nabla}^2\boldsymbol{E} + k_0^2\varepsilon\boldsymbol{E} = 0, \tag{1.12}$$

where $k_0$is the wave vector. By defining the geometry as shown in Figure 3, a propagating wave can, in this case, be defined as $\boldsymbol{E}(x,y,z,t) = \boldsymbol{E}(z)e^{ik_x x}e^{-i\omega t}$ with the propagation constant in the x-direction $k_x = k_{spp}$.

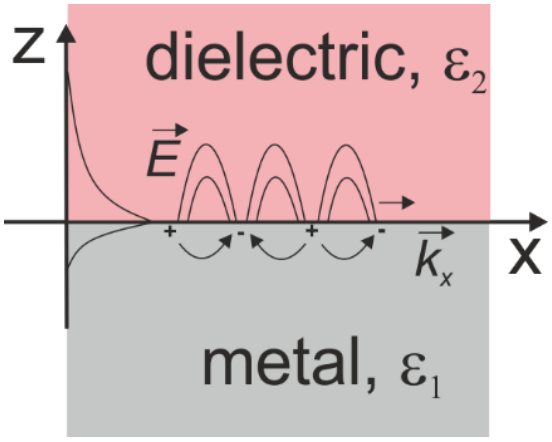

Figure 3: Schematic illustration of the dielectric-metal interface.

It is drawn according to reference[60].

Now, equation (1.12) can be rewritten as:

$$\frac{\partial^2 \boldsymbol{E}}{\partial z^2} + \left(k_0^2 \varepsilon - {k_{spp}}^2\right)\boldsymbol{E} = 0. \tag{1.13}$$

Equation (1.13) describes guided electromagnetic modes in waveguides. It can be shown that transverse magnetic (TM) modes have non-zero H_y, E_x, and E_z components. In detail, for $z > 0$:

$$H_y(\mathrm{z}) = A_2 e^{ik_{spp}x} e^{-k_{z2}z}, \tag{1.14a}$$

$$E_x(\mathrm{z}) = \mathrm{i}\, A_2 \frac{1}{\omega \varepsilon_0 \varepsilon_2} k_2 e^{ik_{spp}x} e^{-k_{z2}z}, \tag{1.14b}$$

$$E_z(\mathrm{z}) = -A_2 \frac{\beta}{\omega \varepsilon_0 \varepsilon_2} e^{ik_{spp}x} e^{-k_{z2}z}, \tag{1.14c}$$

and for $z < 0$:

$$H_y(\mathrm{z}) = A_1 e^{ik_{spp}x} e^{k_{z1}z}, \tag{1.15a}$$

$$E_x(\mathrm{z}) = -\mathrm{i}\, A_1 \frac{1}{\omega \varepsilon_0 \varepsilon_1} k_1 e^{ik_{spp}x} e^{-k_{z1}z}, \tag{1.15b}$$

$$E_z(\mathrm{z}) = -A_1 \frac{\beta}{\omega \varepsilon_0 \varepsilon_1} e^{ik_{spp}x} e^{-k_{z1}z}. \tag{1.15c}$$

Here, ε_1 describes the dielectric function of the metal where $\mathrm{Re}(\varepsilon_1) < 0$. k_{z1} and k_{z2} are the components of the wave vector perpendicular to the interface in the two media, which can be defined as[33]:

$$k_{z1}^2 = {k_{spp}}^2 - k_0^2 \varepsilon_1, \tag{1.16a}$$

$$k_{z2}^2 = {k_{spp}}^2 - k_0^2 \varepsilon_2. \tag{1.16b}$$

At the interface at $z = 0$, the tangential components of the electric and magnetic fields must be continuous, meaning that $A_1 = A_2$ and thus:

$$\frac{k_{z2}}{k_{z1}} + \frac{\varepsilon_2}{\varepsilon_1} = 0. \tag{1.17}$$

Combining (1.16 a,b) and (1.17), the dispersion relation of SPPs propagating at the

interface between the two dielectric-metal half-spaces can be derived:

$$k_{spp} = k_0 \sqrt{\frac{\varepsilon_1 \varepsilon_2}{\varepsilon_1 + \varepsilon_2}} = k_0 \cdot n_{eff}. \tag{1.18}$$

n_{eff} is the effective refractive index of the TM mode. Similar to the description above, it can be shown that for a transverse electric (TE) mode, the following expression can be obtained:

$$A_1(k_{z1} + k_{z2}) = 0. \tag{1.19}$$

Since the real part of the wave vectors must be larger than zero, the equation can only be fulfilled if $A_1 = 0$, meaning that $A_1 = A_2 = 0$. Therefore, no surface modes can exist for TE-polarized fields[33].

Figure 4 shows a dispersion curve, which provides a relation between momentum and frequency. At $\omega < \omega_p$, the permittivity of the metal ε_1 is real and negative. SPPs (Figure 4, red curve) follow photon characteristics and are close to the dispersion curve of the light line (Figure 4, green curve). Deviation from the light line means that the SPPs are confined to the metal surface and cannot be transformed into light (free photons), remaining in a "non-radiative" regime. Reciprocally, a phase-matching technique is needed to excite SPPs by light. For example, an attenuated total reflectance (ATR) setup with an integrated prism or grating can be used to gain corresponding momentum (Figure 4, black arrow). In this case, both the frequency and parallel momentum are conserved to excite the SPP (Figure 4, dashed green curve). As frequency increases, the SPP mode starts deviating firmly away from the light line asymptotically approaching the surface plasmon frequency $\omega_{sp} = \frac{w_p}{\sqrt{1+\varepsilon_2}}$. At this frequency, ε_1 equals ε_2 but with the opposite sign.

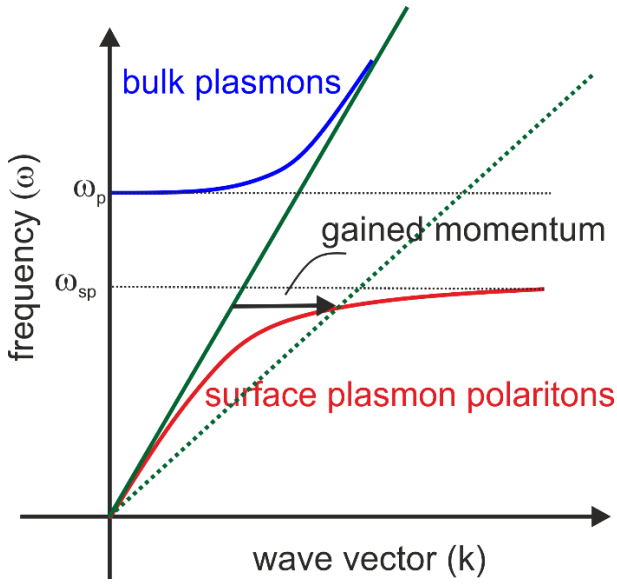

Figure 4: Dispersion relation of bulk plasmons and surface plasmon polaritons.

When $\omega > \omega_p$, ε_1 is real and positive. At this frequency, the wave propagates in the way as it travels in the ordinary positive dielectric medium. The upper blue branch of Figure 4 describes charge oscillations inside a volume of metal (bulk plasmons) obeying the following dispersion relation: $\omega^2 = {\omega_p}^2 + (ck)^2$. At plasma frequency ($\omega_p$), longitudinal collective oscillations of the conduction electrons inside the metal can be excited.

Until now, the focus has been on considering the surface modes between two infinitely large half-spaces. As of now, the focus will shift to an asymmetric multilayer system where a thin metal film with a finite thickness d is placed between two dielectrics with corresponding dielectric functions ε_2 and ε_3 (Figure 5a). In such a system, the SPPs can be excited at every single interface. By decreasing the film thickness, the evanescent fields of SPPs on both interfaces start overlapping, leading to their coupling. That results in hybridization and formation of symmetric and antisymmetric eigenmodes[57]. Figure 5a shows corresponding magnetic field strengths. Symmetric eigenmodes show less

penetration into the metal film, leading to lower Ohmic losses and a longer propagation length than for SPPs. Therefore, symmetric eigenmodes are termed long-range SPPs or LRSPPs[61–65]. On the contrary, antisymmetric eigenmodes or short-range SPPs[63,66–69] (or SRSPPs) show higher absorption and shorter propagation length.

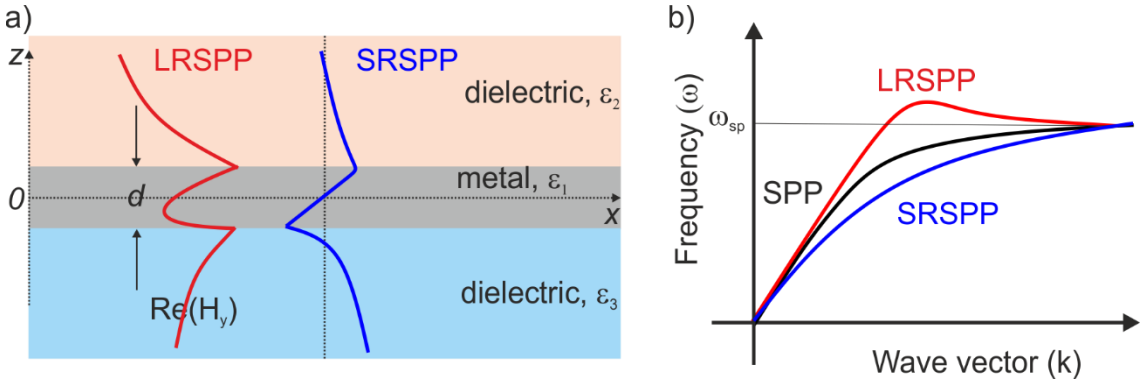

Figure 5: Schematic illustration of studied multilayers where hybridization occurs: a) H_y field distributions for short and long-range surface polaritons; b) dispersion relations of short and long-range surface polaritons.

Next, the dispersion relations for corresponding modes will be derived. First, the field's components for TM modes at $z > d/2$ are expressed as[33,57,65]:

$$H_y(\mathrm{z}) = Ae^{ik_{spp}}e^{-k_2 z}, \tag{1.20a}$$

$$E_x(\mathrm{z}) = -\,i\,A\frac{1}{\omega\varepsilon_0\varepsilon_2}k_2 e^{ik_{spp}x}e^{k_2 z}, \tag{1.20b}$$

$$E_z(\mathrm{z}) = -A\frac{k_{spp}}{\omega\varepsilon_0\varepsilon_2}e^{ik_{spp}x}e^{k_2 z}. \tag{1.20c}$$

Similarly, for $z < -d/2$:

$$H_y(\mathrm{z}) = Ae^{ik_{spp}x}e^{-k_3 z}, \tag{1.21a}$$

$$E_x(\mathrm{z}) = -\,i\,A\frac{1}{\omega\varepsilon_0\varepsilon_3}k_2 e^{ik_{spp}x}e^{k_3 z}, \tag{1.21b}$$

$$E_z(\mathrm{z}) = -A\frac{k_{spp}}{\omega\varepsilon_0\varepsilon_3}e^{ik_{spp}x}e^{k_3 z}. \quad (1.21c)$$

Furthermore, for the metal film region $-d/2 < z < d/2$, the field components are:

$$H_y(\mathrm{z}) = Ce^{ik_{spp}x}e^{k_1 z} + De^{ik_{spp}x}e^{-k_1 z}, \quad (1.22a)$$

$$E_x(\mathrm{z}) = -iC\frac{1}{\omega\varepsilon_0\varepsilon_1}k_1 e^{ik_{spp}x}e^{k_1 z} + iD\frac{1}{\omega\varepsilon_0\varepsilon_1}k_1 e^{ik_{spp}x}e^{-k_1 z}, \quad (1.22b)$$

$$E_z(\mathrm{z}) = C\frac{k_{spp}}{\omega\varepsilon_0\varepsilon_1}e^{ik_{spp}x}e^{k_1 z} + D\frac{k_{spp}}{\omega\varepsilon_0\varepsilon_1}e^{ik_{spp}x}e^{-k_1 z}. \quad (1.22c)$$

From the continuity requirement of H_y and E_x, four coupled equations can be obtained at $z = -d/2$ and $z = d/2$. By solving the linear system of these four coupled equations, the following dispersion relation can be obtained:

$$e^{-2k_1 d} = \left(\frac{k_1}{\varepsilon_1} + \frac{k_2}{\varepsilon_2}\right)\left(\frac{k_1}{\varepsilon_1} + \frac{k_3}{\varepsilon_3}\right)\left(\frac{k_1}{\varepsilon_1} - \frac{k_2}{\varepsilon_2}\right)^{-1}\left(\frac{k_1}{\varepsilon_1} - \frac{k_3}{\varepsilon_3}\right)^{-1}. \quad (1.23)$$

where $k_1 = k_{spp}^2 - k_o^2\varepsilon_1$, $k_2 = k_{spp}^2 - k_o^2\varepsilon_2$ and $k_3 = k_{spp}^2 - k_o^2\varepsilon_3$. Figure 5b depicts corresponding dispersion relations for SRSPP and LRSPP. By increasing the thickness *d*, equation (1.23) transforms into two uncoupled SPP solutions at the respective interfaces described by (1.18).

2.1.3 Planar Optical Waveguides and Boundary Conditions

An optical waveguide is a physical structure that guides electromagnetic waves. Here a planar dielectric waveguide is considered with an asymmetric step-index profile. Figure 6 illustrates the waveguide structure geometry where the electromagnetic wave is coupled via grating and guided between two claddings. The goal in the current section is to express the electric field components[52] in cladding 2 for the guided transverse magnetic mode. Here, only the interface between core and cladding 2 with the corresponding permittivity values of ε_1 and ε_2 is taken into consideration. The corresponding electric field strength in the core is denoted as $\boldsymbol{E_1}(E_{x1}, 0, E_{z1})$ and in the cladding 2 as $\boldsymbol{E_2}(E_{x2}, 0, E_{z2})$.

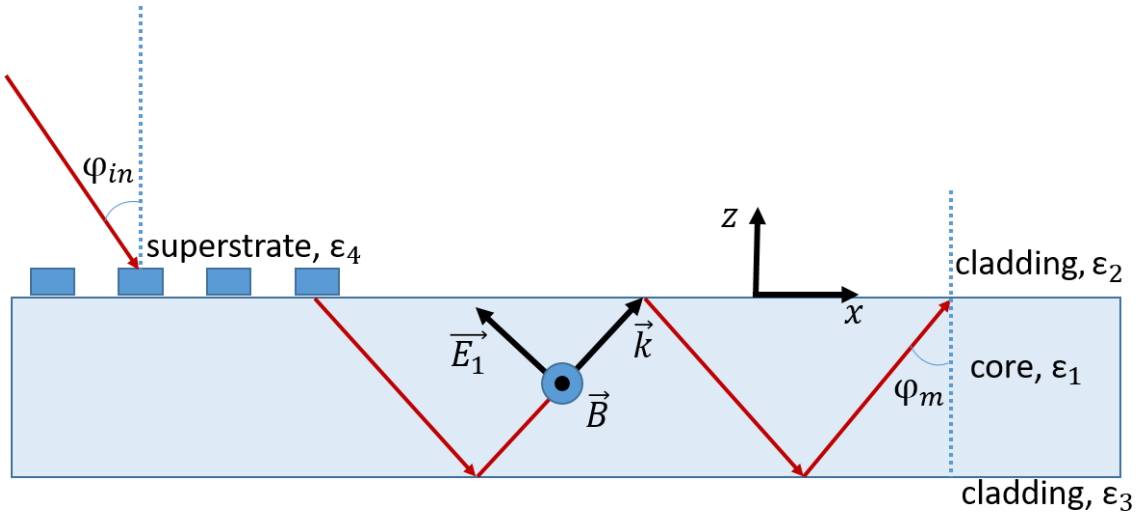

Figure 6: Schematic illustration of the asymmetric planar waveguide structure.

According to Maxwell's equations, the boundary between two dielectrics obeys certain conditions: the tangential components of the electric field must be continuous, and the normal components can be discontinuous[70]. The following boundary conditions can be applied for the interface between core and cladding 2:

$$\begin{cases} E_{x1} = E_{x2} \\ \varepsilon_1 \times E_{z1} = \varepsilon_2 \times E_{z2} \end{cases}, \tag{1.24}$$

From the geometry of Figure 6, the following expression can be obtained as well:

$$\begin{aligned} tan(\varphi_m) &= {E_{z1}}/{E_{x1}} \\ |E_1| &= \sqrt{{E_{x1}}^2 + {E_{z1}}^2}. \end{aligned} \tag{1.25}$$

Here, φ_m is the internal angle of the mode, which can be calculated from the momentum conservation:

$$\boldsymbol{k}_{in} = \boldsymbol{k}_{grating} + \boldsymbol{k}_{mode}, \tag{1.26}$$

where $\boldsymbol{k}_{in}$ is the momentum of incoming light, $\boldsymbol{k}_{grating}$ is the momentum acquired by the grating, for example, by a rectangular grating of period Λ, and $\boldsymbol{k}_{mode}$ is the momentum of

the mode coupled into the waveguide. Projecting (1.26) on the x-axis, the internal angle can be derived as:

$$\varphi_m = \arcsin\left(\frac{\sin(\varphi_{in})\cdot n_4 \pm \lambda_o/\Lambda}{n_1}\right). \tag{1.27}$$

where φ_{in} is the incident angle, λ_o is an incident wavelength, n_1 and n_4 are the refractive indexes of the waveguide and the superstrate, respectively. The resulting evanescent component of the electric field strength in the cladding are then:

$$E_{x2} = |E_1| \cdot \cos(\varphi_m) \cdot e^{-k_2 z} \cdot e^{-ikx}, \tag{1.28a}$$

$$E_{z2} = \frac{\varepsilon_1}{\varepsilon_2} |E_1| \cdot \sin(\varphi_m) \cdot e^{-k_2 z} \cdot e^{-ikx}, \tag{1.28b}$$

where $k_2 = \sqrt{{k_0}^2 \cdot \varepsilon_2 - k^2}$ and $k = k_0 \sin(\varphi_m)$. In the context of this thesis, the calculation result of field components in cladding is used to study the growth of nanoparticles activated and controlled by the evanescent field of the guided mode.

2.2 Basics of Fourier Transform

Before going further, some basics about two-dimensional Fourier transform must be reviewed. Fourier transform is a key processing tool in optics[71]. It is considered a shift of space from real to reciprocal space. The image in the spatial domain is used as input, while the corresponding image in the Fourier or frequency domain is considered output. Mathematically, the two-dimensional Fourier transform of a continuous two-dimensional function f(x, y) is defined as[71]:

$$\mathcal{F}(q_x, q_y) = \iint \mathrm{f(x,y)e}^{-\mathrm{i}2\pi(q_x x + q_y y)} dxdy. \tag{1.29}$$

Here f(x, y) is considered as an image with the brightness function given by $\mathrm{f}(\mathrm{x}_o, \mathrm{y}_o)$ at the coordinates $(\mathrm{x}_o, \mathrm{y}_o)$. The variables x and y have the dimensions of length, while in Fourier space, the variables q_x and q_y have the dimensions of inverse length or spatial frequency. The result of two-dimensional Fourier transform $\mathcal{F}(q_x, q_y)$ is a complex function[72] that can be expressed as:

$$\mathcal{F}(q_x, q_y) = A(q_x, q_y) e^{i\beta(q_x, q_y)}, \tag{1.30}$$

where $A(q_x, q_y) = |\mathcal{F}(q_x, q_y)|$ is a spectral amplitude, representing most of the information about the geometrical structure of the image in the spatial domain.

$\beta = \tan^{-1} \frac{Im(\mathcal{F}(q_x, q_y))}{Re(\mathcal{F}(q_x, q_y))}$ is the corresponding phase. It is important to review some basic properties of the Fourier transform, such as:

- symmetry:

  $\mathcal{F}(q_x, q_y) = \mathcal{F}(-q_x, -q_y)$;

- convolution theorem:

  $f(x,y) \cdot g(x,y) \overset{FT}{\Rightarrow} \mathcal{F}(q_x, q_y) \otimes G(q_x, q_y)$;

- translation:

  $f(x-\Delta x, y-\Delta y) \overset{FT}{\Rightarrow} \mathcal{F}(q_x, q_y) e^{-i2\pi(q_x\Delta x + q_y\Delta y)}$;

- Fourier transform of a sinusoidal function:

  $sin(q_x x) \overset{FT}{\Rightarrow} -i\pi(\delta(q-q_x)+\delta(q+q_x))$.

In this thesis, digital images are analyzed via two-dimensional Discrete Fourier Transform (DFT). The DFT of an arbitrary digital image $g(x,y)$ of size $M \times N$ is a complex number that depends on the pixel values of $g(x,y)$ calculated by the formula[73]:

$$\mathcal{F}(u,v) = \sum_{x=0}^{M-1} \sum_{y=0}^{N-1} g(x,y) e^{-i2\pi(\frac{ux}{M}+\frac{vy}{N})}. \quad (1.31)$$

The value of each pixel $\mathcal{F}(u,v)$ is obtained by summation of the multiplication result between the spatial image $g(x,y)$ and the corresponding base function $e^{-i2\pi(\frac{ux}{M}+\frac{vy}{N})}$. $\mathcal{F}(0,0)$ shows the image's zero-frequency component (DC-component) corresponding to the value of average image brightness. In order to compute a DFT, the FFT algorithm (called fast Fourier transform) is applied[74] in the current work.

2.3 Nanoparticle Growth

This section will present the classical theory of nanoparticle nucleation. Some basics of a young but very promising approach to plasmon-mediated nanoparticle growth[75–80] will be described, and a brief overview of nanoparticle positioning control by light during growth will be provided.

2.3.1 Nucleation Theory

Nucleation theory explains the process of initiating a thermodynamic phase transition[81]. The phase is formed by a sequence of events at an atomic level driven by thermal fluctuations. The process of nuclei formation in a solution can be described based on thermodynamic theory using the total free energy, defined as a sum of the surface and the bulk free energy[82]. The following expression defines the change in the total free energy of the spherical nucleus of radius r during the homogeneous nucleation process:

$$\Delta G = 4\pi r^2 \gamma + \frac{4}{3}\pi r^3 \Delta G_v, \tag{1.32}$$

where γ is the surface energy, and ΔG_v is the bulk free energy. In turn, ΔG_v can be expressed through the temperature T and saturation value S as:

$$\Delta G_v = -k_B \frac{T ln(S)}{v}. \tag{1.33}$$

Here, k_B is the Boltzmann's constant, and v is the molar volume. The term „homogeneous" refers to the nucleation process without favored nucleation sites. To find the maximum free energy needed to form a stable nucleus, the derivative of ΔG is taken with respect to the radius[82]:

$$\frac{d\Delta G}{dr} = 0. \tag{1.34}$$

By substituting ΔG_v in (1.32) with expression (1.33), the critical radius can be obtained by solving the equation with respect to r (1.34):

$$r_{crit} = \frac{2\gamma v}{kTln(S)}. \tag{1.35}$$

r_{crit} is the minimum radius needed to reach the nucleus to avoid redissolving. Replacing the radius by r_{crit} in expression (1.32), the corresponding critical free energy required for the existence of a stable nucleus is derived:

$$\Delta G_{crit} = \frac{4}{3}\pi\gamma r_{crit}^2. \tag{1.36}$$

To represent the nucleus formation process graphically, the total free energy with corresponding terms of the surface and the bulk free energy is schematically plotted as a function of the radius in Figure 7 below.

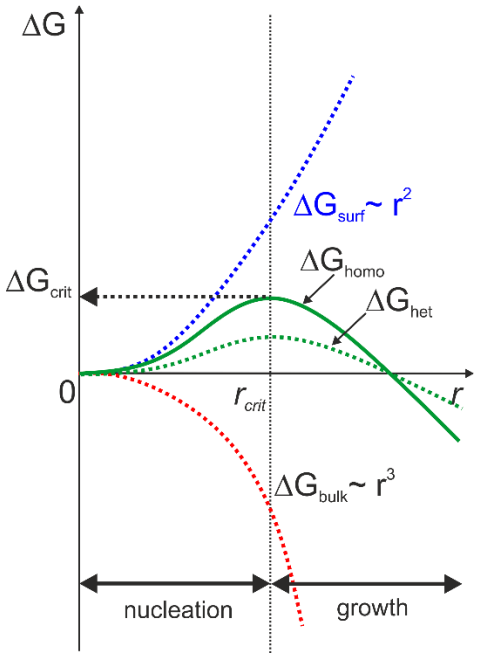

Figure 7: Free energy change as a function of radius r during the nucleation process is shown for the total free energy ΔG during homogenous (ΔG_{homo}, solid green line) and heterogeneous nucleation (ΔG_{het}, dashed green line), as well as for bulk ΔG_{bulk} (dashed red line) and surface ΔG_{surf} (dashed blue line) free energy.

Along with homogeneous nucleation, there is heterogeneous nucleation. Heterogeneous

nucleation occurs at reduced free energy (Figure 7, dashed green line) since a stable nucleating surface is already present. For example, nucleation in the solution cast on top of the foreign surface occurs on the surface first. The amount of free energy reduction compared to homogenous nucleation depends on the contact angle of the foreign surface (or surface energy). The higher the contact angle, the more energy is needed to overcome the barrier to stable nuclear formation. It is important to add that below r_{crit}, the nucleus is unstable and constantly competes between its nucleation and dissolving process. Beyond the critical size, the nucleus starts its stable growth, where growth dominates the shrinking process.

2.3.2 Plasmon-Mediated Growth

The plasmon-mediated method offers a new way of synthesizing plasmonic nanostructures with complete control over shape and size by light[41,75,83,84]. It allows a light-controlled transformation of isotropic metal nanostructures into anisotropic ones. LSP resonance excited in stable plasmonic nuclei serves as a driving force for the chemical reduction of metal ions with subsequent nanostructure growth. This section will briefly review the main mechanisms of plasmon-mediated syntheses for the growth of plasmonic nanoparticles.

At plasmon-mediated growth, three different processes can occur simultaneously, or one can dominate over others depending on the experimental condition. The first mechanism is a light conversation into the local heating of nanoparticles and the surrounding environment. This heating near the nanoparticle surface becomes noticeable by using a pulsed laser or a continuous wave laser at high power. Secondly, at LSP resonance, light is localized within a few nanometers above the nanoparticle surface, leading to a field strength enhancement of up to 10,000 times[85]. The hot spot of light localization is

defined mainly by the shape of the nanoparticle and the direction of plasmon oscillations. It is straightforward that an enhanced chemical reaction for plasmonic nanoparticles occurs at their poles, which is defined by the polarization direction of the incident electromagnetic wave. Molecules close to such spots experience increased field strength and photon flux. Therefore, the ability of metal nanostructures to concentrate light into small volumes can be beneficial in such chemical processes. The third possible process at LSP resonance excitation that can support nanoparticle growth is a generation of "hot" electron-hole pairs involved in a charge transfer reaction between the nanoparticle and the surrounding molecules. The transfer of electrons happens within the lifetime of the generated electron-hole pair, in the range of femtoseconds, followed by electronic thermalization and relaxation via lattice phonons within picoseconds[75]. The dependency of LSP resonance on the nanoparticle's composition, size, shape, and surrounding dielectric environment[86] allows the fabrication of plasmonic nanoparticles for many applications, particularly for surface-enhanced Raman scattering[87,88] or sensing[89–91].

2.3.3 Light-Controlled Alignment Theory

It was found that light-controlled synthesis enables not only control of the size and shape of nanoparticles but also of their spatial distribution. The light-controlled alignment of nanoparticles during growth on a planar surface under plane wave excitation was described in the frame of Polywka's work[43]. The theory predicts the positions of the growing nanoparticle with an estimated accuracy below 20 nm. Every new nanoparticle grows at the position of maximum intensity, defined by the interference of the incident and the scattered waves. As a result, nanoparticles form a particular distribution that stores information about electromagnetic waves involved in the alignment process in the form of nanoparticle positions.

To describe this idea mathematically, the following calculations are performed. First, N nanoparticles are placed at random substrate locations and excited by a plane wave $\boldsymbol{E}_{inc} = \boldsymbol{E}_{pl,0} \cdot e^{-i\boldsymbol{k}_{pl}\boldsymbol{r}}$, where, $\boldsymbol{k}_{pl}$ and $\boldsymbol{E}_{pl,0}$ are the wave vector and the amplitude of the incident plane wave, respectively. The resulting scattering field $\boldsymbol{E}_{sca}$ is calculated then as a sum of all scattered waves from N nanoparticles according to Polywka[43], R being the nanoparticle radius:

$$\boldsymbol{E}_{sca} = \sum_{i=1}^{N} \boldsymbol{E}_{sw,0}\, e^{-i\boldsymbol{k}_{pl}\boldsymbol{r}_i} \cdot e^{i\boldsymbol{k}_w\boldsymbol{r}_i} \cdot \frac{R}{\boldsymbol{r}_i}. \tag{1.37}$$

In (1.37), the near-field term was omitted for simplicity. Here, $\boldsymbol{k}_w$ and $\boldsymbol{E}_{sw,0}$ are the wave vector and the amplitude of the scattered wave, respectively. The resulting field strength is given as a superposition of the incident ($\boldsymbol{E}_{inc}$) and scattered ($\boldsymbol{E}_{sca}$) waves:

$$\boldsymbol{E} = \boldsymbol{E}_{inc} - \boldsymbol{E}_{sca}. \tag{1.38}$$

The intensity distribution is calculated as:

$$I(\boldsymbol{r}) \propto |\boldsymbol{E}|^2. \tag{1.39}$$

Inserting (1.38) into (1.39), the following expression is obtained:

$$I(\boldsymbol{r}) \propto |\boldsymbol{E}_{inc} - \boldsymbol{E}_{sca}|^2 = \boldsymbol{E}_{inc}{}^2 + \boldsymbol{E}_{sca}{}^2 - 2\boldsymbol{E}_{sca}\boldsymbol{E}_{inc}. \tag{1.40}$$

The point of maximum intensity of $I(\boldsymbol{r})$ defines every new position for the next nanoparticle, and this position changes with every new nanoparticle. The procedure (1.37) to (1.40) is repeated by adding new nanoparticles. In the end, the nanoparticle distribution formed in such a step-by-step process is analyzed using the Fourier transform. It yields two symmetrical circles shifted from the center coordinate in reciprocal space. In general, the formation of a circle in reciprocal space originates from the Fourier transform of a spherical wave $\mathcal{F}[E_{sca}]$, see Figure 8a. The radius of this circle corresponds to the projection of the scattered spherical wave momentum on a

nanoparticle plane divided by 2π:

$$\hat{r}_w = \frac{k_w}{2\pi} = \frac{n_w}{\lambda_0}. \tag{1.41}$$

n_w is the effective refractive index of spherical wave propagation.

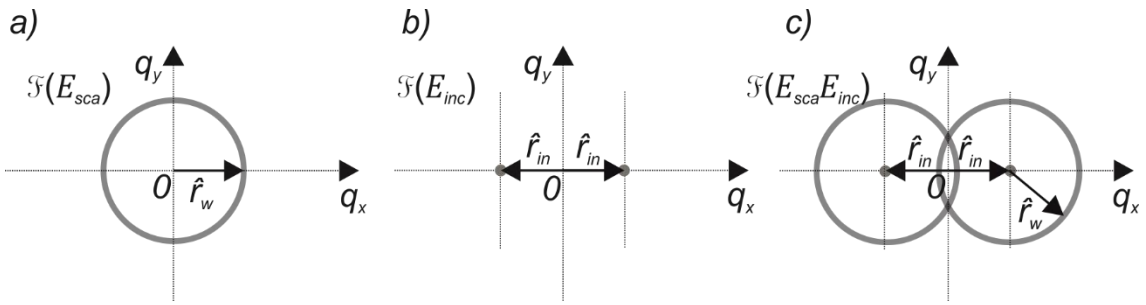

Figure 8: Fourier transformation of nanoparticle distribution, formed by interference of incident and scattered waves: a) Fourier transformation of the scattered spherical wave : circle of radius $\hat{r}_w$; b) Fourier transformation of the incident plane wave: two Dirac pulses at points $q_x = \pm\hat{r}_{in}$ and $q_y = 0$; c) convolution of Fourier-transformed incident and scattered waves: shift of circle (a) to the center of the Dirac points (b).

Similarly, the Fourier transform of an incident wave $\mathcal{F}[E_{inc}]$ (see Section 2.2) results in two Dirac pulses shifted by the value of $\hat{r}_{in}$ from center coordinates (Figure 8b). Such shift corresponds to the projection of the incident wave momentum on a nanoparticle plane divided by 2π:

$$\hat{r}_{in} = \frac{k_{pl}}{2\pi} = \frac{\sin(\varphi)\cdot n_{in}}{\lambda_0}, \tag{1.42}$$

where φ is the incident angle, n_{in} is the effective refractive index of plane wave propagation. The multiplication of two functions in real space $\boldsymbol{E}_{sca} \cdot \boldsymbol{E}_{inc}$ in (1.40) corresponds to a convolution of their Fourier-transformed functions according to the

convolution theorem:

$$\mathcal{F}[\boldsymbol{E}_{sca} \cdot \boldsymbol{E}_{inc}] = \mathcal{F}[\boldsymbol{E}_{sca}] * \mathcal{F}[\boldsymbol{E}_{inc}]. \quad (1.43)$$

This results in a symmetrical shift by $\hat{r}_{in}$ of two circles of radius $\hat{r}_w$ from the center coordinate in the reciprocal space (Figure 8c). As it can be seen, the Fourier transform analysis of intensity $I(\boldsymbol{r})$ or nanoparticle distribution enables extracting hidden information about electromagnetic waves involved in the complex interference process. More information about the light-controlled alignment theory and corresponding simulation can be found here[43].

2.4 Disorder Engineering and the Concept of Hyperuniformity

State-of-the-art optical devices are usually built based on well-ordered structures with sharp and predictable responses. In the past, any disorder in optics was generally considered unfavorable. Introducing disorder into photonic devices would promptly result in reduced control, increased uncertainty, and the unpredictability of optical responses. Nevertheless, managing and harnessing this disorder makes it feasible to attain comparable or even superior optical functionalities compared to well-ordered structures[8]. A new state of matter with „engineered disordered" introduced a decade ago by Professor Torquato erased a border between order and disorder in optics[92]. A new class of materials is known as super-homogeneous or hyperuniform materials. Such disordered materials have also been found in many natural and biological systems during the last decade. For example, hyperuniformity was found in matter distribution in the universe, receptor organization patterns in the immune system, and the photoreceptor patterns on the avian eye retina[3]. Moreover, the hyperuniformity concept allows for classifying and structurally characterizing special disordered configurations. This subchapter aims to introduce the theoretical foundations of hyperuniform disordered materials.

Hyperuniform materials can also be termed as materials with suppressed large-scale density fluctuations or near-crystalline materials, emphasizing enhanced uniformity in their element arrangement and their proximity to crystalline order without exhibiting Bragg peaks[3]. In order to quantify the hyperuniform materials, there are several options. One option is to use the number variance, which defines the variance in the number of elements within spherical windows of a given radius R_w. In a statistically homogeneous configuration of N points in d-dimensional Euclidean space, the number variance can be

de defined as[3]:

$$\sigma_N^2(R_w) = \langle N(R_w)^2 \rangle - \langle N(R_w) \rangle^2. \quad (1.44).$$

The number variance $\sigma_N^2(R_w)$ grows slower than window volume for hyperuniform configuration[3]. In contrast, the number variance grows in order of window volume in the disordered configuration[3]: $\sigma_N^2(R_w) \sim R_w^d$. At the same time, for periodic point configurations, which are a subclass of hyperuniform system, the scaling law[3] is $\sigma_N^2(R_w) \sim R_w^{d-1}$.

Another option to describe the hyperuniform materials is to use the structure factor $S(\boldsymbol{k})$. The structure factor reflects the information about the arrangement of structural elements to one another. In the particular case of N particle configuration at locations $\boldsymbol{r}_1$, $\boldsymbol{r}_2$,..., $\boldsymbol{r}_N$ subjected to periodic boundary conditions, the structure factor can be defined as[11,18]:

$$S(\boldsymbol{k}) = \frac{1}{N} \left| \sum_{i=1}^{N} e^{-i\boldsymbol{k}\cdot\boldsymbol{r}_i} \right|^2 = \frac{1}{N} |\mathcal{F}(M_o)|^2, \quad (1.45)$$

where $\boldsymbol{k}$ is a wavevector, M_o is the binary matrix with unit elements corresponding to the center coordinates of nanoparticles, and $\mathcal{F}$ is the two-dimensional Fourier transform of the matrix M_o. Hyperuniform point configurations have a structure factor $S(\boldsymbol{k})$ that goes to zero as a wave vector $|\boldsymbol{k}|$ tends to zero[92]:

$$\lim_{|\boldsymbol{k}| \to 0} S(\boldsymbol{k}) = 0. \quad (1.46)$$

The structure factor approaches zero with the following power-law dependency[3]:

$$S(\boldsymbol{k}) \sim |\boldsymbol{k}|^g, \quad (|\boldsymbol{k}| \to 0). \quad (1.47)$$

Here, power g is a measure of short-range order[93]. The degree of short-range order rises with increasing g. If g goes to infinity, the hyperunifom system tends to another form of hyperuniformity, stealthy hyperuniformity, where the states within $|\boldsymbol{k}| < |\boldsymbol{K}|$ in

reciprocal space are forbidden[3,11,20,92,94,95], i.e. $S(\boldsymbol{k}) = 0$. It results in suppressed density fluctuations from infinite wavelength down to intermediate wavelengths. Vanishing of the structure factor $S(\boldsymbol{k})$, which is proportional to the scattering intensity, makes such a materials transparent for incident radiation in a specific spectral window and/or angular range[11,96].

In experiments, polydisperse materials of spheres, disks, or non-spherical particles are studied. In such materials, the underlying point pattern might not induce hyperuniformity, which can lead to the wrong conclusion that a certain polydisperse material is not hyperuniform[97–99]. Therefore, instead of the structure factor, the spectral density (χ_S) is often chosen as the most accurate and natural tool to determine hyperuniformity for polydisperse materials[98,100,101]. Spectral density (χ_S) is the Fourier transform of the autocovariance function $\chi_V(\boldsymbol{r}) = P^{(i)}(\boldsymbol{r}) - \phi_i^2$, where ϕ_i is the volume fraction of a present phase i and $P^{(i)}(\boldsymbol{r})$ is the probability of finding two points separated by vector $\boldsymbol{r}$ in a phase i at the same time[101]. In analogy with the definition above, a hyperuniform material is one in which the associated spectral density $\chi(\boldsymbol{k})$ vanishes as the wave number $|\boldsymbol{k}|$ tends to zero[101]:

$$\lim_{|\boldsymbol{k}|\to 0} \chi(\boldsymbol{k}) = 0. \tag{1.48}$$

In numerical simulations, when the exact determination of nanoparticle radii is not possible, the spectral density $\chi(\boldsymbol{k})$ is calculated as[94]:

$$\chi(\boldsymbol{k}) = \frac{1}{V}\langle \left|\mathcal{I}^{(i)}(\boldsymbol{k})\right|^2 \rangle, \tag{1.49}$$

where V refers to the volume of the simulation box, brackets $\langle\cdot\rangle$ indicates an ensemble average, $\mathcal{I}^{(i)}(\boldsymbol{k})$ is the Fourier transform of the phase indicator function $\mathcal{I}^{(i)}(\boldsymbol{r})$ [94,99].

Since, in real experiments, the polydisperse system is restricted by size and is affected by

different errors and random noise, the spectral density approaches zero but never reaches "true zero". In order to determine the degree of hyperuniformity, the metric parameter H is introduced[99]:

$$H = \frac{\chi(\boldsymbol{k}=0)}{\chi(\boldsymbol{k}_{peak})} \quad , \tag{1.50}$$

where $\chi(\boldsymbol{k}_{peak})$ is the most prominent peak height of spectral density. When H is less than 10^{-2}-10^{-3}, the system is considered to be hyperuniform[99]. A similar criterion is also applied for the structure factor $S(\boldsymbol{k})$[3].

Chapter III Methods

The previous chapter has covered the basics of electromagnetic theory related to metal nanostructures, nucleation and growth mechanisms, and the concept of controlled disorder in optics. The theoretical aspects of light-controlled nanostructuring were provided as well. Now, the focus will be shifted to the experimental part. The methods used to fabricate, characterize, and simulate plasmonic metasurfaces will be reviewed here.

3.1 Fabrication Methods

3.1.1 Fabrication of a Surface Plasmon Polariton Waveguide

A sapphire substrate (Al_2O_3) of a thickness t = 0.5 mm and diameter d = 13 mm with a scratch-dig surface quality of 80 - 50 is used. On top of the sapphire substrate, an ultrathin chromium film of a thickness t = 1.5 nm is deposited as an adhesion promoter at a deposition rate of 0.2 Å/s, followed by a smooth silver film deposited at a deposition rate of 0.5 Å/s by thermal evaporation of silver shots (Alfa Aesar, 99.999%) inside a physical vapor deposition (PVD) chamber at the pressure of 10^{-6} mbar. The silver thickness varies from 20 nm to 60 nm, depending on the experiment (see Sections 4.1, 4.2, and 4.3). At thicknesses below 30 nm, the deposition rate is reduced and kept below 0.1 - 0.2 Å/s to reduce surface roughness. The root mean square (RMS) roughness of the silver films remains lower than 0.5 nm. In the end, a poly(methyl-methacrylat) (PMMA) film of a thickness of 15 nm is spin-coated on top. As a solvent for PMMA (Aldrich Chemical Company, M_w=350 kg/mol), propylene glycol methyl ether acetate (PGMEA) is used. After the spin-coating process, the sample is placed inside a pre-vacuum chamber (10^{-2} mbar) for 10 min to evaporate the solution's solvent. Such a waveguide structure can

support SPP modes at sapphire/silver and silver/PMMA interfaces.

3.1.2 Thin-Film Resonator Fabrication

The fabrication process of the thin-film resonator is divided into three steps: the preparation of a silver grating by using a shadowing effect during thermal evaporation on soft polymer; transfer printing of the silver grating from soft polymer onto a glass substrate[102]; the mechanical flattening of polystyrene film spin-coated on top of transfer-printed silver grating. This work uses polydimethylsiloxane (PDMS) as a well-known soft polymer for the replication process[103].

Preparation of a silver grating on a soft polymer: first, the surface of the blazed diffraction grating (50 × 50 mm, 600 grooves/mm, blaze angle of 5.15°) is covered by an anti-sticking layer (ASL) to fabricate a replica for the process. The ASL is an ultrathin layer (preferably a monolayer) of molecules with very low surface energy (< 20 mN/m). In this work, two methods are used to prepare the ASL layer: gas-phase and liquid-phase methods. Both are based on the use of (1,1,2,2 H perfluorooctyl)-trichlorosilane (short: F6).

For the gas-phase method, Teflon-based evaporation units and a spacer ring as a holder are used. Before the process, all Teflon parts are placed on the hotplate for 10 min at 150°C to remove water residues. Next, blazed grating and evaporation units with 50 µL of F6 are placed on a hotplate at 120° for 90 min inside a glovebox at a relative humidity below 30%. In the end, the grating covered by F6 is placed on a hotplate at 150°C for 15 min to evaporate the solution's solvent. More information about the process can be found in the work of Steinberg et al. [104]

An alternative to the gas-phase process is the liquid-phase process. The advantages of the liquid phase process are independency from air humidity, short process time, and

relatively small thermal stress for the sample, which is crucial for some polymers and photoresists. At the same time, the final anti-sticking layer is less uniform and usually contains more than one monolayer. For the liquid-phase process, the sample of interest is placed on a hotplate at 120°C for 10 min before the process. Afterward, it is loaded into isooctane (toluene is an alternative option), and 50 µL of F6 are added. The sample is kept in this F6-isooctane solution for 10 min. In the end, the grating is placed on a hotplate at 150°C for 10 min as for the gas-phase method.

The PDMS-based replica is fabricated by casting on top of the ASL coated blazed grating the mixture of the silicone prepolymer and the cross-linker in a 10:1 ratio by volume (Sylgard184 from Dow Corning). The grating with the viscous PDMS on top is placed into a pre-vacuum chamber (10^{-2} mbar) to remove entrapped air. Next, to harden the PDMS to a certain level, the grating is transferred to a hotplate at 80°C for 30 min. The corresponding atomic force micrograph of the replicated blazed PDMS grating is shown in Figure 9a. Next, the PDMS with the replicated grating structure is transferred to a vacuum chamber which is pumped down to the pressure of about 10^{-6} mbar for physical vapor deposition. The thermal evaporation of silver takes place at an angle of $\beta_o = 60°$ to the vertical of the grating surface (Figure 9b). The deposition rate is 1 - 2 Å/s.

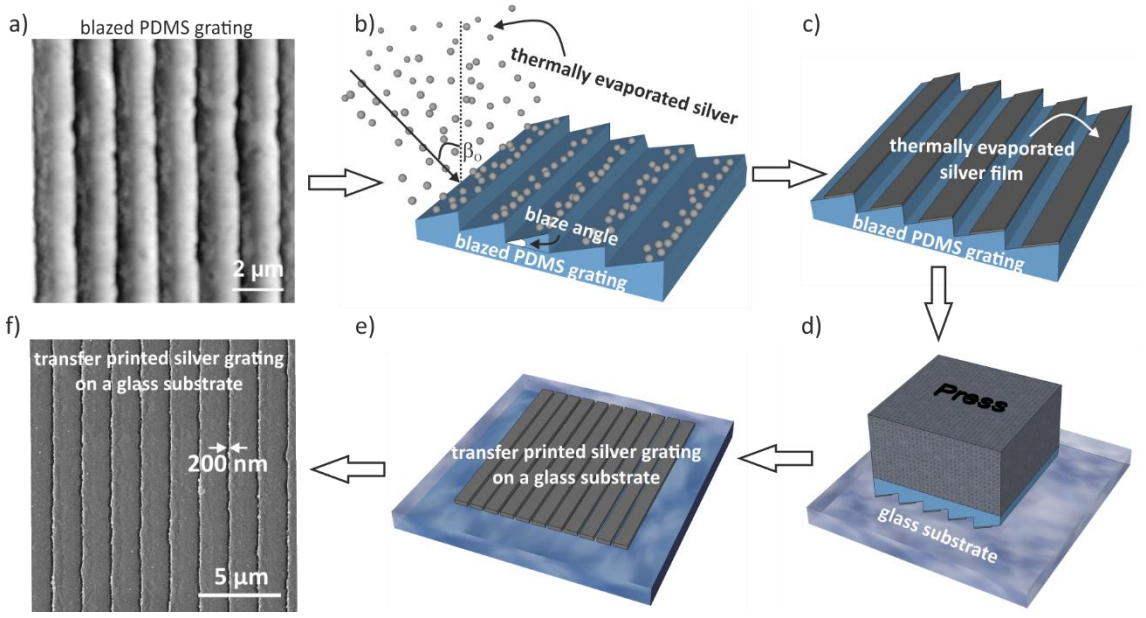

Figure 9: Technological steps to prepare a metal grating: a) an atomic force micrograph of a replicated blazed PDMS grating; b) silver thermally evaporated at a certain angle onto the blazed PDMS grating; c) silver film on PDMS and sides free of silver due to the shadowing effect; d) transfer printing of the silver film from PDMS onto the glass substrate using a homogeneously applied pressure; e) the result of a transfer-printed silver grating on the glass substrate; f) scanning electron micrograph of a transfer-printed silver grating of 1.66 µm period on the glass and corresponding gap width of 200 nm.

In this case, the nominal silver thickness is $d_o = 200$ nm. The actual thickness can be calculated as:

$$d = d_o \cdot \cos(\beta_o). \tag{1.51}$$

The thickness of the silver grating d, determined with a surface profilometer, is around 100 nm, which fits the formula (1.51) well.

Transfer printing of the silver grating from the soft polymer onto a glass substrate: the silver grating is then transferred from the PDMS (Figure 9c) onto the UV-treated for 3 min glass substrate. The layers with a few drops of isopropanol in between are pressed together using a homogeneously distributed pressure of 40 mbar (Figure 9d) for 10 min. Removing the PDMS, the metal grating is transferred onto the glass substrate (Figure 9e). The result of transfer printing is shown in the scanning electron micrograph in Figure 9f.

The period of the silver grating is 1.6 µm, and the width of the gap between the lines is about 200 nm, measured using atomic force microscopy (AFM). The transfer printing method allows the design of different geometries. For example, using a 555 nm grating and nominal evaporation thickness silver of 70 nm at 60°, the grating of 35 nm with gaps around 170 nm is fabricated (Figure 10a).

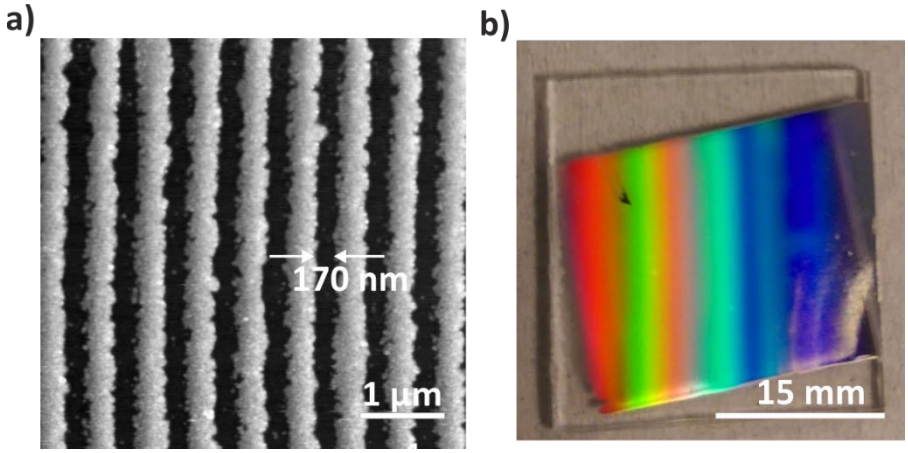

Figure 10: Transfer printing of metal grating: a) scanning electron micrograph of a transfer-printed silver grating of 555 nm period demonstrating the flexibility of the transfer printing method to achieve different periods, gaps, or thicknesses; b) photography of transfer-printed silver on glass using an MTS adhesion promoter.

To further improve the adhesion between the transfer-printed silver grating and the UV-treated glass substrates, (3-Mercaptopropyl) trimethoxysilane (MTS) by Aldrich Chemistry is used as an adhesion promoter. A mixture of 1% MTS and a solvent of either 99% of isooctane or 99% of hexadecane is mixed. Afterward, UV-treated glass substrates are placed into the solution for two hours to deposit one or more monolayers of MTS. The concentration of MTS has a critical impact on the transfer printing process. Increasing the concentration of MTS in Isooctane to 1.5% leads to better homogeneity and enhanced surface energy (75 mN/m). A further increase to 2% showed island-like growth.

Furthermore, different solvents are tested. Glass substrates are placed into a 1.5% MTS solution with isooctane and hexadecane. No difference in surface energy and transfer printing quality is found. Isooctane is used exclusively due to lower reactivity. The suggested MTS as an adhesion promoter allows for transfer printing of silver grating on glass over a large area with a high output quality (Figure 10b).

Mechanical flattening of polystyrene film spin-coated on top of a transfer-printed silver grating: a polystyrene film with a thickness of 120 nm was spin-coated on top of the transfer-printed silver grating on glass. As a solvent for polystyrene (Aldrich Chemical Company, M_w=350 kg/mol), Toluene (Fischer Chemical, > 99.9%) is used. After the spin-coating process, the solvent is evaporated at 85°C for 5 min on a hotplate.

To avoid groves above the gaps (Figure 11a), waviness of the surface, and later decoration phenomena during the growth of AgNPs, the polymer film is mechanically flattened using a polished silicon wafer covered with a gas-phase ASL layer. The silicon wafer was chosen due to the low RMS roughness, which is lower than 0.2 nm. The applied force on the sample must be homogeneously distributed. The flattening stack is schematically illustrated above the wavy polymer surface in Figure 11a.

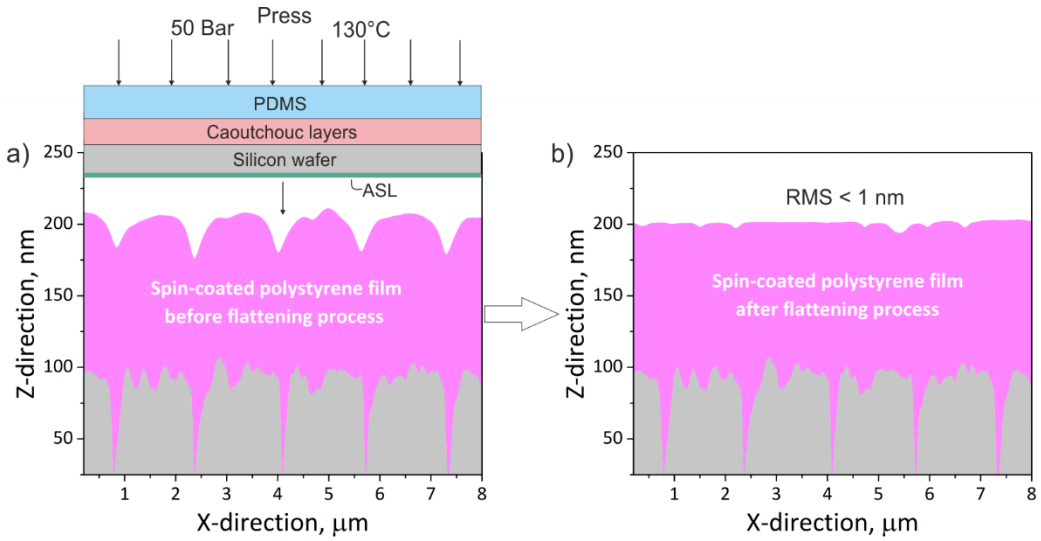

Figure 11: Profiles from atomic force micrographs of the transfer-printed silver lines with polystyrene film spin-coated on top: a) before and b) after the flattening, RMS < 1 nm.

To even out the pressure, additional caoutchouc layers (3 mm in thickness) are placed on the back side of the wafer, followed by a layer of PDMS (2 mm in thickness). After pressing the complete stack at 50 bar with a temperature of 130°C, the surface is flattened (Figure 11b). The RMS is less than 1 nm. It is important to note that the thickness of the polymer film should be kept higher than 90 - 100 nm to achieve a homogenous flattening on top of the metal gratings of a thickness of 100 nm, including the gaps between the grating lines.

3.1.3 Asymmetric Planar Waveguide Fabrication

In the following, a standard procedure for asymmetric waveguide fabrication is provided. OrmoPrime, OrmoStamp, OrmoClad, and OrmoCore from „Micro Resist Technology“ are used for the process. OrmoPrime is a ready-to-use adhesion promoter based on

organofunctional silanes designed to enhance the substrate's adhesion for OrmoStamp in nanoimprinting processes. OrmoCore and OrmoClad are UV-curable inorganic-organic hybrid polymers exhibiting relatively large refractive indices: 1.555 and 1.537 at 589 nm, respectively. They are soluble in PGMEA, and cross-linkable under UV exposure.

First, the holographic sinusoidal reflective grating with a period of 555 nm is covered by the vapor-phase ASL layer described in Section 3.1.2. Borosilicate glass squared wafers from Schott of 6 × 6 cm are used as a substrate for replication. The substrates are treated with an excimer lamp for 2 min to increase the surface energy for better adhesiveness during the spin-coating process[105]. Then OrmoPrime is spin-coated on top of the glass substrate at the speed of 2000 rpm for 30 sec to get a film thickness of 200 nm (Figure 12a). Next, the substrate is placed on a hotplate at 150°C for 5 min to remove the solvent. Afterward, OrmoStamp of around 0.8 - 1.0 g is cast on top of the holographic reflective grating with ASL. Then, the grating is covered by a glass substrate with OrmoPrime to form a homogenous film in between, mainly by capillary forces(Figure 12b). The complete stack is then placed in pre-vacuum (10^{-2} mbar) at 80°C for 10 min to prevent air inclusions in developing an OrmoStamp film. The temperature is used to lower the viscosity of the OrmoStamp and, therefore, facilitate the removal of air inclusions. In the next step, the OrmoStamp is cross-linked under UV exposure with an energy density of 1000 mJ/cm² for 12 min. Later, the OrmoStamp is carefully lifted off with a scalpel to separate the grating from the substrate with the replica of the grating on its surface (Figure 12c).

Photolithography follows after the replication process. The grating replica is covered with a 400 nm thick AZ 1505 positive photoresist layer by spin-coating at 5000 rpm for 30 sec (Figure 12d). The sample is placed on a hotplate at 110°C for 10 min to remove the solvent.

Afterward, a photolithographic mask is placed on the grating covered with photoresist, and two stripes are exposed to UV light for 5 sec each (Figure 12e), and the sample is placed in AZ 726 MIF developer for 55 sec (Figure 12f). The substrate is placed on a hotplate at 180 C to harden the photoresist. It is important to note that the temperature must be increased and decreased only gradually. Otherwise, the sample can break due to terminal stress. A liquid phase ASL is applied to finalize the process. The photoresist AZ 1505 from “MicroChemicals” contains the photoactive component diazonaphthoquinone (DNQ) solved in PGEMA. DNQ degrades under exposure. Therefore, a vapor phase ASL cannot be applied to samples coated with AZ 1505[106]. An examination of the fabricated replica with AFM revealed a problem concerning the surface flatness of the waveguide (Figure 12d). The surface's RMS roughness is around 45 nm, which is unacceptable for the envisaged optical application. Therefore, an additional flattening process is introduced after spin-coating AZ 1505 photoresist and removing the solvent to improve the surface roughness of the replica (Figure 12g). The flattening process is conducted by pressing the spin-coated sample with an ASL-coated wafer at optimum found parameters: 125°C at 80 bar of pressure for 5 min. Next, the flattened surface of the photoresist is exposed to UV light (Figure 12h). With this improved process, the surface roughness is lowered significantly from 45 nm to 1 nm. The final structure is shown in Figure 12i.

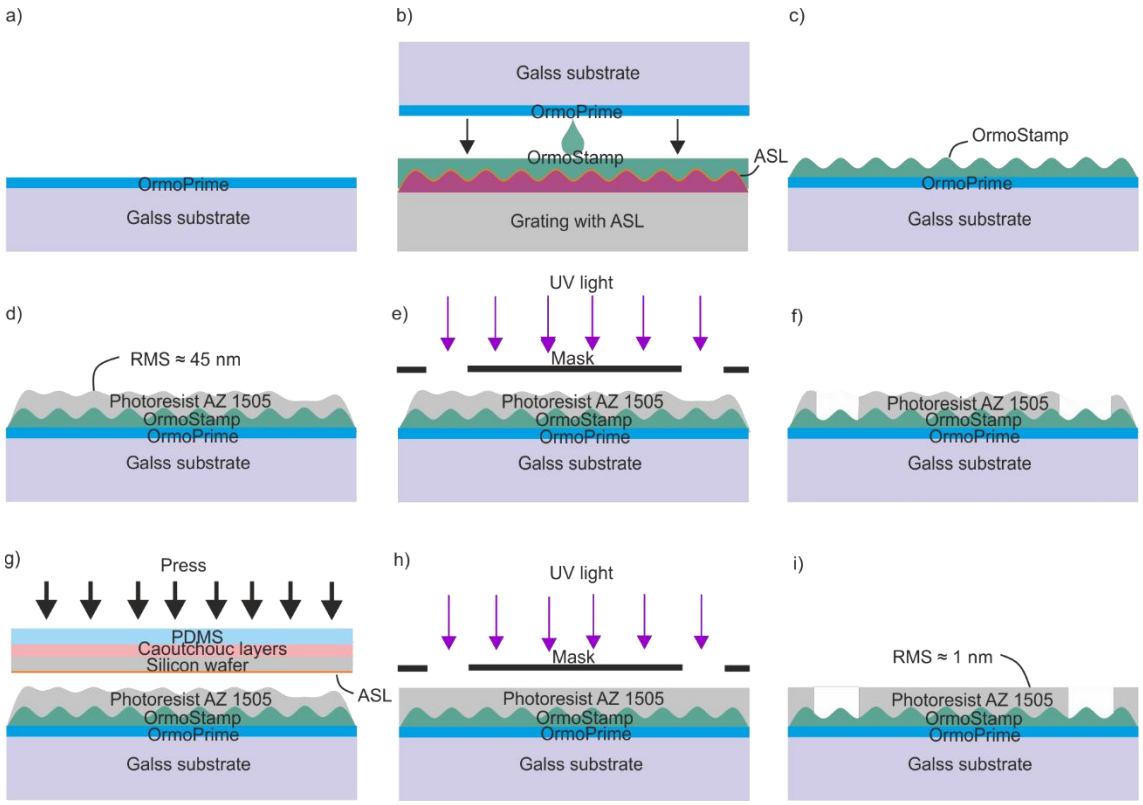

Figure 12: Schematic illustration of the replication and photolithography processes: a) UV-treated glass substrate with spin-coated OmorPrime; b) casting OrmoStamp on ASL-covered grating and placing the glass substrate with OrmoPrime on top; c) the final grating replica; d) spin-coated AZ 1505 photoresist on top of the grating replica; e) illumination of the photoresist through the mask with UV light; f) the final structure after etching of photoresist in the developer; g) additional flattening process after spin coating of AZ 1505 photoresist to improve the flatness of the photoresist surface; h) illumination of the flattened photoresist through the mask with UV light; i) the final structure with RMS of photoresist surface around 1 nm.

Next, the OrmoCore waveguide is deposited on a glass wafer covered by OrmoClad as a cladding layer (Figure 13a). The process starts by treating the glass wafer with an excimer

lamp for 2 min. Afterward, 1% OrmoClad in PGMEA is spin-coated at 9000 rpm to get a thickness of 70 nm. Next, to achieve a waveguide thickness of 1600 nm, a 40 wt. % OrmoCore in PGMEA solution is spin-coated at 2000 rpm for 30 sec. Then, the sample is placed inside a pre-vacuum chamber (10^{-2} mbar) for 10 min to evaporate the solution's solvent and eliminate possible air inclusions in the OrmoCore film. The partial cross-linking of the OrmoCore film by UV light for 10 sec is carried out in an inert gas atmosphere (nitrogen) to avoid the formation of an "inhibition layer".

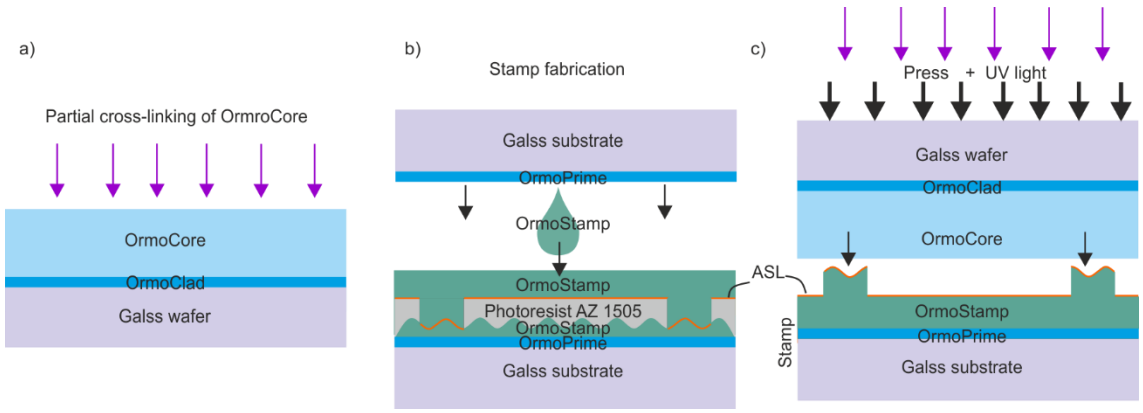

Figure 13: Schematic illustration of the technological steps for waveguide fabrication with coupling grating: a) spin-coated OrmoClad and OrmoCore on top of the UV-treated glass wafer; b) fabrication of the stamp structure, similar to the grating replication process; c) imprinting the stamp structure into the partially cross-linked OrmoCore, followed by UV illumination.

Next, the stamp is prepared according to the procedure similar to the replication of the holographic sinusoidal reflective grating (Figure 13b). Afterward, the stamp covered with ASL is imprinted into the prepared OrmoCore film at 100 bar for 15 min: 5 min under the press, plus 10 min under the press with UV exposure. This step is schematically illustrated in Figure 13c. An additional caoutchouc layers layer is needed to distribute the pressure

homogeneously. The waveguide quality strongly depends on the quality of the used stamp. Once the imprint process is finished, the sample and the used stamp are separated. The fabricated OrmoCore waveguide can support modes between air and OrmoClad (Figure 14a).

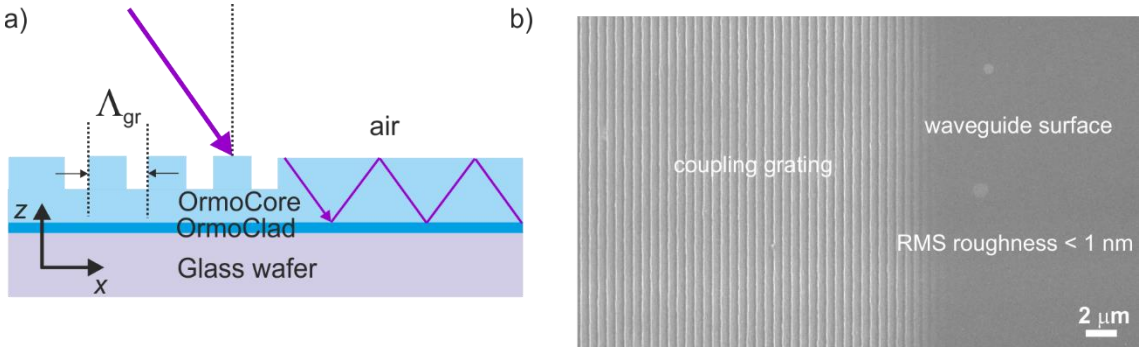

Figure 14: Fabricated OrmoCore waveguide: a) schematic illustration of coupling grating with the waveguide structure supporting the mode guidance between air and OrmoClad; b) corresponding scanning electron micrograph of the waveguide surface with coupling grating.

A sinusoidal grating with a period of 555 nm is used as a coupler to excite the corresponding mode. The scanning electron micrograph of the waveguide surface with coupling grating is shown in Figure 14b.

3.1.4 Ionic Solution Preparation for Silver and Gold Nanoparticle Growth

The ionic solution preparation for plasmon-induced growth of AgNPs is based on the mirror reaction described by Saito et al.[107]. The chemical reaction is based on reducing silver ions by glucose and involves a mixture of ammonia, silver nitrate, and aqueous glucose solutions. For the standard experiment, five aqueous solutions are needed: 30 wt. % of NH_3 (solution I), 6 wt. % of NH_3 (solution II), 2 wt. % of $AgNO_3$ (solution III),

6 wt. % of $AgNO_3$ (solution IV), and 35 wt. % of $C_6H_{12}O_6$ (solution V). When ammonia (NH_3) is mixed with water (H_2O), hydroxide ions are released into the water: $NH_3 + H_2O \rightarrow NH_3^+ + OH^-$. Mixing the silver nitrate ($AgNO_3$) with water (H_2O), it disintegrates into the ions: $AgNO_3 + H_2O \rightarrow Ag^+ + NO_3^- + H_2O$. The standard preparation of the final solution involves the following steps: using a microlite syringe solution I is added drop by drop to 3 mL of solution III until the color turns first to brown due to the formation of silver oxide ($2Ag^+ + OH^+ \rightarrow Ag_2O + H_2O$), and to transparent again due to dissolving and the formation of the $[Ag(NH_3)_2]^+$ cation complex. Next, solution IV is added until the solution turns pale-brown, indicating the formation of stable silver seeds. Afterward, solution II is added until the solution turns transparent again. Usually, only a few drops are required at this point to dissolve silver ions: $Ag_2O + 4NH_3 + H_2O \rightarrow 2[Ag(NH_3)_2]^+ + 2OH^-$. Further addition of solution II increases the sensitivity to light. In the end, the resulting solution containing $[Ag(NH_3)_2]^+$ cation complexes is mixed with 1 mL of solution V used as a reducing agent. In this case, silver as an electron acceptor reduces to elemental silver. The corresponding oxidation and reduction chemical reactions are $C_6H_{12}O_6 + 2OH^- \rightarrow C_6H_{12}O_6 + H_2O + 2e^-$, and $[Ag(NH_3)_2]^+ + e^- \rightarrow Ag + 2NH_3$. The final ionic solution is termed in this work as ELD solution (electroless deposition). The term “electroless” emphasizes the fact that there is no need for an electric field to conduct the chemical reaction.

The solution preparation for light-induced growth of AuNPs is based on the reduction of gold chloride with sodium citrate in an aqueous solution described by Turkevich et al. [108,109]. Here, hydrogen tetrachloroaurate (III) hydrate ($HAuCl_4 \bullet nH_2O$) is used as a precursor containing $[AuCl_4]^-$ anion. Sodium citrate ($Na_3C_6H_5O_7$) serves as a reducing

agent. For the standard experiment, two aqueous solutions are needed: 0.01 wt. % of $HAuCl_4$ (solution I) and 1 wt. % of Na_3-citrate (solution II). The rate of nucleation and further growth depends on the relative change in the amount of solutions I and II.

3.1.5 Light-Induced Fabrication of Plasmonic Metasurfaces

The ELD solution prepared according to the steps described above is cast onto the desired surface and exposed to light. The typical experiment is illustrated schematically below in Figure 15. To reduce the growth rate of AgNPs, the ammonia content is increased to 18.5 wt% compared to the standard ELD solution (12.0 wt%). When low ammonia content is used (≤ 12 wt%) and the reaction time exceeds a particular time (within 1 min), parasitic growth occurs on the substrate. This growth is based on the spontaneous formation of the silver nuclei at statistical substrate positions or within the volume of the ELD solution activated by room temperature. Moreover, when the nanoparticles reach a certain size in the volume, they fall on random substrate positions due to gravity forces. Such undesirable nuclei formation on the surface and in the volume of the ELD solution is slowed down by increasing the ammonia content.

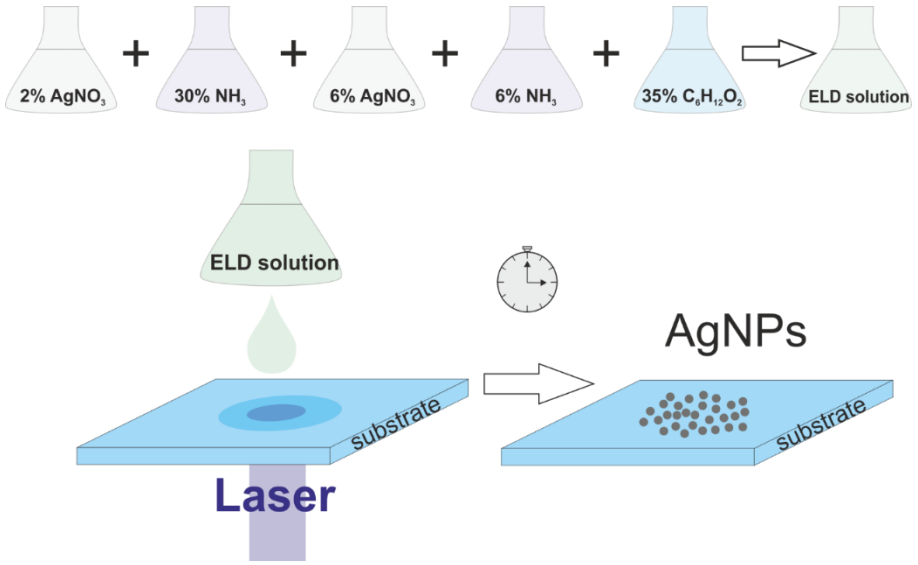

Figure 15: Steps for light-induced growth of AgNPs from ELD solution.

It is important to note that such "parasitic" growth happening without light is used to fabricate a plasmonic metasurface with tunable isotropic hyperuniform features. Therefore, the term "parasitic" growth refers only to light-induced deposition.

In this work, light-induced deposition of AgNPs from ELD solution with increased ammonia content is conducted under different excitation conditions. The corresponding experiments are listed below and schematically illustrated in Figure 16.

- **Experiments using polarized light and a glass substrate (Figure 16a):**

The ELD solution cast on the UV-treated borosilicate glass substrate of 30 × 30 mm is illuminated by either linearly or circularly polarized light at the incident angle of 0° (perpendicular incidence) using a CW laser diode from Roithner-Laser of 405 nm (RLDE405M-100-5, 100 mW), 532 nm (CW532-04-50, 50 mW), or 660 nm (RLDH660-70-3, 70 mW). Since the linear polarization state of the diode laser output can be unstable, an additional wire grid polarizer (WP25L-UB, Thorlabs) is used.

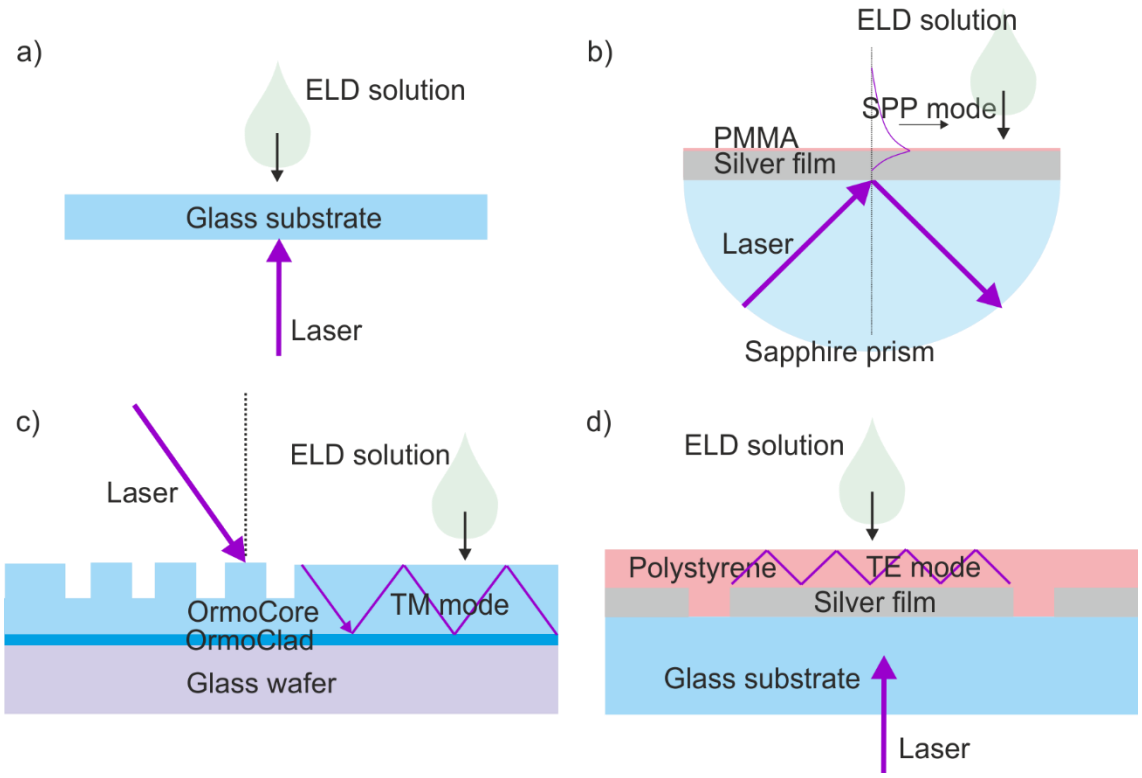

Figure 16: The schematic illustration of the experimental setups used for light-induced growth of nanoparticles: a) experiments with a glass substrate and polarized light at perpendicular incidence; b) experiments with SPP waveguide; c) experiments using asymmetric planar waveguide; d) experiments using a thin film resonator.

The circularly polarized light is obtained with a combination of a linear polarizer and a quarter-waveplate with its axes at 45° to its polarization axis placed in one line of light propagation. The illumination area for every laser is adjusted so that the power density for all lasers is around 0.45 W/cm². The deposition time varies between 4 and 12 min, see Section 4.1.

- **Experiments using an SPP waveguide (Figure 16b):**

The excitation by SPP modes is implemented using a standard Kretschmann configuration with a semi-cylindrical sapphire prism (Section 3.2.2). First, the SPP

waveguide structure (see Section 3.1.1) is placed on top of the sapphire prism with index matching liquid in between. ELD solution is cast on top of the SPP waveguide surface covered by PMMA film. The PMMA film serves here as a buffer layer to avoid film growth instead of nanoparticle formation. The CW diode lasers having 660 nm or 532 nm wavelengths with a nominal power of 70 mW and 30 mW, respectively, are used for excitation of SPP mode. The power density is set to around 0.40 W/cm^2. The incident angle of the p-polarized laser beam is set to 54° for 660 nm and 59° for 532 nm. The coupling efficiency between photons and SPPs stays between 75% and 80%. The deposition time is optimized to fabricate the plasmonic metasurface with either anisotropic stealthy hyperuniformity features (4 min) or a sharp ring structure in reciprocal space (6 min), see Section 4.1.

- **Experiments using asymmetric planar waveguides (Figure 16c):**

OrmoCore waveguides with a sinusoidal grating coupler (Section 3.1.3) are used. The laser beam of diameter 1.5 mm is focused at the edge of the sinusoidal grating to efficiently couple the light into the OrmoCore waveguides. The incident power density is around 1.50 W/cm^2. The coupling grating has a period of Λ = 555 nm. The TM_0 mode is excited with the p-polarized laser diode (λ_0 = 405 nm) at an angle of 57.8° to the grating normal (Figure 16c). When the TM_0 mode is excited, the ELD solution is cast on top of the OrmoCore waveguide surface at a distance of 2 - 4 mm from the edge of the coupling grating. After 460 sec of deposition, the ELD solution is removed.

- **Experiments using a thin-film resonator (Figure 16d):**

The thin-film resonator with a cavity made of polystyrene film (Section 3.1.2) is illuminated by the s-polarized CW laser (405 nm, 100 mW) from the bottom side. The power density is adjusted to around 1.5 W/cm^2. The ELD solution is cast on the surface of

the polymer film following the resonant excitation of TE dielectric modes. After 1 min of deposition, the ELD solution is removed.

It is important to note that after experiments with light-induced deposition of AgNPs, the drop of the ELD solution is removed by a napkin using the capillary motion of water. The sample is then immersed in pure water for 10 min to dissolve the remaining reaction products. In the end, a drying process is conducted using nitrogen flow.

- **Experiments using polarized light and a glass substrate for AuNP deposition (Figure 17):**

Next, the light-induced fabrication method of plasmonic metasurfaces has been extended to AuNPs. The following procedure was developed to grow AuNPs on a glass substrate under light illumination (Figure 17). First, 20 mL of 0.01% $HAuCl_4$ are drop-cast on a UV-treated borosilicate glass substrate. After the homogenous distribution of the solution along the substrate surface, the circularly polarized laser of 405 nm wavelength is applied for pre-illumination to replace the pre-heating step[108].

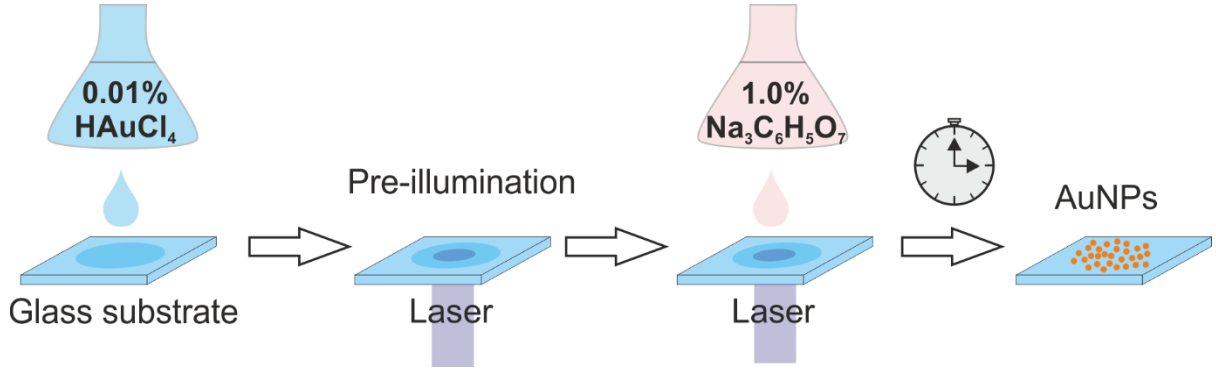

Figure 17: Light-induced fabrication of metasurfaces with AuNPs on a glass substrate.

The power density at the substrate is adjusted to the optimum values of 1.6 -1.8 W/cm^2. The threshold power for growth mediation is found to be 1.2 W/cm^2. Below this value, no

growth is observed. Next, 0.2 mL of 1% sodium citrate is added on top to start the nucleation and growth of AuNPs. After 950 sec of deposition, the solution is removed, and the substrate is immersed in pure water for 10 min. The final morphology of the AuNP metasurface depends on the ionic solution content, pre-illumination time of $HAuCl_4$, and deposition time. Similar to AgNPs, the morphology of AuNP metasurface can be varied by the optical properties of the used light (Section 4.1).

3.2 Characterization Methods

This section describes setups used to characterize light-induced growth. The basics of Raman spectroscopy are described here as a tool for the in situ study of ELD solution composition during AgNP growth. Furthermore, the Michelson interferometer is discussed. It is applied to measure the refractive index change to characterize the sensing performance of the plasmonic metasurface. The experiment for beam divergence measurements is described afterward. Next, microscopy techniques such as SEM and AFM are explained briefly. In the end, an overview of the methods for thickness and surface energy measurements of thin films is provided.

3.2.1 In Situ Monitoring of Silver Nanoparticle Growth

The following setups were built for the in situ monitoring of AgNP growth (Figure 18). The setup in Figure 18a is used to monitor the growth at the incident angle of 0° (perpendicular incidence). The setup is additionally supported with a lens and a linear polarizer. In the line of beam propagation, the "λ/4" plate can be applied in combination with a linear polarizer to get a circular polarisation state. The transmitted power through the ELD drop is monitored via a power meter placed 5 mm above the drop of the ELD solution. As a result, only transparent substrates can be used in this configuration. In this thesis, the setup of Figure 18a will be discussed in detail in Section 4.4.1.

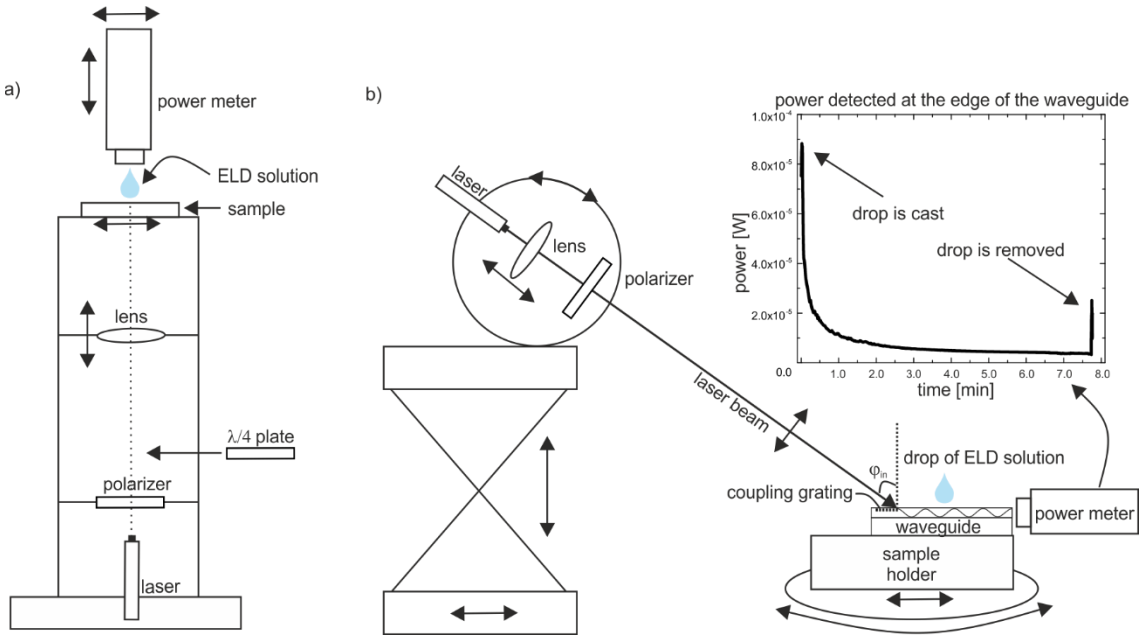

Figure 18: Setups for AgNP growth induced at perpendicular incidence (a) or by the evanescent field of the waveguide mode (b). The measurement of the power detected at the edge transmitted through the waveguide is shown in the sub-figure, including the moments of time when the ELD solution is cast and removed from a substrate.

The setup in Figure 18b is used for the deposition of AgNPs on an asymmetric waveguide. It offers a high degree of flexibility and allows the selective coupling of corresponding modes by choosing the polarization state, the incident angle, and the power density. Additionally, the power meter placed at the waveguide's edge allows in situ measuring of the transmitted power during nanoparticle growth on the surface of the waveguide. The typically measured power transmitted through the waveguide is shown in Figure 18b. When the ELD solution is cast, the power drops significantly within 1 min. Afterward, the transmitted power decreases much more slowly. The setup of Figure 18b will be discussed in detail in Section 4.4.2.

3.2.2 Attenuated Total Reflectance Setup

The widely used attenuated total reflectance setup in Kretschmann's configuration is applied here to excite the SPP mode[91], monitor the mode-induced growth of nanoparticles via reflectance, and later characterize the sensing performance of a plasmonic metasurface. As discussed in Chapter 2, direct excitation of SPPs with incident light is impossible due to the mismatch of the lateral momentum ($k_x = k_{\parallel}$), see Figure 4. Therefore, at a given frequency, the momentum of light must be increased. The additional sapphire prism increases the lateral momentum of light to $k_{\parallel} = k_0 \sin(\varphi) n_{prism}$. Here, k_0 is the wave vector of the incident wave, φ is the incident angle, and n_{prism} is the refractive index of the sapphire prism. A momentum match $k_{\parallel} = k_{spp} = k_0 n_{eff}$ enables the excitation of a bounded surface wave that propagates along the dielectric metallic interface with the phase velocity $v_p = \omega / k_{\parallel}$. Here, n_{eff} is the corresponding effective refractive index of the SPP mode. Schematically, the ATR setup is shown in Figure 19a.

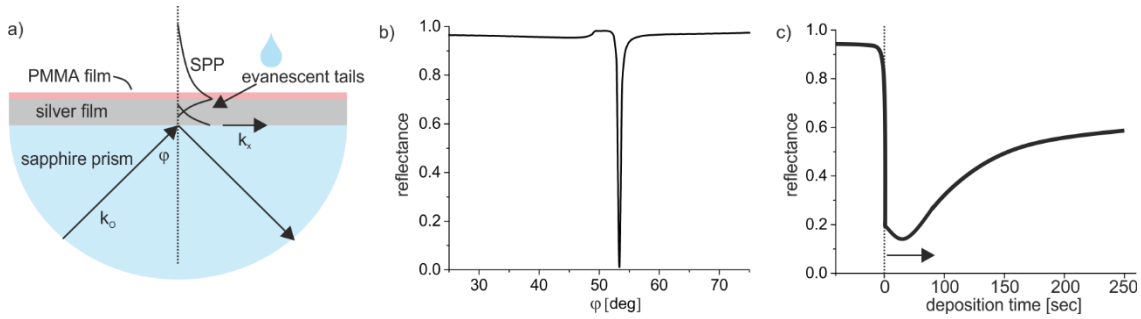

Figure 19: ATR setup: a) coupling between photons and SPPs via an evanescent field; b) SPP resonance at 54°, simulated for 660 nm laser at a silver film of the thickness t = 54 nm, and a PMMA film of t = 15 nm and non-absorbing liquid with refractive index of n = 1.336 on top; c) reflectance measured during the nanoparticle growth.

The collimated p-polarized laser beam illuminates the sapphire half-cylindrical prism with the SPP waveguide structure on top. Light is collimated using a set of lenses and polarized using a linear polarizer. A photodiode detects the reflected power. The resonance excitation occurs in the region of total reflection at the interface sapphire/silver when the evanescent field of the reflected wave and the field profile of the SPP mode overlap. In Figure 19b, the result of the reflectance simulation at the resonance excitation of SPPs is shown. The SPP resonance is found at the excitation angle of 54°, corresponding to minimum reflectance and maximum SPP excitation. Changing the refractive index of the environment in the vicinity of the silver film surface leads to a shift of the resonance curve to a higher or lower excitation angle. In this work, before casting the solution on the SPP waveguide surface, the SPP excitation angle is adjusted to the refractive index of the ELD solution. A water-based glucose solution of 7.77% is used as a test solution mimicking the ELD solution. As a result, the moment of casting the ELD solution is characterized by a sharp decay in reflectance followed by the excitation of SPPs. Figure 19c shows typical reflectance versus deposition time during nanoparticle growth from ELD measured experimentally. Due to the mismatch of the refractive index of the test solution and the ELD solution, the reflectance first slightly decreases, reaching its minimum after around 25 s of deposition. Afterward, the reflectance increases due to the increase in the refractive index of the environment during the nanoparticle growth. It is important to note that the experiment is conducted at a fixed excitation angle. That means that after changing the refractive index, the excitation angle needs to be adjusted to keep the efficient excitation of SPPs during the entire deposition of nanoparticles. Later experiments showed that either a slight mismatch in the refractive index at the beginning of deposition or a decrease in the efficiency of SPP excitation during the growth does not

significantly affect the growth of nanoparticles driven by the SPP mode.

3.2.3 Michelson Interferometer

A Michelson interferometer is a well-known configuration for detecting a change in the refractive index of a transparent medium[110]. Michelson interferometers produce interference by splitting light beams into two parts. Each part travels a different optical path and comes back together where it interferes with another part. Figure 20 shows schematically the experimental setup used in this work. It allows for monitoring a change in the refractive index of the test analyte pumped through the flow cell during the optical measurements.

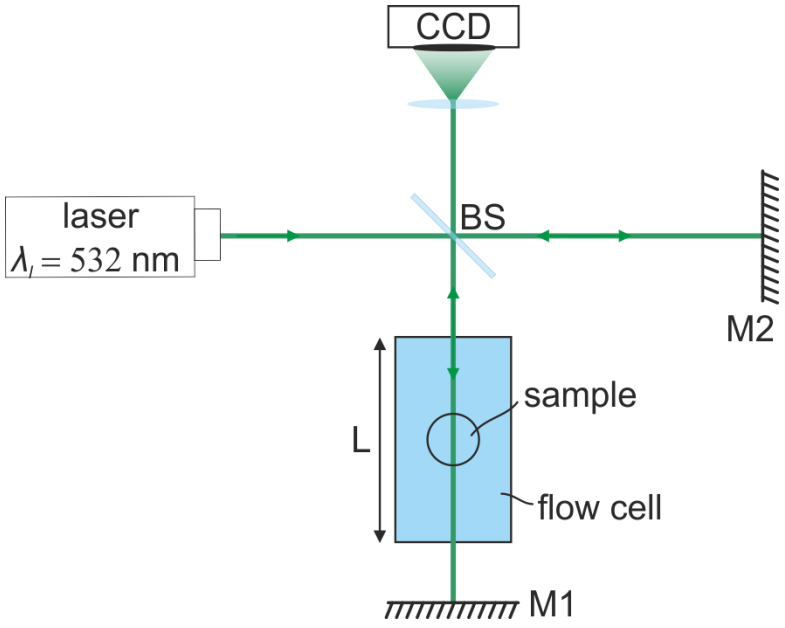

Figure 20: Michelson interferometer consisting of a light source, a 50:50 beam splitter (BS), two mirrors (M1, M2), and a CCD camera to detect the interferogram.

A diode laser with a wavelength of $\lambda_l = 532$ nm is used as a light source for the interferometer. One beam of the Michelson interferometer interacts with the flow cell

with an interaction length of $2 \times L = 16$ cm. Factor 2 is required as the beam propagates through the flow cell forward and backward. The beams are reflected from both mirrors and hit the beamsplitter back at the original incident beam's point. The corresponding interferogram at the interferometer's output is monitored by a CCD sensor (Figure 21a). By changing the refractive index of the test analyte, the corresponding phase φ_l of the detected signal is shifted by

$$\Delta\varphi_l = 2\pi \cdot \frac{2L}{\lambda_l} \cdot \Delta n. \tag{1.59}$$

Here, $\Delta\varphi_l$ is the phase shift, and Δn is the change in the analyte's refractive index.

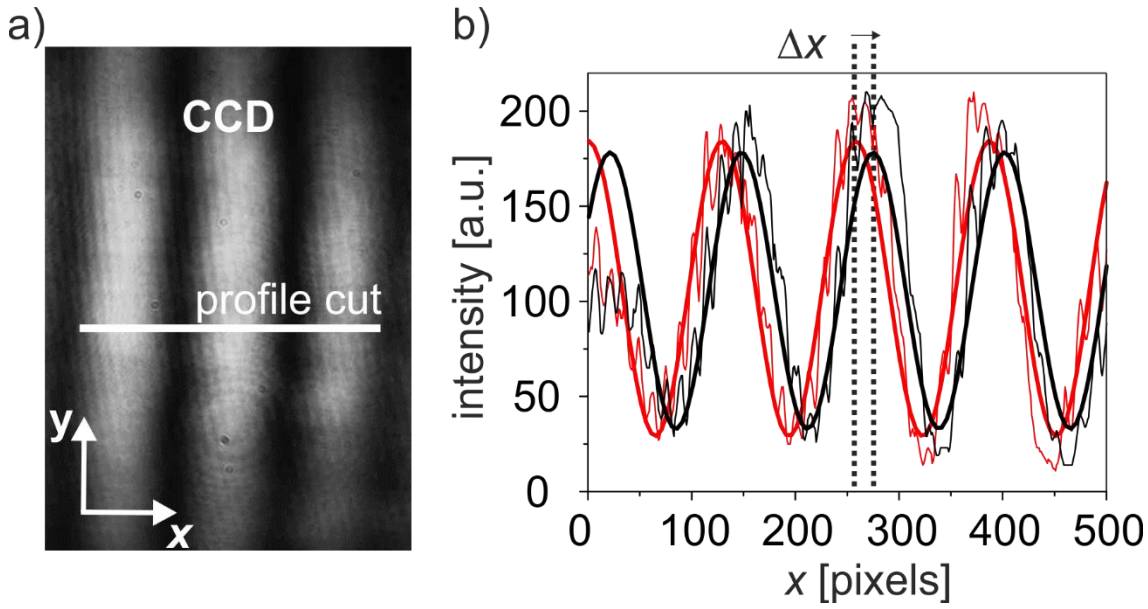

Figure 21: Refractive index detection scheme: a) interferogram detected by the CCD sensor; b) sinusoidal fit to the measured intensity profiles of two interferograms recorded on the CCD sensor.

A phase shift of $\Delta\varphi_l$ causes a shift of the interference fringes in x-direction detected by the CCD sensor (Figure 21b). The distance between two intensity maxima in the recorded interference pattern corresponds to a phase shift of 2π. In CCD images, such a shift can

be expressed in pixel units as $\Delta x = \frac{128.15\ [\text{pixels}]}{2\pi}\Delta\varphi_i$. CCD images captured while changing the refractive index of the analyte undergo a horizontal cut, followed by a sinusoidal fit of an obtained intensity profile shown in Figure 21b. Using the previous CCD image as a reference, the corresponding phase change is calculated. Summing up all phase changes, one obtains the overall refractive index change for the analyte during the entire optical measurement.

3.2.4 Measurement of Laser Beam Divergence

A beam divergence describes how a beam widens over a distance. The divergence angle ($\Delta\gamma$) at full width at half-maximum of the intensity beam profile is used to calculate the beam divergence. The divergence angle of the used 660 nm diode laser is measured as follows. First, the beam width is measured in front of the output aperture of the laser. Second, the beam width is measured on a screen at a distance of 57 m. The corresponding measured values are $\emptyset_{1,FWHM} = 2.50$ mm and $\emptyset_{2,FWHM} = 8.75$ mm (Figure 22).

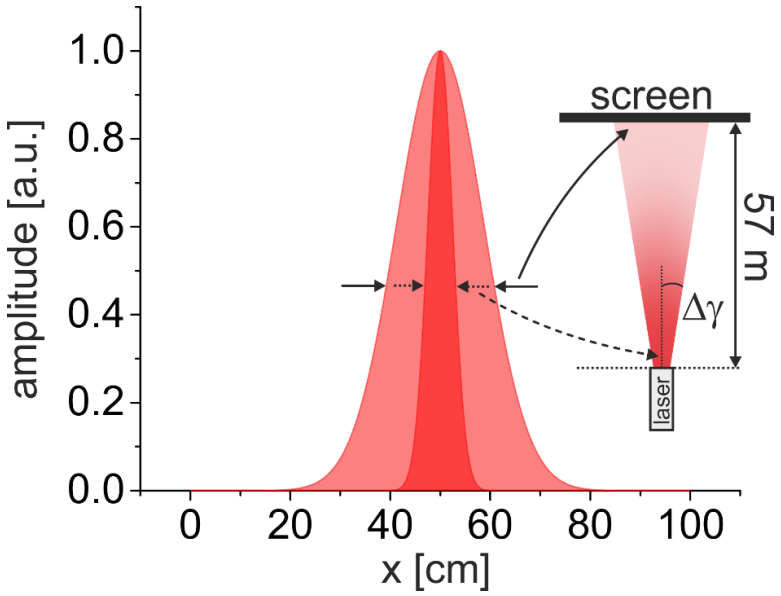

Figure 22. The measurement of laser beam divergence Δγ of 660 nm diode laser.

From the geometry sub-sketch shown in Figure 22, half of the opening angle $\Delta\gamma$, corresponding to beam divergence, is calculated: $\Delta\gamma \approx 5.48 \cdot 10^{-5}$ rad. The result of beam divergence will be used in Section 4.3 for the simulation of sensor response.

3.2.5 Scanning Electron and Atomic Force Microscopy

A scanning electron microscope[111] (SEM) is a microscope that provides a sample image with a resolution down to the nanometer scale by scanning the surface with a focused beam of electrons. A typical scheme of electron microscopes is shown in Figure 23a.

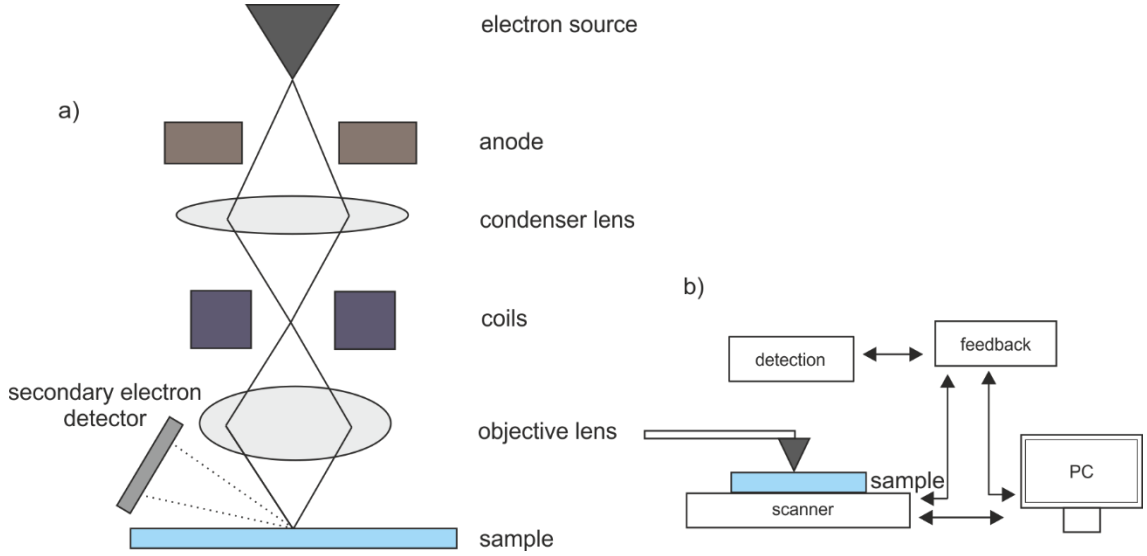

Figure 23: Simplified schemes visualizing the working principle of a scanning electron microscope (a) and atomic force microscope (b).

First, thermally generated electrons from a filament are accelerated and attracted toward the positively-charged anode. The setup is kept under vacuum to avoid any interactions with atoms and molecules. Similar to optical microscopes, additional lenses control the electron path. The lens consists of coils with flowing currents generating the magnetic field, which allows for the guidance of the electron flow. The condenser lens converges the

electron beam. It defines the size of electron beam, which determines the resolution of the microscope. Additional scanning coils are applied to raster the beam onto the sample. In turn, the objective lens serves to focus the beam on the sample. The interaction of electrons with atoms in the sample generates electrons, photons, and other irradiations. Backscattered (BSE) and secondary electrons (SE) are used to generate SEM images. BSEs result from elastic interaction between the electron beam and the sample. By contrast, SEs originate from inelastic interactions. Due to the difference in penetration depth, BSEs and SEs deliver different information. BSEs come from the deeper region of the sample. Therefore, the brightness of the coming signal depends on the atomic number of the studied material. At the same time, SEs are usually used to study surface topography. SEs are detected using a secondary electron detector (Everhart-Thornley). The signal intensity depends on the number of detected electrons and sample topography. In this work, the SEM investigations were conducted using a Philips XL30S FEG system with a field emission cathode based on a tungsten source.

Atomic force microscopy[111] (AFM) also enables a resolution down to the nanometer scale. In contrast to standard microscopes, the AFM does not use photons or electron beams and is, therefore, not diffraction limited. Instead, the AFM system uses a sharp mechanical tip to generate a 3D map of the sample surface. The resolution of the image depends on the geometry of the tip. A typical AFM system is shown in Figure 23b. A sharp tip is mounted on the end of a cantilever. The tip is made of n-doped silicon. A piezoelectric scanner controls the lateral and vertical position of the AFM tip relative to the surface. While scanning, the cantilever deflection occurs due to repulsive or attractive interactions between the atoms of the sample and the tip. Such deflection is monitored by a laser beam reflected from the back side of the AFM cantilever, covered by aluminum.

The photodetector monitors the power of the laser. The feedback loop keeps the deflection constant by adjusting the distance to the tip. It is needed to keep the setpoints constant during the measurements. In this work, the measurements were conducted using a Bruker Innova system in tapping mode with a tip radius of less than 12 nm (RTESPA-300). The oscillating tip is used to scan the sample surface. As a setpoint, an amplitude of cantilever oscillation close to the resonance frequency of 300 kHz is chosen. The surface topography is obtained by detecting the changes in oscillation amplitude of the cantilever while scanning the surface. The feedback loop minimizes the corresponding changes. The tapping mode is well-suited to measure the topographical features of soft materials like PDMS or other soft polymers.

3.2.6 Raman Spectroscopy

Raman spectroscopy[87] provides information about the rotational and vibrational motions of molecules. For molecule excitation, the monochromatic light source is used. Most photons are elastically scattered (Rayleigh scattering) in a way that scattered photons have the same energy as incident photons. Only a few photons have lower (Stokes Raman scattering) or higher energy (anti-Stokes Raman scattering) than incident photons. The spectrum of the intensity of scattered photons versus their difference in frequency to incident photons is called the Raman spectrum. In this work, the Raman spectra signal is recorded in situ during the growth of the nanoparticles on the glass substrate (Figure 24).

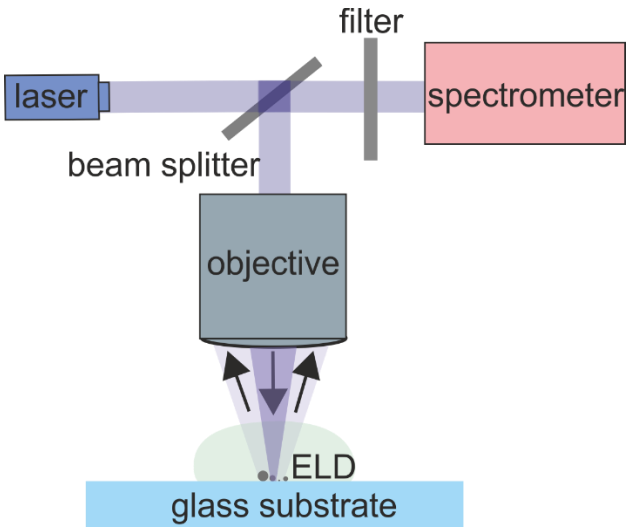

Figure 24: Simplified scheme visualizing the Raman spectroscopy setup used to study AgNP growth on a glass substrate.

AgNP growth is induced and controlled by an excitation laser. The scattered signal is collected to the objective with a high numerical aperture and then sent to the spectrometer. The additional filter before the spectrometer blocks the intense excitation light to distinguish the weak Raman signal from it. In addition, the grown AgNPs enhance the Raman signal and make it possible to study the ELD solution composition in detail.

3.2.7 Other Characterization Tools

Along with the characterization methods described above, some additional methods used in this work will be described shortly below. The surface profilometer 3ST is used to measure thin film thickness. The measurements are based on the electromechanical movement of the diamond-tipped stylus over the sample surface according to a user-defined scan length, speed, and stylus force. Additionally, the setup is equipped with a camera and a white light source. The average step height (ASH) analytical function is applied to calculate the thickness of the film by computing the differences between two

average height measurements. Before the measurements, the thin film is scratched with a needle down to the substrate. The stylus then moves over the scratch, thus measuring the difference in thickness between the thin film and the substrate. This process is repeated a few times at different positions on the surface of the sample. Afterward, an average value is calculated. The profilometer 3ST allows measuring vertical features ranging from 100 Å to 1310 kÅ on the round stage with a diameter of 165 mm.

The EASYDROP Contact Angle Measuring System from KRÜSS GmbH is used for contact angle measurements. The contact angle defines a solid's wettability to a liquid. The solid is considered wettable when the contact angle stays between 0° and 90°. Above 90°, it is not considered wettable. To measure the contact angle, a drop of two liquids, distilled water, and diiodomethane (CH_2I_2), is cast on a sample placed on a moveable table using a syringe with resolution in the µL range. The drop is illuminated from one side. A camera with high resolution captures an image of the drop from another side. The Young-Laplace fit of the droplet geometry is used to determine the contact angle. The contact angle is linked to the surface energy via the Young equation[112].

3.3 Simulation Methods

In this chapter, an overview of the simulation techniques employed in this work will be given. First, nanoparticle light scattering calculations are conducted in a discrete dipole approximation (DDA) frame[113]. A short description of such a calculation is provided in Section 3.3.1. Afterward, the procedure of disorder measures calculation based on SEM micrograph analysis is given in the following Section 3.3.2. Then, CST Studio and Comsol Multiphysics (Sections 3.3.3 and 3.3.4) are shortly described as tools to conduct a numerical simulation for thin film resonators and SPP waveguide structures. At the end of the current section, a new concept of sensor performance evaluation is introduced. A detailed description is given in Section 3.3.5.

3.3.1 Simulation of Light Scattering by Nanoparticles

According to the description above (Section 2.3.3), the nanoparticle alignment process during growth is governed by the interference of scattered and incident waves. To calculate the scattered waves, DDA is used in this work. In DDA, the scattering nanoparticles are represented by point dipoles. Each dipole acquires the dipole moment $\boldsymbol{p}_j = \varkappa_j(\boldsymbol{E}_{scat,j} + \boldsymbol{E}_{inc,j})$ at the location $\boldsymbol{r}_j$ by illumination of the wave with the field strength $\boldsymbol{E}_{inc,j}$. The resulting scattering field $\boldsymbol{E}_{sca,j}$ at location $\boldsymbol{r}_j$ is calculated as a sum of all waves scattered from individual dipoles. It can be expressed using formula (1.8) of the fundamentals chapter as[114]:

$$\boldsymbol{E}_{scat,j}(r,t) = e^{-i\omega t} \times$$

$$\times \sum_{m\neq j} \frac{e^{i\boldsymbol{k}\boldsymbol{r}_{jm}}}{\boldsymbol{r}_{jm}^3}\left(k^2\boldsymbol{r}_{jm} \times (\boldsymbol{r}_{jm} \times \boldsymbol{p}_m) + \left[3\boldsymbol{r}_{jm}\left(\boldsymbol{r}_{jm} \cdot \boldsymbol{p}_m\right) - \boldsymbol{r}_{jm}^2\boldsymbol{p}_m\right] \cdot \left(\frac{1-ik\boldsymbol{r}_{jm}}{\boldsymbol{r}_{jm}^2}\right)\right), \quad (1.53)$$

where $\boldsymbol{r}_{jm} = \boldsymbol{r}_j - \boldsymbol{r}_m$ is a vector between the point of consideration and the mth nanoparticle. In this work, formula (1.53) is implemented in a matrix form in Matlab, and

calculations are carried out for SPP modes as an excitation source with the strength of the electric field $\boldsymbol{E}_{inc,j}$ defined in Section 2.1. In detail, the simulation is conducted for SPPs excited by a p-polarized plane wave with a wavelength of 660 nm. The simulation domain has a size of 12 × 12 μm². The domain is divided into 3000 × 3000 mesh cells with the corresponding mesh cell size of 4 × 4 nm². The radius of silver nanoparticles is 110 nm. The simulation begins with a scattering calculation for five nanoparticles randomly placed on a substrate. The new nanoparticles are placed on a substrate according to the light-controlled alignment description of Section 2.3.3. The calculation is continued until a certain nanoparticle number is reached. The simulation results are shown in Figure 44a,b.

3.3.2 Measures of Engineered Disorder

Along with the standard two-dimensional Fourier transform, two additional disorder measures are used to characterize the fabricated plasmonic metasurface: structure factor and spectral density, which were discussed in detail in Section 2.4. The following algorithm is applied to calculate a structural factor (Figure 25a). The grayscale SEM micrographs with a size of 484 × 712 pixels are used as input. Next, the SEMs are cut to get squared micrographs of 484 × 484 pixels. They are then converted into a binary format using an "imbinarize" function with a threshold leveling procedure. After binarization some micrographs containing nanoparticles with missing pixels are filled afterward to reconstruct the form of the nanoparticle. The center coordinates and the size of the nanoparticles are found using the "regionprops" function (image processing toolbox), which is based on 8-connected components in the binary image (Figure 25b). The binary matrix (B) is built by assigning the center coordinates of the nanoparticles one and other pixels zero. It represents the distribution of nanoparticle centers plotted in

Figure 25c. Afterward, the DFT of the B matrix is performed by using the FFT algorithm. The absolute value of the calculation result is squared and divided by the number of centers (N_d) to get the value of the structure factor $S_1(\boldsymbol{q})$:

$$S_1(\boldsymbol{q}) = \frac{1}{N_d} |\mathcal{F}(B)|^2. \tag{1.54}$$

$\mathcal{F}$ denotes here the DFT of the matrix B. The described procedure is repeated for other SEM micrographs taken with the same magnification, brightness, and contrast values. The average value of the structure factor $\langle S \rangle$ is calculated by summing up the structure factor of individual SEMs and dividing them by the number of SEMs (N_c) in the loop:

$$\langle S(\boldsymbol{q}) \rangle = \frac{1}{N_c} \sum_{i=1}^{N_c} S_1^i(\boldsymbol{q}). \tag{1.55}$$

The procedure of spectral density calculation is similar to the structure factor calculation. However, in this case, the grayscale SEM micrographs are directly used for calculation without the need for binarization and center determination.

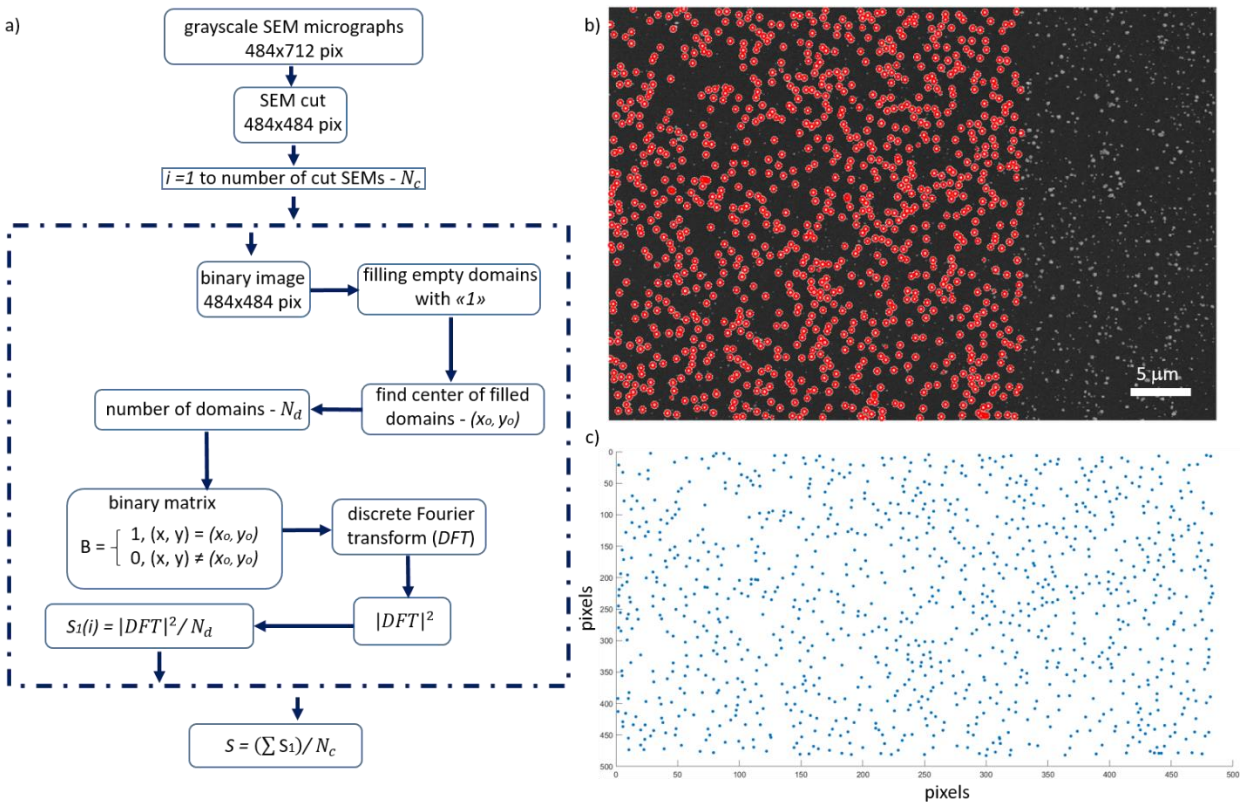

Figure 25: Schematic illustration of the algorithm used to calculate the average structure factor (a), the center determination on a squared sub-area of SEM micrographs of 484 × 484 pixels (b), and the corresponding underlying center distribution of the detected nanoparticles represented by matrix B (c).

The grayscale SEMs are transferred directly in a matrix form M. Afterward, the spectral density $\chi(\boldsymbol{q})$ is calculated based on formula (1.49) of Section 2.4:

$$\chi(\boldsymbol{q}) = \frac{a^2}{A}|\mathcal{F}(M - \bar{m})|^2. \tag{1.56}$$

Here, $\bar{m}$ is an average value of matrix M, A is the micrograph area, and a is the area of a single pixel[18,19].

3.3.3 Numerical Simulation using CST Studio Suite

The time and frequency domain 3D solver of CST Studio Suite (CST) based on the finite element method (FEM) is applied to study the optical properties of the resonator. The FEM is a means to solve differential equations numerically. The simulated domain is meshed into small cells to conduct finite element analysis. The calculations are performed for a single cell. The final result is a combination of answers from every cell in the simulation domain.

CST is an efficient tool for simulating multi-port optical systems. First, a 3D solver of CST is applied to simulate the dielectric resonator based on Bragg reflectors, which is used in Chapter 4 to emphasize the importance of alignment between plasmonic and dielectric parts of hybrid optical structures. The domain is meshed with a minimum of 10 cells per wavelength to get an accurate result. Open "add space" boundary conditions are used for simulation. The simplified dielectric resonator has a dielectric waveguide as a resonator cavity with a corresponding length of 1620 nm and a refractive index of 1.5. The Bragg reflectors consist of alternating high ($n_1 = 2.5$) and low ($n_2 = 1.1$) refractive index plates placed at both cavity sides. The corresponding plate thicknesses are $t_1 = \lambda/(4n_1) = 40$ nm and $t_2 = \lambda/(4n_2) = 92$ nm, respectively. By illuminating the resonator with a plane wave through a port placed inside the cavity, the resonance takes place for the wavelength of 405 nm. As a result, a standing wave is formed with an electric field strength profile shown in Figure 26.

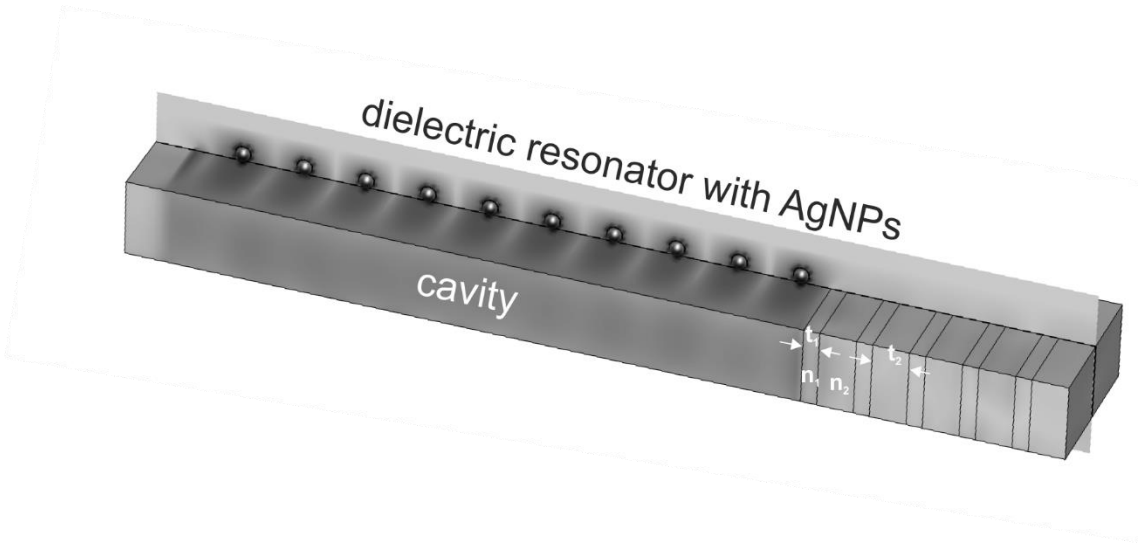

Figure 26: Result of dielectric resonator simulations with CST, a combination of a dielectric resonator with nanoparticles placed at different positions on top.

Next, on top of the dielectric resonator (Figure 26), the plasmonic nanoparticles are placed to study the structure's near-field response, see Section 4.4.1.

A similar investigation using CST Studio is performed for a thin film resonator shown in Figure 27a in the time and frequency domain. A periodic boundary condition is applied for ±x- and ±y-directions, while an open "add space" boundary is used for the ±z-direction. The structure consists of glass as a substrate, a silver film of 100 nm with a different gap width, and a polymer film (polystyrene) of different thicknesses. To mimic the ELD solution, a water-based environment is added on top.

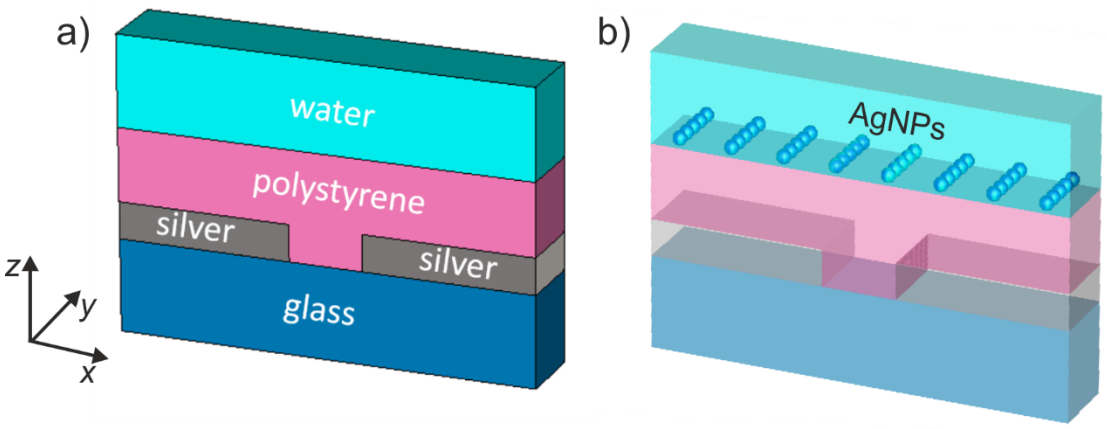

Figure 27. Numerical simulation of a thin film resonator: a) containing a glass substrate, a silver film with gaps, flat polymer, and a water environment; b) infinitely long nanoparticle chains on a polymer surface.

The gap is translated in the ±x-direction with a period of 1.66 μm according to applied boundary conditions. The structure is illuminated using a TE-polarized plane wave with a wavelength of 405 nm from the bottom side to the +z-direction. First, resonance behavior is studied for the coupled TE mode with respect to the polystyrene thickness and gap widths. The resonance cavity for the mode is formed between the two closest gaps. In the end, the chains of AgNPs (infinitely long in ±y-direction with a radius of 20 and 40 nm) are added (Figure 27b), and the near and far field response is investigated (Section 4.4.1).

3.3.4 Numerical Simulation using Comsol Multiphysics

The Wave Optics Module of Comsol Multiphysics in a Frequency Domain is applied to study resonance excitation of SPPs in the waveguide structure. Like CST Studio, COMSOL Multiphysics solves electromagnetic fields using the finite element method within the modeling domain. The simulation begins with setting up the model geometry, material

properties, and boundary conditions. After setting the effective mesh sequence manually, the simulation is conducted. A floquet periodicity is used in ±x-direction at the boundaries of the simulated domain (Figure 28a). Scattering boundaries are applied on the top and bottom of the simulation domain (±z-direction). The plane wave in p-polarization illuminates the SPP waveguide structure at a certain angle, and reflectance is calculated. The SPP resonance is excited and modeled before and after the deposition of AgNPs on top of the SPP waveguide.

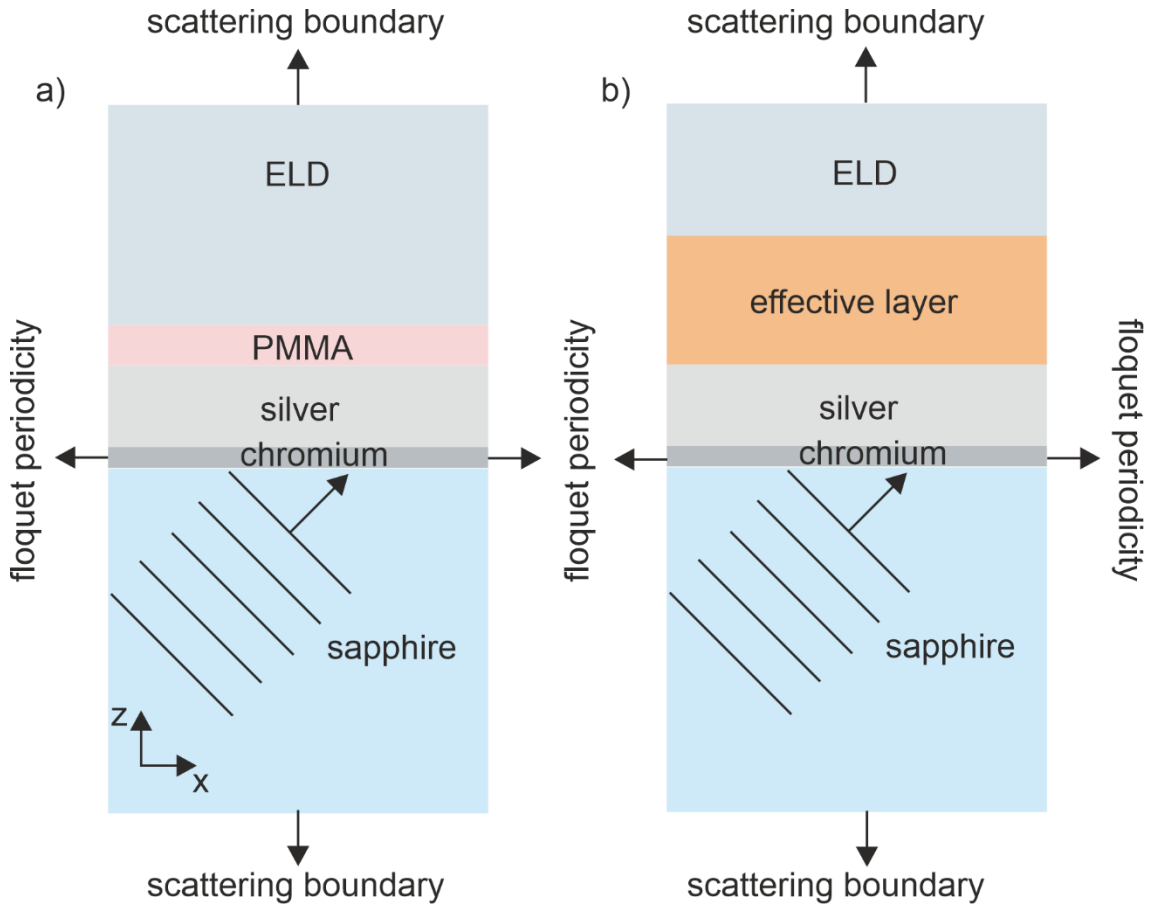

Figure 28. Numerical simulation of the SPP waveguide structure using Comsol Multiphysics without (a) and with additional losses (b) represented by an effective layer.

Additional losses mimicking absorption losses are introduced by adding an effective layer (Figure 28b) with a refractive index of $n = n_{real} + in_{img}$ on top of the silver film. The layer has a thickness of 200 nm corresponding to the average nanoparticle diameter in addition to the PMMA layer. The simulated SPP resonance curve is fitted to the experimental data by varying the imaginary part of the refractive index n_{img} of the lossy layer. The corresponding simulation results are shown in Section 4.3.

3.3.5 Evaluation of Sensor Response

The optical response of the plasmonic metasurface is simulated with an overlap function (U) between two rings with the radius and width defined by the experiments (Section 4.3). The amplitude profile of the rings $w(r)$ is modeled by a Gaussian function:

$$w(r) = \frac{1}{\sigma\sqrt{2\pi}} \cdot e^{-\frac{1}{2}\left(\frac{r-r_o}{\sigma}\right)^2}, \tag{1.57}$$

where σ is the standard deviation defined through the full width at half maximum ($FWHM$) of the ring width amplitude: $\sigma = FWHM \,/\, 2\sqrt{2ln2} \approx FWHM \,/\, 2.355$, r_o is the radius of the ring. The schematic illustration of two rings with a cut of the profile amplitude is shown in Figure 29.

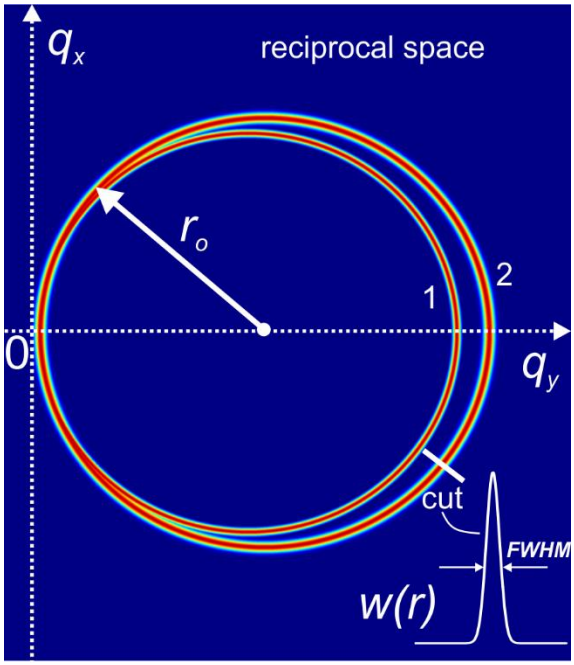

Figure 29. Definition of the geometry and amplitude of the ring with Matlab for simulation of the optical response of the plasmonic metasurface.

The rings shown in Figure 29 are converted into a matrix form, represented by matrixes A and B:

$$A = \begin{bmatrix} a_{11} & \cdots & a_{1m} \\ \vdots & \ddots & \vdots \\ a_{m1} & \cdots & a_{mm} \end{bmatrix}; B = \begin{bmatrix} b_{11} & \cdots & b_{1m} \\ \vdots & \ddots & \vdots \\ b_{m1} & \cdots & b_{mm} \end{bmatrix} \quad (1.58).$$

One ring can be rotated at a fixed radius r_o or expanded by increasing the radius r_o. Another ring is fixed. The corresponding overlap between two rings, is calculated then by an element-wise product of matrixes A and B. In a matrix form, the overlap is defined through matrix C as:

$$C = A \circ B = \begin{bmatrix} a_{11}b_{11} & \cdots & a_{1m}b_{1m} \\ \vdots & \ddots & \vdots \\ a_{m1}b_{m1} & \cdots & a_{mm}b_{mm} \end{bmatrix}. \quad (1.59)$$

The overlap function U is defined as a sum of all elements $c_{i,j}$ of the matrix C:

$$U = \sum_{i=1}^{m} \sum_{j=1}^{m} c_{i,j}. \tag{1.60}$$

In the end, the resulting overlap function is normalized by the maximum value of U (maximum overlap). For simulation, a fine-coarse grid mimicking reciprocal space $(q_x;q_y)$ is defined in Matlab. Each cell of the grid has a size of $5.2 \cdot 10^{-5} \times 5.2 \cdot 10^{-5}$ µm^{-2}. The result of the above-described simulation procedure is provided in result Section 4.3.

Chapter IV Results and Discussion

This chapter presents the results of the light-controlled engineering of features inside the reciprocal space of plasmonic metasurfaces. Section 4.1 is dedicated to plasmonic metasurfaces with hyperuniformity features as a clear manifestation of the engineered disorder. It extends the capability of the fabrication method with SPPs and demonstrates that plasmonic metasurfaces can exhibit tunable characteristics in reciprocal space. In Section 4.2, multimode engineering of features inside the reciprocal space with hybridized SPP modes is realized. It is demonstrated in detail in Section 4.3 that the plasmonic metasurfaces with the engineered disorder induced by SPP-controlled growth of nanoparticles can be directly applied as a high-performance refractive index sensor. The final result of Section 4.4 shows the impact of electromagnetic boundaries on the spatial ordering of nanoparticles during nanoparticle deposition.

4.1 Disorder-Engineered Plasmonic Metasurfaces

This section will present the results of plasmonic metasurface engineering based on AgNP growth from the ELD solution[15],[16],[17](Section 3.1.4) in darkness and under illumination. This method offers versatile experimental access to a bottom-up fabrication method for engineered disordered metasurfaces. Unlike other state-of-the-art bottom-upmethods[13,30,115], it does not rely on suspensions or dispersions of nanoparticles that self-assemble on top of the sample surface. Moreover, growth from a chemical reactant avoids undesired agglomeration of nanoparticles, so it does not need additional dispersing agents, which is attractive for cost-competitive large-scale applications. In Section 4.1.1, it is shown that the growth of AgNPs in the absence of light allows the fabrication of a plasmonic metasurface with the features of hyperuniformity. The impact

of deposition time and temperature on hyperuniformity is also discussed. In Section 4.1.2, the impact of light on a growing plasmonic metasurface is studied, and a corresponding theoretical description is developed. Plasmonic metasurfaces with isotropic and anisotropic stealthy hyperuniformity are engineered using circularly polarized light and SPP modes, which is experimentally demonstrated in Section 4.1.3. Finally, the formation of sharp characteristics in the reciprocal space during SPP-controlled deposition of nanoparticles is demonstrated, and a corresponding description is suggested.

4.1.1 Disorder Hyperuniform Plasmonic Metasurfaces Fabricated in Darkness

Any growth in darkness has been considered undesirable and was referred to as parasitic growth previously[43]. However, after a closer look at the morphology of AgNPs grown on a glass substrate in darkness, it was observed that this metasurface has features of hyperuniformity. The deposition experiment is shown schematically in Figure 30a. The ELD solution is prepared as described in Section 3.1.4. Figure 30b shows the photograph of the substrate after 23 min of deposition. The resulting metasurface covered by AgNPs is investigated using an SEM (Section 3.3.2). A typical SEM micrograph of the fabricated plasmonic metasurface is shown in Figure 30c. The densely packed AgNPs exhibit an average nanoparticle radius of 38 nm (Figure 30d). The minimum radius of the nanoparticle is about 13 nm. The corresponding fraction of the area covered by AgNPs is 39%, commonly referred to as a filling factor (short FF).

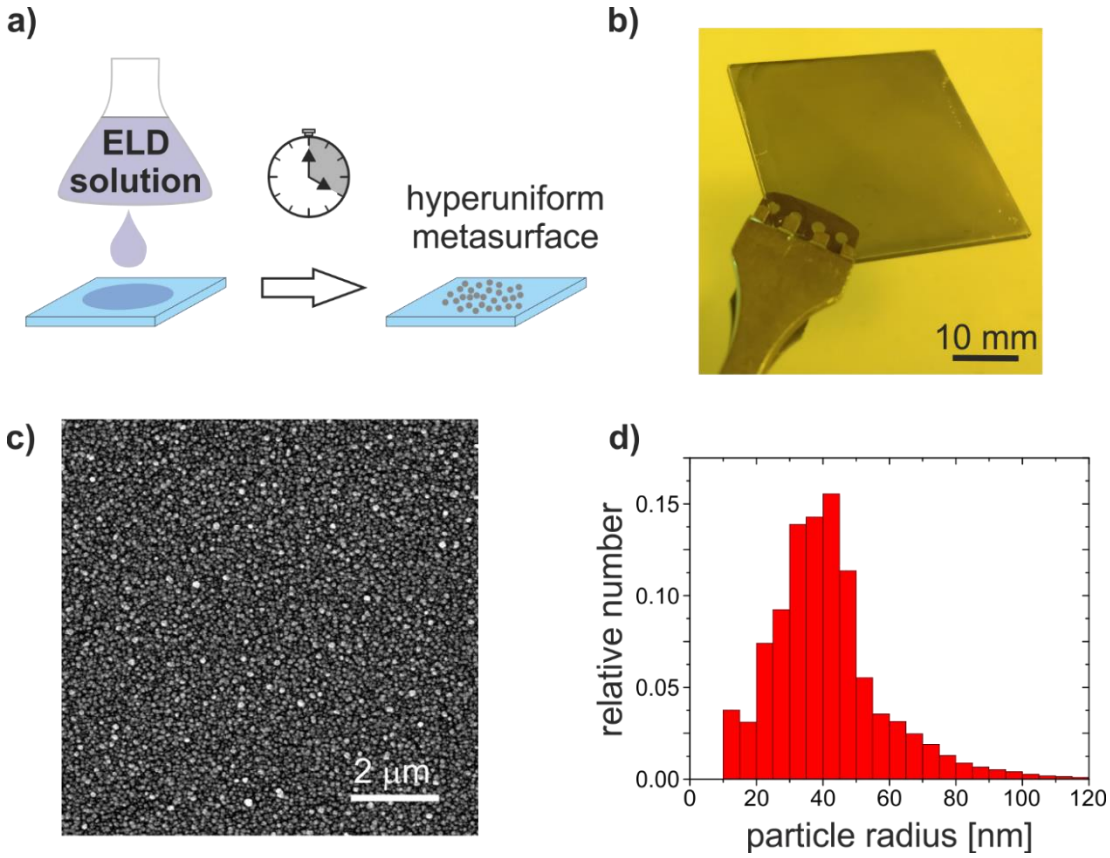

Figure 30: The fabrication of metasurfaces in darkness with hyperuniform features: a) the fabrication procedure without light; b) a photograph of a substrate after deposition; c) the SEM micrograph of the resulting plasmonic metasurface; d) the histogram of the nanoparticle radii extracted from the SEM micrograph.

The nanoparticle assembly on the real-space SEM appears to be random in both spatial and radius distribution (Figure 30c,d). However, the Fourier-transformed electron micrograph (FTEM) reveals features of hyperuniformity in the nanoparticle assembly (Figure 31a). Here q refers to spatial frequency values ($q = 1/\lambda$). While the Fourier transformation is a common method to analyze the surface morphology of a nanostructure, in practice, the spectral density χ_S is a more accurate and reliable method to analyze metasurface with hyperuniform features[92,98,101,116]. The spectral density

extracted from the grayscale SEM micrographs according to formula (1.56) and the procedure described in Section 3.3.2 is shown in Figure 31b. As the feature inside the reciprocal space possesses rotational symmetry apart from a line-like artifact discussed later, the spectral density can be converted into polar coordinates (r, φ) and averaged over the angle φ from 0 to 2π. The corresponding normalized value of the angular-averaged spectral density is shown in Figure 31c (black curve). The fabricated metasurface has a maximum of $\chi_S(r)$ at around 4.9 µm^{-1}, which corresponds to 204 nm in real space. According to the definition of equation (1.48), the current nanoparticle distribution is near-hyperuniform as the spectral density is not suppressed down to zero.

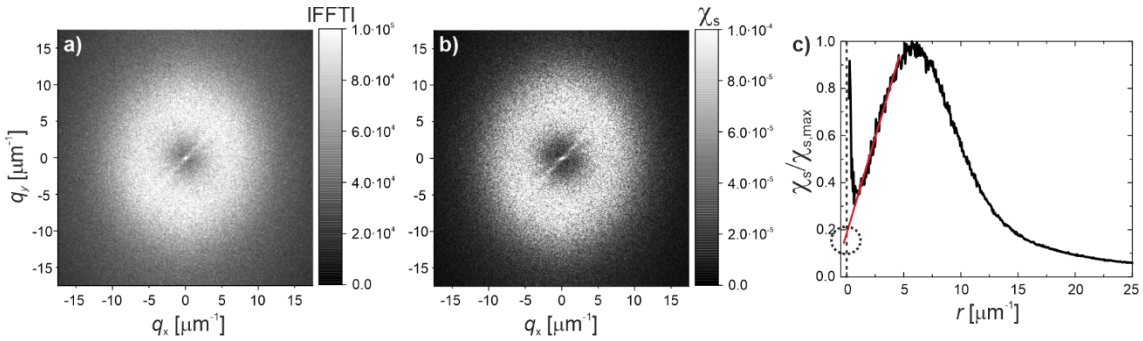

Figure 31: The reciprocal space analysis of a plasmonic metasurface fabricated in darkness: a) the FFT value of the SEM micrograph derived via 2D Fourier transformation; b) the spectral density representing the degree of hyperuniformity in the nanoparticle distribution; c) the normalized angular-averaged spectral density with a corresponding linear fit (red line), employed for quantifying the degree of hyperuniformity.

However, true hyperuniformity cannot be directly observed in the real experiment[47] as spectral density is defined over infinitely large lateral dimensions. Using the metric H_χ introduced in Section 2.4, it is estimated how far a nanoparticle distribution deviates from

the hyperuniformity state[47]. The lower this value, the larger the degree of hyperuniformity. To estimate H_χ according to formula (1.50), a linear approximation of the spectral density is applied for small values of r (Figure 31c, red line). Afterward, dividing the aproximated value of χ_S at $r = 0$ (Figure 31c, dashed circle) by the value $\chi_{S,max}$, corresponding to the maximum or most prominent peak value of the spectral density, the degree of hyperuniformity is estimated to be 0.18, indicating that the plasmonic metasurface is near-hyperuniform according to the literature[117,118]. It stays in the same order of magnitude as the recently reported values[117,118] calculated for monodisperse packing of hard disks (H_χ = 0.61) and binary-disk mixtures ($H_\chi \approx$ 0.10). The variation of the AgNP deposition time with the current method makes it possible to control the hyperuniformity in situ via morphology change. Thus, the metasurfaces were prepared for 10, 22, and 25 min of deposition time to demonstrate this. Figures 32a - c show the corresponding graphs of normalized angular-averaged spectral density.

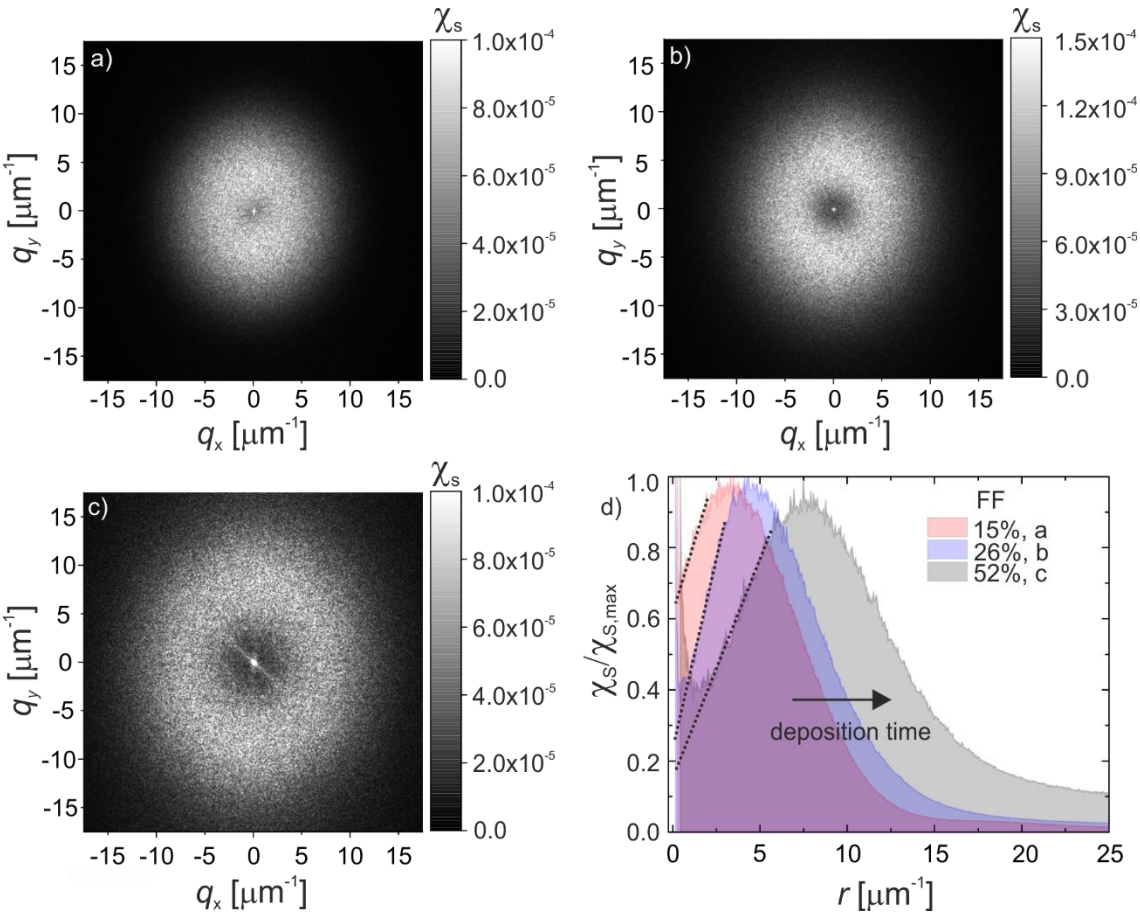

Figure 32: In situ control of the isotropic near-hyperuniformity: a)-c) the spectral density χ_S calculated for plasmonic metasurfaces obtained at 10 min, 22 min, and 25 min of deposition; d) the corresponding normalized angular-averaged spectral density.

The maximum peak $\chi_{S,max}$ shifts to 3.30 μm^{-1}, 4.60 μm^{-1}, and 7.80 μm^{-1} over deposition time, respectively. This demonstrates control of the features inside the reciprocal space of the metasurface during nanoparticle deposition. The corresponding values for H_χ metric are found to be 0.62, 0.26, and 0.17, indicating that the metasurface is developed from a non-hyperuniform to a near-hyperuniform state. The spectral density shift of $\chi_{S,max}$ is displayed in Figure 32d with respect to the filling factor, which is, in turn,

controlled by the deposition time. The average nanoparticle radius increases steadily with deposition time. The corresponding values are 29, 32, and 36 nm. Therefore, nanoparticle size can also be controlled in situ with the suggested growth method. Furthermore, ambient temperature change affects nanoparticle morphology and, consequently, the features inside the reciprocal space of the plasmonic metasurface. The corresponding experiment is conducted at an increased temperature of 50°C to demonstrate this. At higher temperatures, the growth rate is significantly enhanced, and strong coalescence of nanoparticles is observed. A typical SEM micrograph after 5 min of deposition can be seen in Figure 33a. The filling factor is about 58%.

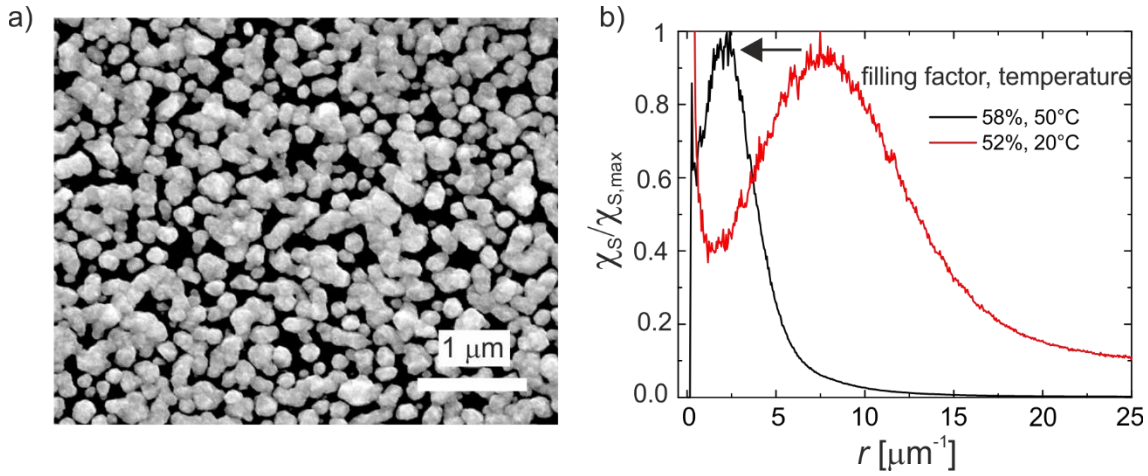

Figure 33: Deposition of AgNPs in darkness at a higher temperature: a) SEM micrograph after 5 min deposition at 50°C; b) the corresponding value of the normalized angular-averaged spectral density (black curve) compared with the spectral density obtained at room temperature (red curve).

By calculating the corresponding spectral density and comparing the value with one obtained in the experiment conducted at room temperature (20°C), the maximum peak shifts from 7.80 µm^{-1} to 2.30 µm^{-1} (Figure 33b). The value of H_χ is about 0.54, which is

higher than the value obtained at room temperature with a comparable filling factor, 58% versus 52%. To conclude, by changing the deposition time and temperature during fabrication in darkness, the degree of hyperuniformity and the position of the maximum $\chi_{S,max}$ can be controlled. It is important to note here that the cause of hyperuniformity of AgNPs grown in darkness from ELD solution is still unclear. It is assumed that the process of AgNP growth is governed by thermodynamic and chemical processes, which prohibit the simultaneous growth of two nanoparticles in the same place. There is a certain forbidden radius at which the closest nanoparticle can be formed. To prove this assumption, the following simulation is conducted. The nanoparticles are placed randomly on the area of 9.37×9.37 μm² one by one sequentially with a corresponding forbidden radius of r_o around the placed nanoparticle. Figures 34a - d show the resulting distribution of nanoparticle centers and corresponding structural factors. As can be seen, no features in reciprocal space are observed when the forbidden radius around nanoparticle centers is 1 nm. The hyperuniformity starts manifesting by increasing the forbidden radius further to 3, 9, and 12 nm.

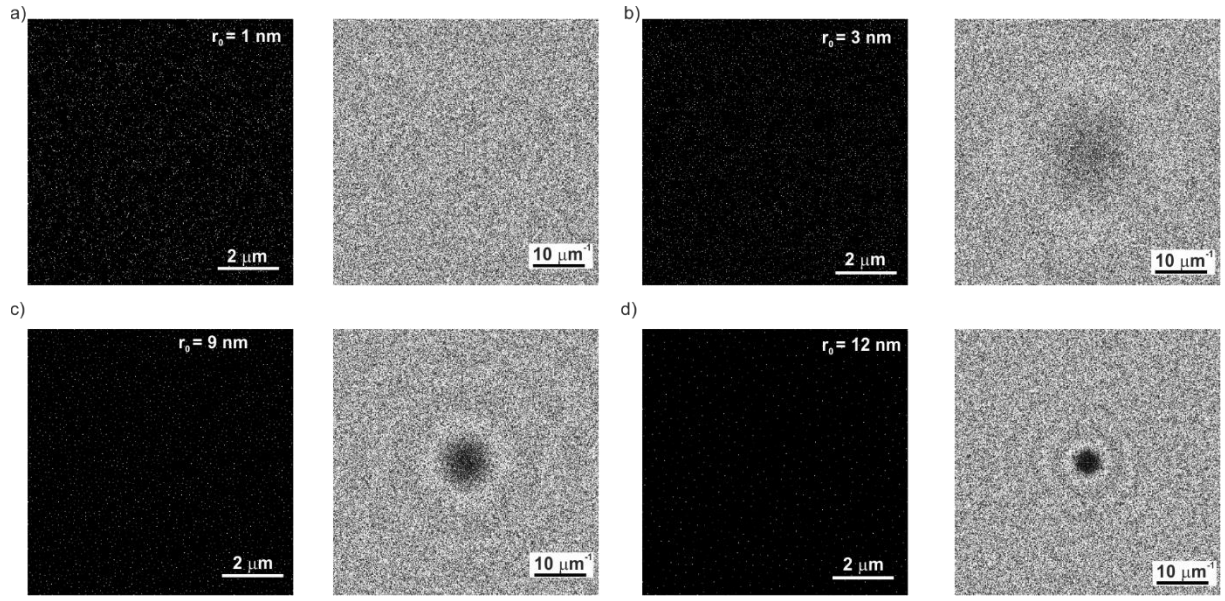

Figure 34: Result of simulation of nanoparticle growth in darkness: distribution of nanoparticle centers randomly placed on the area of 9.37×9.37 μm² with the corresponding calculation of structural factor for forbidden radii around the nanoparticles of 1 nm (a), 3 nm (b), 9 nm (c), and 12 nm (d).

As a result, the formation of AgNP distribution during the growth from the ELD solution is not a random process and obeys a rule defining the forbidden radius based on thermodynamic and chemical processes that should be investigated in detail as part of further work.

4.1.2 Disorder Engineering of Plasmonic Metasurfaces with Light

It was shown that AgNP deposition using an ELD solution could be controlled by light. When the ELD solution is cast onto the substrate surface in darkness, spontaneous formation of AgNPs occurs. Figure 35a shows the nanoparticle formation process described in Section 2.3.1. It schematically underlines the impact of light on non-stable nanoparticles below the critical size. Without light illumination, nanoparticles under

critical size are thermodynamically unstable (see Section 2.3.1) and are in constant competition between dissolving into atoms and statistical growth (Figure 35a, blue area). Once a nanoparticle overcomes its critical radius, it becomes stable, and the probability of shrinking into atoms is significantly decreased, enabling further non-reversible stable growth (Figure 35a, violet area).

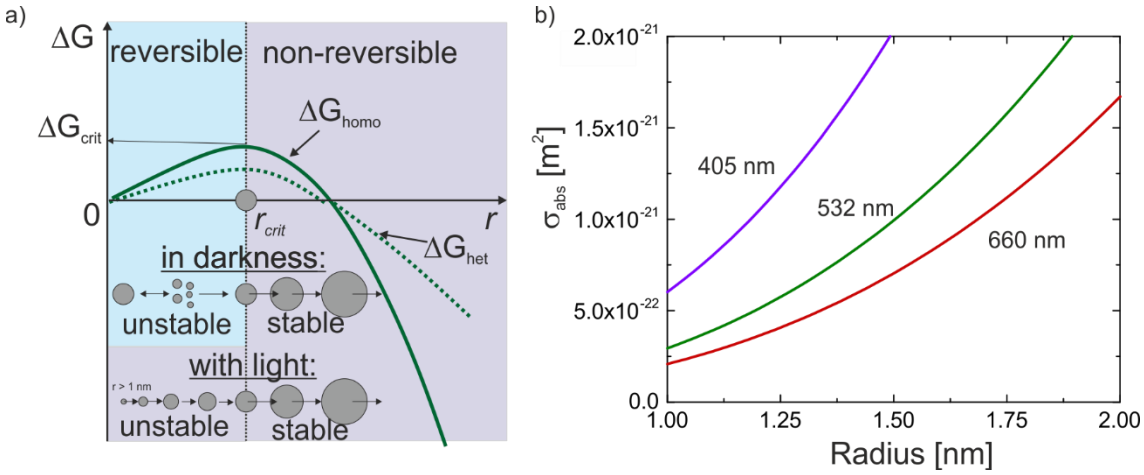

Figure 35: Growth of nanoparticle with and without light illumination: a) Gibbs free energy versus nanoparticle radius: under critical growth on a substrate surface (dashed line) and volume (solid line) with a schematic illustration of reversible and non-reversible growth in darkness and with light; b) absorption cross-section of AgNP calculated for nanoparticle in a water environment at different wavelengths.

Light illumination allows excitation of the LSP resonance, which delivers the energy and supports the growth of nanoparticles to an overcritical size. (Figure 35a, with light). Although AgNPs can statistically reach a stable nanoparticle size, positions with efficient LSP resonance excitation (local intensity hot spots) are energetically favored, and the growth rate is significantly enhanced there. Such intensity hot spots are defined by the interference pattern of scattered and incoming waves according to the description in

Section 2.3.3. LSP resonance at such spots can be excited once the AgNPs have statistically grown to a certain size. The reported value in the literature shows that nanoparticles at a radius of 1 nm can already support LSP resonance excitation[119]. The growth of AgNPs that are large enough to enable LSP excitation but still much smaller than the critical size can be mediated in two ways. First, the LSP delivers energy to the nanoparticle, thus energetically supporting its growth according to the plasmon-mediated growth described in Section 2.3.2. Figure 35b shows the absorption cross-section of AgNPs of different sizes from 1 nm at different exciting wavelengths. It can be seen that the probability of such excitation is higher for a lower wavelength. Second, the excitation of LSP resonance increases the adhesion between the excited AgNP and the surface[41], further decreasing the nanoparticle's free energy and critical size.

Plasmon-mediated growth continues until the AgNP reaches a size where the scattering dominates the absorption, so the amount of energy transferred to the nanoparticles decreases significantly[43,120]. Figure 36 shows the absorption and scattering cross-section for different excitation wavelengths (405, 532, and 660 nm). The simulation was performed for AgNPs in a water environment. The lower the wavelength, the lower the radius at which the scattering cross-section starts exceeding the absorption cross-section. The corresponding radius values are found to be 12, 17, and 21 nm. Therefore, the radius of the nanoparticle at plasmon-mediated growth is wavelength-dependent.

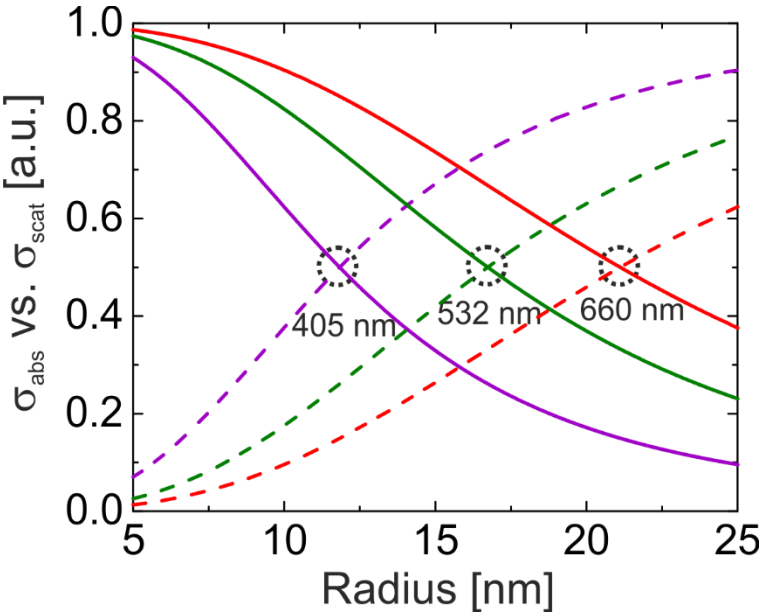

Figure 36: Absorption (solid lines) and scattering (dashed lines) cross-sections at different nanoparticle radii and wavelengths. The values were normalized by a sum of $\sigma_{abs} + \sigma_{scat}$.

The light can in situ control not only the spatial distribution of AgNPs by defining the hot spots on a substrate for the growth but also the influence the morphology of the growing nanoparticles. Together with plasmon-mediated growth of nanoparticles, different mechanisms, such as coalescence and Ostwald ripening, can also contribute to nanoparticle growth[121]. In summary, the proposed plasmon-mediated growth of AgNPs from the ELD solution under light exposure occurs in the following four steps:

1. Chemical reaction ($r \lesssim 1\ nm$) supported by light:

Details on the chemical reaction can be found in Section 3.1.4. As described, the addition of ammonia leads to the formation of the $[Ag(NH_3)_2]^+$ complex cation with a lower standard redox potential compared to Ag^+/Ag[122,123]. According to the literature[124], the $[Ag(NH_3)_2]$ complex cation involved in the chemical reaction can be excited by light,

followed by the reduction of the silver ions by glucose. Therefore, illumination may also support the chemical reaction. However, the main impact of the ammonia content in the proposed growth model is that it strongly reduces the reaction speed and, thus, the deposition rate.

2. Plasmon-mediated growth of unstable AgNPs ($1\ nm < r < r_{critical}$):

Unstable nanoparticles are already large enough for LSP excitation at local intensity hot spots.

3. Growth of stable AgNPs ($r < \lambda/2\pi$)[56]:

The stable nanoparticle keeps growing, increasing its radius and, at the same time, decreasing the nanoparticle absorption.

4. Termination of nanoparticle growth ($r \approx \lambda/2\pi$):

The scattering of nanoparticles dominates their absorption, causing a significant reduction in the growth rate.

In situ monitoring of plasmon-mediated growth of AgNPs from ELD is conducted experimentally with a Raman spectroscopy setup, described in Section 3.2.6. The ELD solution is cast on glass and illuminated from the top by a laser. Figure 37 shows the recorded Raman spectra during the deposition of AgNPs on glass.

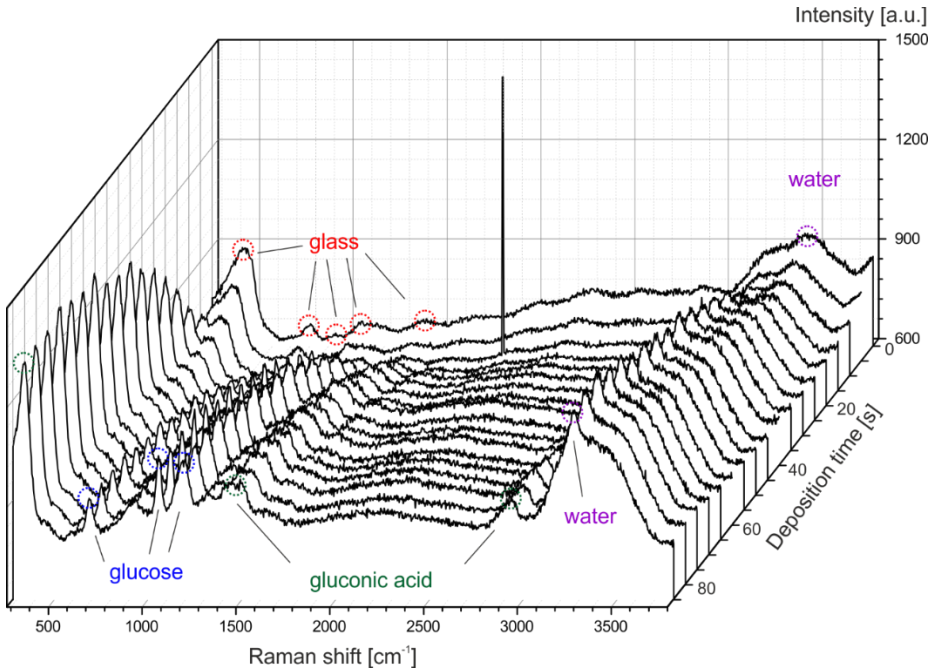

Figure 37. In situ Raman spectra during the growth of nanoparticles on a glass surface under laser illumination.

The laser wavelength of 488 nm is used. The power density is around 1.6 W/cm^2. The Raman spectrum is recorded every 5 s. As can be seen from Figure 37, at the moment of ELD casting on a glass surface (t = 0 s), a weak Raman signal from glass[125] (red dashed circles) and water[126] (violet dashed circles) is detected. After t ≈ 25 s of deposition, glass peaks get reduced. At the same time, characteristic peaks from glucose[127,128] (blue dashed circles) and water rise rapidly, meaning that the formation of the AgNPs on the glass surface occurs.

Moreover, the fingerprints of gluconic acid[129–131] (green dashed circles) as a product of silver reduction are found. For deposition time longer than t ≈ 35 s, peaks stay unchanged. Such an analysis is a powerful tool for studying in situ chemical reaction that is strongly linked to the final morphology of the plasmonic metasurface.

4.1.3 Isotropic and Anisotropic Stealthy Disorder Hyperuniform Plasmonic Metasurfaces

Precise control of light parameters makes it possible to fabricate a metasurface with a stronger form of hyperuniformity – stealthy hyperuniformity. In this case, the spectral density not only vanishes as k approaches zero, but is also suppressed within a particular region of reciprocal space[3], see Section 2.4.

At the lateral momentum of incident light being zero, it is first investigated experimentally how light polarization affects hyperuniformity. Preliminary experiments show that linear polarized light does not enable fabricating a metasurface, showing isotropic stealthy hyperuniformity[43]. In particular, Figures 38a - c illustrate the result of the calculation of spectral densities for plasmonic metasurfaces fabricated with linear polarized light at perpendicular incidence for different wavelengths ($\lambda_1 = 660$ nm, $\lambda_2 = 532$ nm, and $\lambda_3 = 405$ nm) on a glass substrate.

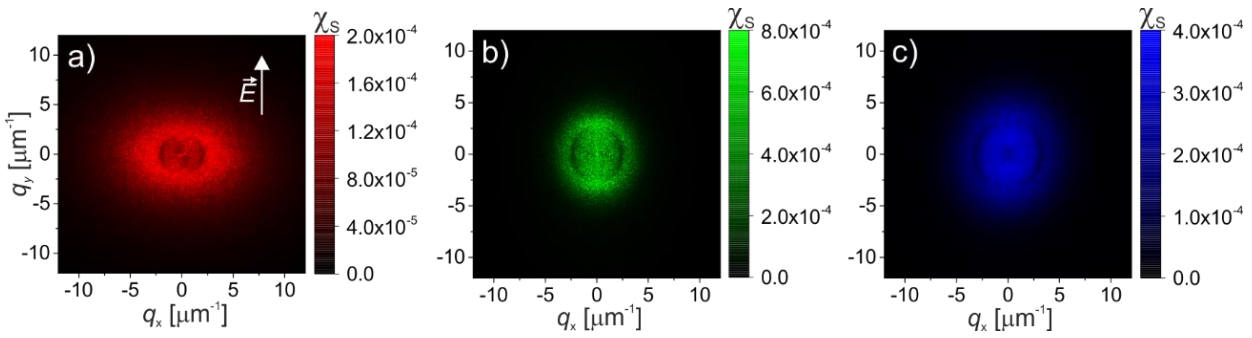

Figure 38: Spectral densities of AgNPs under linear polarized light with the wavelength of 405 nm (a), 532 nm (b), and 660 nm (c) at perpendicular incidence on a glass substrate.

More details about the experiment can be found in Section 3.1.5. Here, perpendicular incidence ensures that the lateral momentum of light ($k_{\parallel}$) is zero. In this case, inside the

reciprocal space, there are two pronounced moon-like dark areas shifted symmetrically with respect to the polarization direction marked by a white arrow. At the same time, by using circularly polarized light, stealthy hyperuniformity is induced, and rotational symmetry is also achieved. Figures 39a,c, and e show the SEM micrographs of plasmonic metasurfaces fabricated with circularly polarized light. Corresponding graphs of spectral densities show a disk with reduced values (Figures 39b,d, and f). The radii $\hat{r}$ of the disks are scaled by the laser wavelength inside the ELD solution and are defined as:

$$\hat{r}_i = \frac{n_{ELD}}{\lambda_i}, \; i = 1,2,3 \tag{1.61}$$

with a refractive index of $n_{ELD} \approx 1.336$, corresponding to the refractive index of the ELD solution. The broad minimum in the spectral density observed in Figures 39b,d, and f allowed hyperuniform metasurfaces to be referred to as quasi-stealthy. Suppression of the spectral density to zero is impossible in real experiments not only due to finite-size effects but also due to other contributions such as imperfections, missing structural elements, and others.[27] The manifestation of quasi-stealthy hyperuniformity indicates that the circularly polarized light induces short-range ordering of AgNPs during growth without long-range translational order. Based on the dependency (1.61) between disc radius and wavelength follows that short-range order is governed by the interference between incident light and scattered light from existing AgNPs (Section 2.3.3). It is important to note that the formation of the donut-like shape of the spectral density maximum allows forming of isotropic photonic bandgaps[132]. In analogy with a diffraction grating, such a metasurface exhibits isotropic diffraction with only one diffraction order.

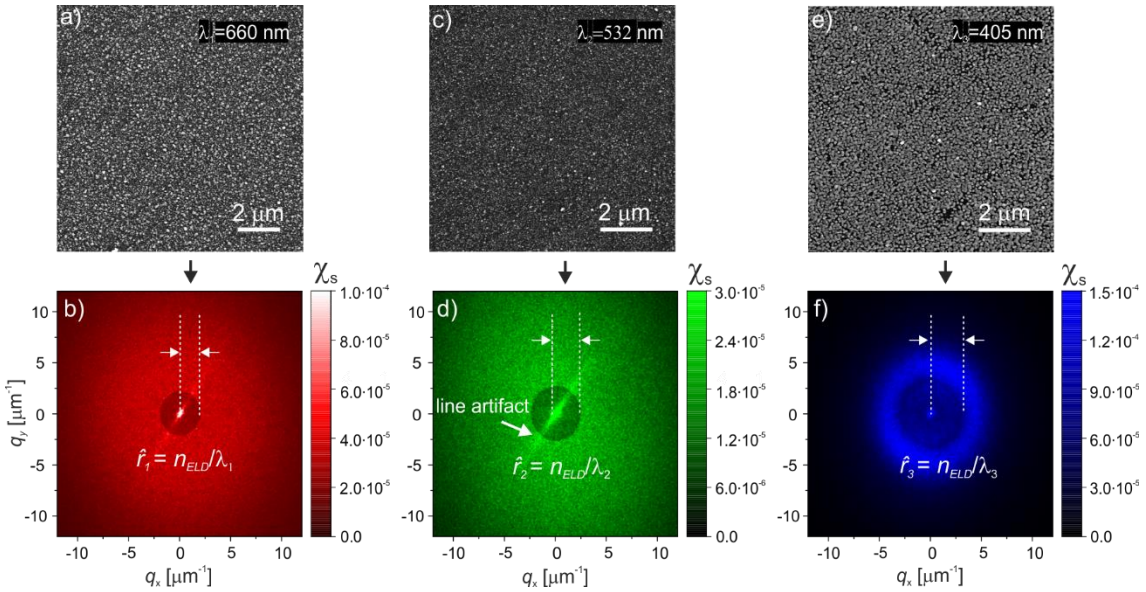

Figure 39: Stealthy hyperuniform metasurfaces fabricated with circularly polarized light of wavelengths 660 nm (a), 532 nm (c), and 405 nm (e) with corresponding spectral densities (b ,d ,f).

As expected, the nanoparticle size dependency on the wavelength is observed in the current experiment. A lower wavelength is associated with a smaller nanoparticle radius when identical conditions are followed. However, the average nanoparticle radii are found to be 19, 17, and 37 nm for the 405, 532, and 660 nm lasers, respectively. Because of the strong influence of the wavelength on absorbance, the nanoparticle size at 405 nm is larger than expected. Compared to 532 nm and 660 nm lasers, a 405 nm laser has a much higher absorbance (Figure 36).

Another point to discuss is the manifestation of the bright, thin line in the center of the reciprocal space in Figures 39b,d. The line suppresses hyperuniformity in a particular direction. Similar artifacts have been observed for experiments conducted in darkness in Figures 31b and 32c. Hence, the direction of the line is independent of the properties of

the light. Since this effect completely disappears for stronger adhesion of AgNPs when blue light is used for deposition, it can be presumed that post-treatment of the glass substrate after deposition is crucial for the appearance of such artifacts. Mainly, a correlation was observed between the removal direction of the samples from the cleaning water after deposition and the direction of the line artifact in the reciprocal space. As a result, low adhesion of AgNPs and mechanical manipulation of the sample after it has been removed from the solution leads to morphology changes, similar to the change in morphology caused by humidity or water on AgNP adhesion.[23]

It is well known that AgNPs are extraordinarily efficient at absorbing and scattering light. Even though AgNPs have a more intense and sharp plasmonic resonance than AuNPs, they cannot be applied in biotechnology due to their high toxicity. Moreover, AuNPs have advantages over AgNPs because of their affinity with the human organism, stability, and ability to interact with various substances. To extend our approach to the field of biotechnology for sensing[133], imaging[134], therapy[135], drug delivery[136] and etc., a plasmon-mediated synthesis of AuNPs has been developed based on the reduction of gold chloride with sodium citrate[108]. The AuNPs have been deposited according to the procedure described in Section 3.1.5. The obtained metasurface of AuNPs was examined afterward by SEM. The resulting SEM micrograph is shown in Figure 40a. A polydisperse distribution of nanoparticles is observed (Figure 40b). The average nanoparticle radius is around 50 nm and can be varied by deposition time or volume ratio between Na_3-citrate and $HAuCl_4$. By increasing the amount of Na_3-citrate from 0.2 mL to 0.4 mL, the corresponding average radius of the nanoparticle was decreased to 25 nm.

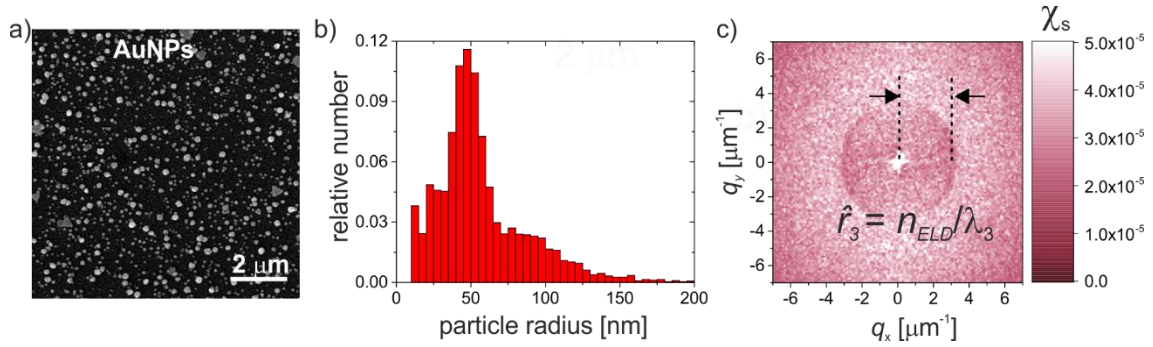

Figure 40: Fabrication of plasmonic metasurface with AuNPs under illumination by circularly polarized 405 nm laser: a) resulting SEM micrograph; b) radius distribution; c) spectral density.

Similar to the AgNPs, the AuNPs form a metasurface with features of engineered disorder – isotropic stealthy hyperuniformity. Figure 40c illustrates the spectral density calculated from the measured SEM micrograph. It represents a disk of reduced values of spectral density. As before, the radius of the disc $\hat{r}_3$ is defined through the laser wavelength of 405 nm, indicating a similar alignment process with light as for AgNPs. Further experiment optimization is required to suppress the spectral density values within the disc to realize a plasmonic metasurface based on AuNPs with stealthy hyperuniformity.

After a discussion of polarization and wavelength impact on the features inside the reciprocal space, the focus will be shifted to the lateral momentum of light. As predicted theoretically, anisotropic stealthy hyperuniformity can occur in disordered nanoparticle systems under excitation with maximum lateral momentum[92], which can be achieved through SPP excitation. To prove this, light-controlled growth of AgNPs under SPP excitation is experimentally conducted. An SPP waveguide structure prepared according to the description of Section 3.1.1 is used. To excite SPPs, the ATR setup using a sapphire prism is applied (Section 3.2.2). In this case, the lateral momentum of light is $k_{\parallel} = k_x =$

k_{spp}. Figure 41a shows a schematic illustration of the experimental setup with the sapphire prism and SPP waveguide structure accompanied by a photograph of the substrate showing AgNP growth under SPP excitation from the topside. As shown in Figure 41b, there is no spatial order in the SEM micrograph of the resulting metasurface. However, spectral density calculations reveal two distinct dark disks shifted symmetrically along the q_x-axis (Figure 41c). Such observation is described theoretically as anisotropic stealthy hyperuniformity, where hyperuniformity is induced only in one particular direction and is absent in other directions.[3], [18]

The shift $\pm\hat{r}_{\parallel}$ and the radius $\hat{r}_{spp}$ of the disks are equal and defined as:

$$\hat{r}_{\parallel} = \hat{r}_{spp} = \frac{1}{\lambda_{spp}}. \tag{1.62}$$

Unlike experiments involving dark growth and light-controlled growth in perpendicular incidence ($k_{\parallel} = 0$), the metasurface with maximum lateral momentum exhibits anisotropic stealthy hyperuniformity.

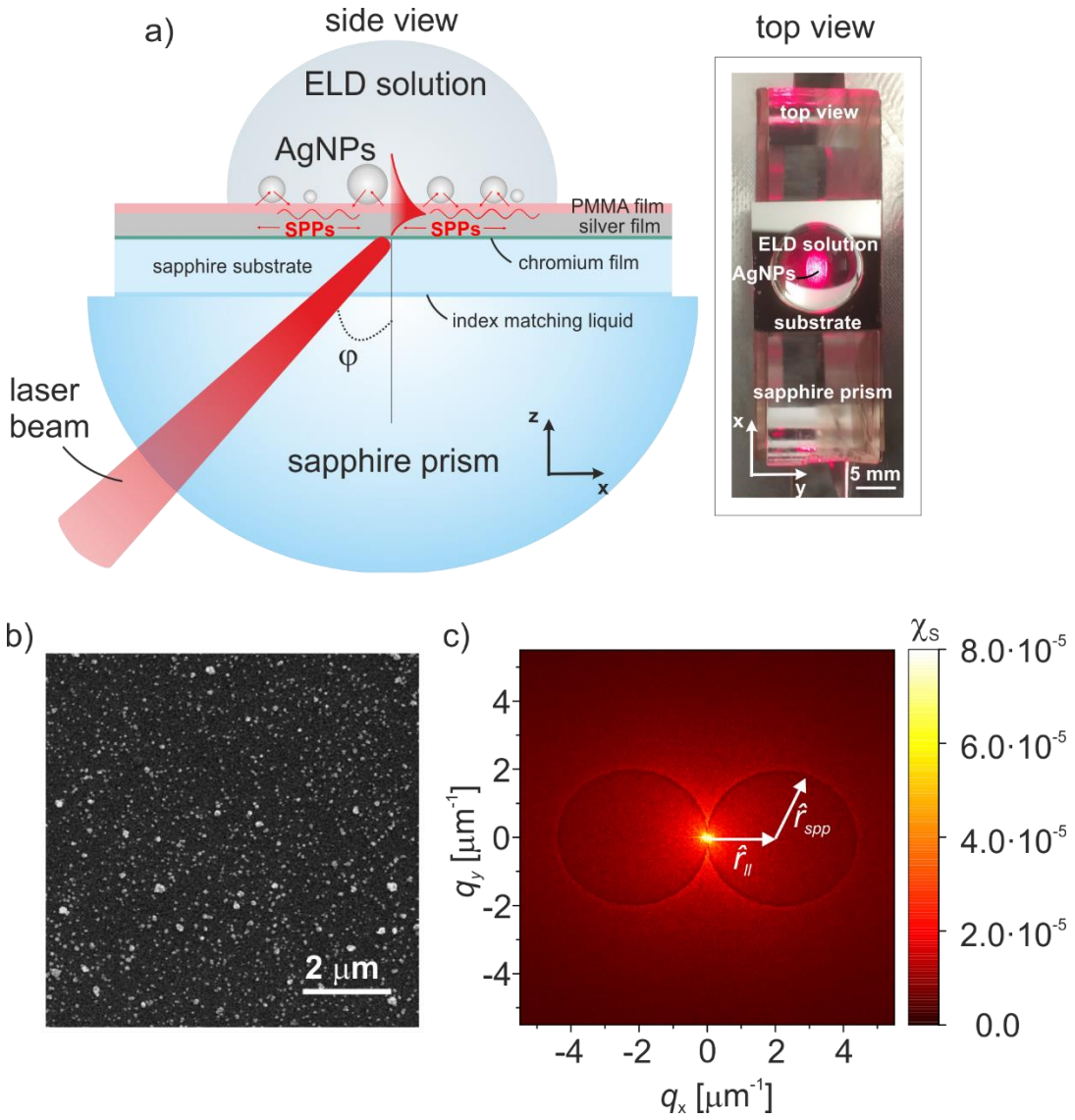

Figure 41: Light-controlled growth of metasurfaces via SPPs showing anisotropic stealthiness: a) a sketch of the experimental setup in side view and a photograph showing the top view; b) a typical SEM image of the resulting metasurface; c) the corresponding spectral density.

It is important to note that oblique light ($k_{\parallel} > 0$) can ensure a symmetrical shift of the two disks, as demonstrated in previous works[43]. For example, using a high-index sapphire substrate leads to an accessible incident angle of around 59° at which the disks touch each

other at $q_x = 0$ and $q_y = 0$ inside the reciprocal space. However, in this case, the dark disks develop into dark circles for large incident light angles, so anisotropic stealthy hyperuniformity cannot be achieved[43].

The transformation of disks into rings is also observed for experiments with SPP excitation. In particular, disks are developed into rings for longer deposition times. Figures 42a - d demonstrate how the disks develop in reciprocal space during the deposition time of 0.5 to 12 min. For short deposition times (≤ 0.5 min), the disks are barely visible (Figure 42a). The most prominent disc structure occurs between 3 and 5 min of deposition. The disk transformation into a ring takes place after 5 min of deposition. At a deposition time of 6 min, the rings get notably clear and sharp. For longer deposition times (≥ 12 min), the rings become fuzzy (Figure 42d) until they disappear into a closed silver film. Therefore, deposition time is the control parameter for in situ engineering of characteristic features inside the reciprocal space.

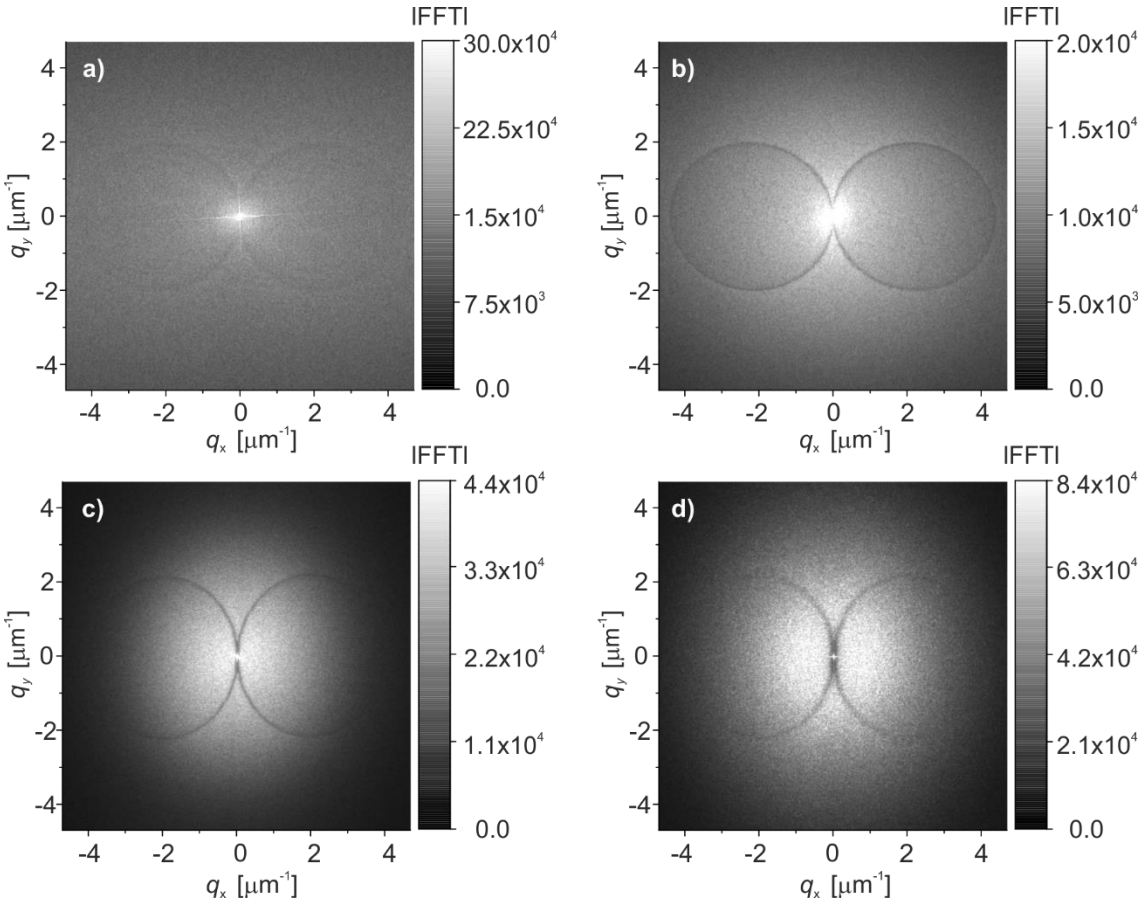

Figure 42: FTEMs of grown metasurface with different deposition times of 0.5 min (a), 4 min (b), 7 min (c), and 12 min (d).

In contrast to photonic excitation, under SPP excitation in all experiments, the circles have always been found to touch each other (Figure 42a-d). As no direct manifestation of the used light source (photonic features) is found in the FTEMs, and the direction and wavelength of the incident SPPs coincide with the direction of the ring shift and the ring radius, it is assumed that a near-range order is introduced by SPPs. Although it is not yet fully understood, the nanoparticle growth process can be explained as follows. During growth, AgNPs support LSP resonance excited by incident SPPs via their electromagnetic fields overlap. Reciprocally, LSPs mediate the scattering of the incident SPPs into

scattered SPPs of arbitrary lateral direction. The scattering process is visualized schematically in Figure 43a, where real and momentum space are shown. The incident SPP wave with the momentum of $k_{\parallel}$ is scattered into SPP waves with the momentum of $k_{spp} = k_{\parallel}$. The black circle in momentum space represents the scattering states defined along the ring of radius k_{spp} as: $k_x^2 + k_y^2 = k_{\parallel}^2 = k_{spp}^2$.

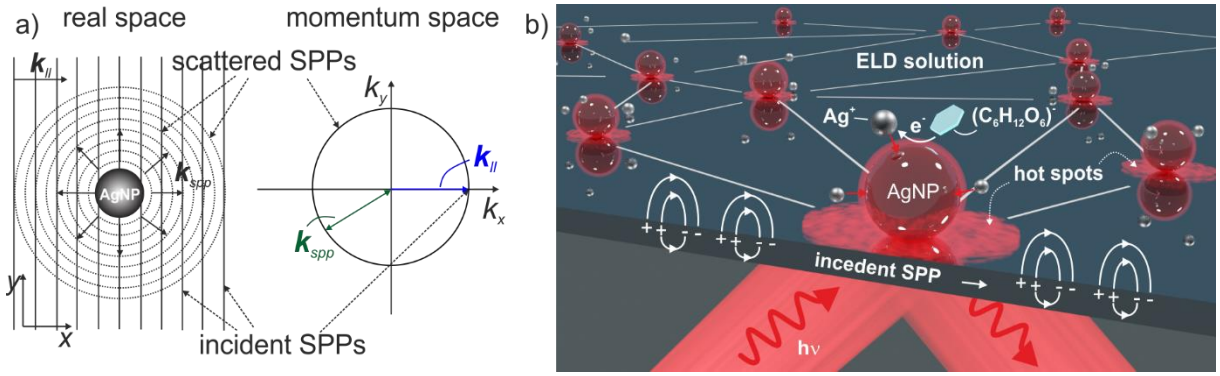

Figure 43: Principle of the SPP-induced growth: a) real and momentum space during the nanoparticle scattering process under SPP excitation; b) growing AgNPs forming a plasmonic metasurface of engineered disorder.

During scattering, the light frequency remains constant, and there is a fixed phase relationship between the incident and scattered SPPs. In the end, interference between incident and scattered SPPs occurs, leading to the formation of hot spots of maximized local electromagnetic field intensity, emphasized as red ellipses on the sample's surface in Figure 43b. At such spots, the nanoparticle growth rate is energetically favorable and significantly enhanced, see Section 4.1.2. After a nanoparticle reaches an over-critical size in such a spot, it becomes an additional, efficient source of SPP wave scattering, generating next-intensity hot spots for the growth of the next nanoparticle. In other words, the interference of SPPs dictates the positions of AgNPs on a microscopic scale,

which is emphasized by white lines between the particles in Figure 43b, indicating the formation of an interdependent network AgNPs.

The corresponding simulation based on light-controlled alignment description (Section 2.3.3) is performed to prove that the interference of scattered and incident SPPs governs the alignment of the nanoparticles. Figure 44a demonstrates a typical interference intensity map of scattering SPPs by nanoparticles during the alignment process calculated according to Section 3.3.1.

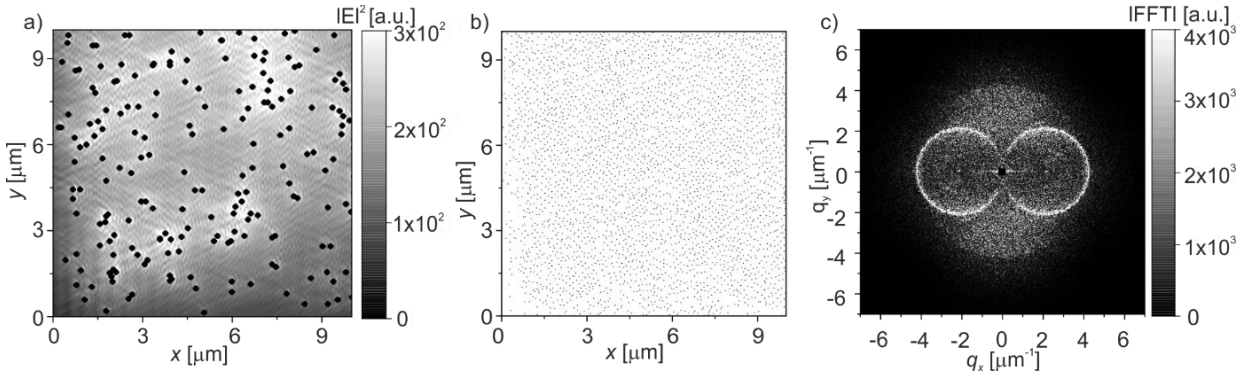

Figure 44: Result of the simulation of a local intensity map originated from scattered nanoparticles: a) field intensity map; b) nanoparticles placed one by one at intensity spots defined by intensity map (a); c) corresponding FFT calculated from the nanoparticle distribution (b).

The final nanoparticle distribution is shown in Figure 44b. The resulting FTEM has two symmetric circles touching each other at $q_x = 0$ and $q_y = 0$. The shift and radius of the circles are equal and scaled by the SPP wavelength (Figure 44c) according to the formula (1.62). It is important to note that independent of the number, position, and size deviation of the initial random scattering sources, the final pattern possesses the local intensity spots whose distribution yields two symmetrically shifted circles in reciprocal space. This

makes it possible to engineer the features inside the reciprocal space of a plasmonic metasurface and directly adapt it to a real application scenario.

4.2 Disorder Engineering via Hybridization of Surface Plasmon Polaritons

This section will further explore engineering of features inside the reciprocal space by SPP modes. In particular, the focus will be on the growth of AgNPs governed by hybridized SPP modes such as short-range and long-range SPP. It will be demonstrated how such engineering can be extended to a two-beam configuration at the end of the current section.

4.2.1 Multimode Engineering of Plasmonic Metasurfaces with Hybridized Modes

Here, it will be demonstrated that strong interaction between the incident SPP wave and growing nanoparticles causes the excitation of hybridized modes that can be visualized in reciprocal space by analyzing the grown nanoparticle distribution in real space. AgNP growth is induced at the SPP waveguide (Section 3.1.5) with a reduced thickness of the silver film compared to the experiments of Section 4.1 conducted at the thickness of 54 nm. The experimental ATR setup shown in Figure 41a is used here. FTEMs of plasmonic metasurfaces deposited using the p-polarized lasers with a wavelength of 532 and 660 nm are shown in Figures 45a and b. The corresponding silver film thicknesses of the SPP waveguide are 35 and 40 nm, respectively. The FTEMs reveal four distinct dark symmetrical rings of different radii, denoted as $\hat{r}_{SRSPP}$ and $\hat{r}_{LRSPP}$. The rings are symmetrically shifted along the $\pm q_x$-axis and have a common center, indicating the same excitation momentum: $k_{in} = 2\pi \cdot \hat{r}_{in} = k_0 \cdot n_{prism} \cdot \sin(\varphi)$. The radius of two touching rings $\hat{r}_{LRSPP}$ scales with the SPP wavelength $\hat{r}_{LRSPP} = {\lambda_{spp}}^{-1} = \frac{n_{eff,LR}}{\lambda_0}$, similar to the results in Figure 42 according to equation (1.62).

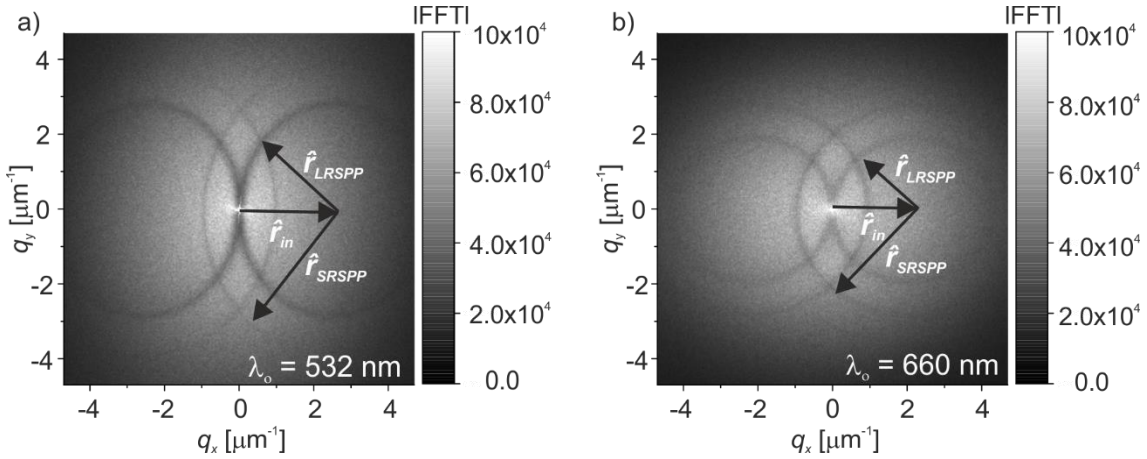

Figure 45: FTEMs of plasmonic metasurface grown via SPP modes excited using lasers with a wavelength of 532 (a) and 660 nm (b) on silver films with thicknesses of 35 and 40 nm, respectively.

At the same time, non-touching rings with a radius of $\hat{r}_{SRSPP}$ correspond to a scattered wave with an effective refractive index of $n_{eff,SR}$, which is $\hat{r}_{SRSPP}/\hat{r}_{LRSPP}$ times higher than $n_{eff,LR}$. The excitation of such a mode in an SPP waveguide using the ART setup configuration with a sapphire prism is impossible due to the momentum conservation mismatch: $k_{in} \ll k_0 \cdot n_{eff,SR}$. Therefore, this mode excitation can occur only during AgNP growth. In this case, the nanoparticle alignment process can be explained as follows. First, it is assumed that the growth of AgNPs from the ELD solution is initiated by the SPP mode (Figure 46a). The LRSPP has a considerably smaller fraction of fields inside the silver film[61].

Moreover, LRSPPs have large penetration depths normal to the propagation direction, in the range of micrometers, which can be used for sensing applications to detect the changes in the volume of the test medium. When a nanoparticle size on a surface reaches a particular value (Section 4.1.2), the coupling between SPP and LSP in AgNPs takes place

with subsequent back-coupling to either the LRSPP or the SRSPP mode (Figure 46b) with arbitrary momentum directions. Contrarily to LRSPP, SRSPP has a much higher propagation loss[68] due to the stronger field confinement to the metal surface, which makes it possible to use SRSPP to detect slight changes at the metal surface[64]. Moreover, excitation of both modes having the same frequency but propagating with different phase speeds allows the detection of multiple analytes simultaneously, known in the literature as surface-multiplasmonic sensing[137,138].

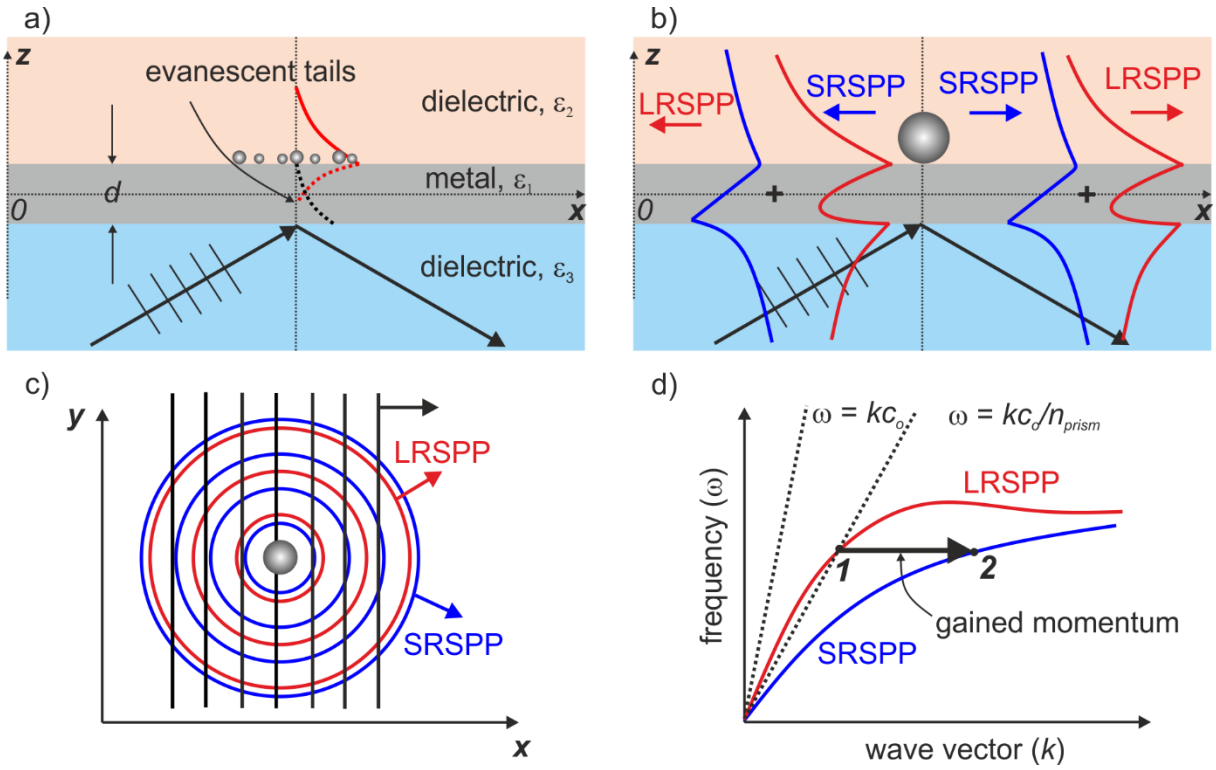

Figure 46: Schematic illustration of the formation of double rings in reciprocal space: a) initiation of the nanoparticle growth: b) excitation of LSP in nanoparticles and back-coupling into LRSPP (red) and SRSPP (blue) modes; c) wave front profiles of the LRSPP and SRSPP modes; d) dispersion diagram representing the LRSPP and excitation of the SRSPP mode by nanoparticles with the gained momentum marked by a black arrow.

Figure 46c shows the wave fronts of the back-coupled LSP modes into propagating LRSPP (blue ring) and SRSPP (red ring) modes schematically, together with the wave front of the exciting wave (black lines) in the xy-plane. Afterward, the formation of an interference pattern by the incident and scattered waves occurs with subsequent nanoparticle alignment processes according to the theory described in Section 4.1. In the end, the resulting nanoparticle distribution saves information about both modes in the form of their positions on an SPP waveguide surface. The described process can also be illustrated in a dispersion diagram of LRSPP and SRSPP modes (Figure 46d).

Additionally, light lines in the vacuum and inside the prism are added (Figure 46d, dot lines). The initial excitation state is marked with "1". State "2" indicates the excitation of SRSPP. This state cannot be achieved in the current ATR configuration due to the momentum mismatch. At the same time, the black arrow represents a gained momentum by grown nanoparticles to excite the SRSPP mode. This assumption agrees with the experiment where the manifestation of the non-touching rings or the SRSPP mode on FTEMs takes place after a particular deposition time.

4.2.2 Simulation Results of Surface Plasmon Polaritons Hybridization and Comparison to the Experiment

Generally, the silver film between two dielectrics can support the bound-to-metal SPP modes propagating at both dielectric/metal interfaces. The corresponding dielectric constants are denoted here as ε_1, ε_2, and ε_3, see Figure 46a. When the thickness of the metal film is reduced, the evanescent fields of the modes start overlapping, leading to mode hybridization and subsequent formation of the LRSPP and SRSPP modes. Figures 47a and b show the numerical solutions of the dispersion relation (1.23) for both

modes at different silver film thicknesses d from 10 to 70 nm and laser wavelengths 532 and 660 nm. The result of the dispersion calculation is obtained for the dielectric constant of the ELD solution $\varepsilon_2 = \varepsilon_{ELD} = 1.336$, measured using Michelson interferometry (Section 3.2.3). The graphs are plotted in real wavenumbers normalized to the wavenumber of a single interface SPP at $\varepsilon_1/\varepsilon_2$. It becomes apparent: the shorter the wavelength, the higher the cut-off thickness of mode hybridization. For 660 nm, it is 45 - 50 nm, and for 532 nm, it is 50 - 55 nm (Figures 47a,b). Below the cut-off thickness, the SRSPP mode (upper curves) starts deviating significantly stronger than the LRSPP mode (lower curves) by approaching lower thicknesses. Above the cut-off thickness, the modes are degenerated and described by the dispersion relation for a single interface.

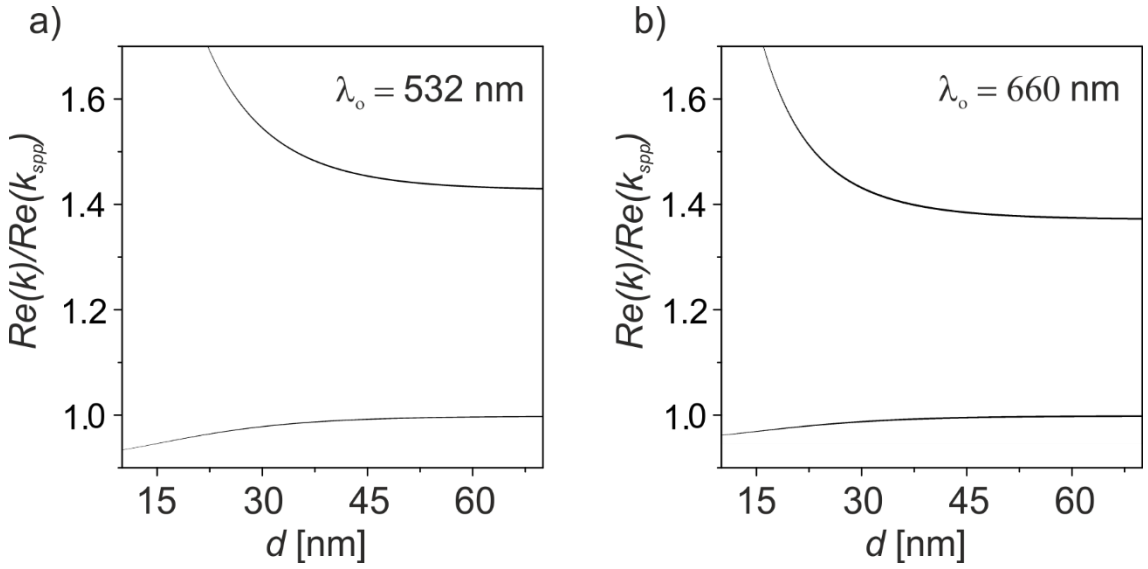

Figure 47: Dispersion relation for the normalized wavenumbers in a thin silver metal film of various thicknesses, calculated for the excitation wavelengths of 532 nm (a) and 660 nm (b) at the dielectric constant ε_2 corresponding to ELD solution.

According to the suggested theory, the radius of rings linked to the wavenumber should

follow the simulated dispersion curve by changing the thickness of the silver film. To prove this assumption, the corresponding experiments at different thickness films are conducted for the p-polarized laser with wavelengths of 532 and 660 nm. The corresponding radii are measured from FTEMs. The radii then are transformed to the wavenumbers and normalized to the wavenumber corresponding to a non-hybridized SPP mode at a single interface $\varepsilon_1/\varepsilon_2$. The resulting values are added to the dispersion curves simulated above (Figures 47a,b). Figure 48 represents the normalized radius values: red points for touching rings and black squares for non-touching rings.

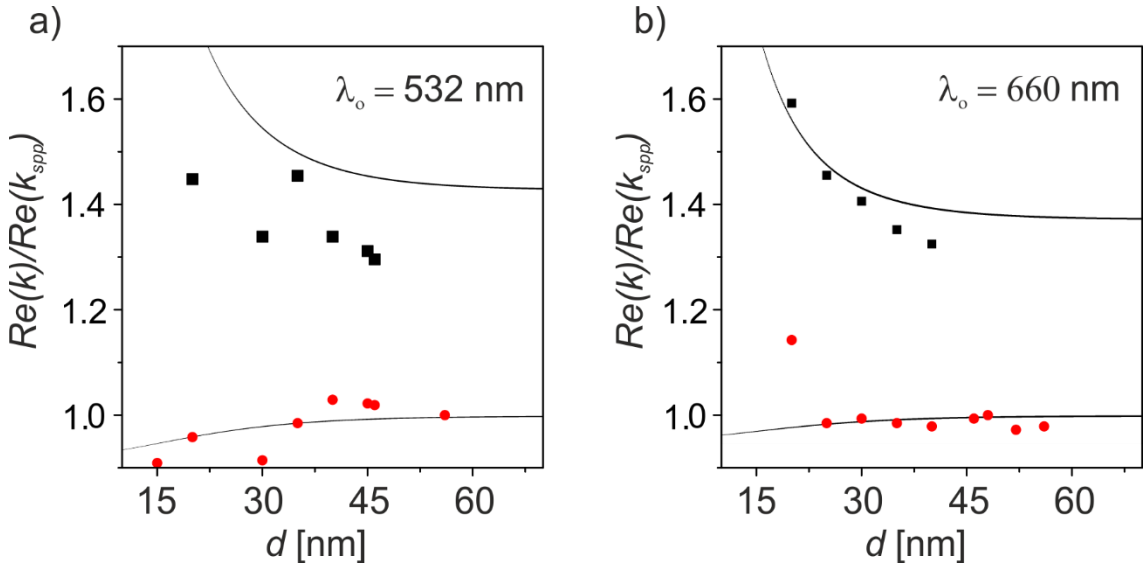

Figure 48: Comparison of simulated dispersion curves and the ring radii extracted from FTEMs obtained at various thicknesses and excitation wavelengths of 532 (a) and 660 (b) nm.

As shown, the plotted radii follow the simulated dispersion curves. However, some deviations can be observed. For a wavelength of 532 nm, more substantial deviations in measurements can be observed than for a wavelength of 660 nm. Such deviations can be attributed to the experiments being conducted at slightly different deposition parameters

than expected, such as the ELD solution content, the film thickness, roughness, the SPP excitation condition, and other aspects. The mode hybridization for 532 nm occurs at a higher cut-off thickness than for 660 nm, which agrees with the simulated dispersion curve behavior. In particular, the non-touching rings disappear for a 532 nm and 660 nm laser at a thickness of 54 nm and 45 nm, respectively. Only touching rings are observed for thicknesses higher than the cut-off value. It is important to note that most radii obtained from the experiments fit the theory. However, a substantial deviation from the simulated dispersion curves is observed at a low thickness of the silver film, i.e., below 23 nm. It is especially remarkable for the 660 nm laser at a thickness of 20 nm. It is assumed that the film cannot be considered a closed and smooth film at such thickness, and the dispersion relation (1.23) is not fulfilled in this case.[62,139]

4.2.3 Hybridized Modes with Two-Beams Configuration

The experiments in a double-beam configuration are conducted to further explore the growth method with SPP modes using a thin silver film. The SPP waveguide with a silver film thickness of 35 nm was used here for nanoparticle deposition. At this thickness, the SPP waveguide supports hybridized modes for both wavelengths of 532 and 660 nm (Figure 48a,b). First, the ELD solution is cast on the SPP waveguide surface, and deposition is conducted first by a 660 nm laser at the incident angle of φ_r (Figure 49a). Then, the ELD solution is removed, and the sample with AgNPs is rotated by $\Delta\theta_{xy} = 95°$ in the xy-plane with respect to the azimuth angle (Figure 49a). Next, the incident angle φ_g is adjusted to a 532 nm laser, and a new drop of ELD solution is added on top of the SPP waveguide surface with AgNPs. Here, the existing nanoparticles grown using a 660 nm laser are considered a random scattering source for a 532 nm laser.

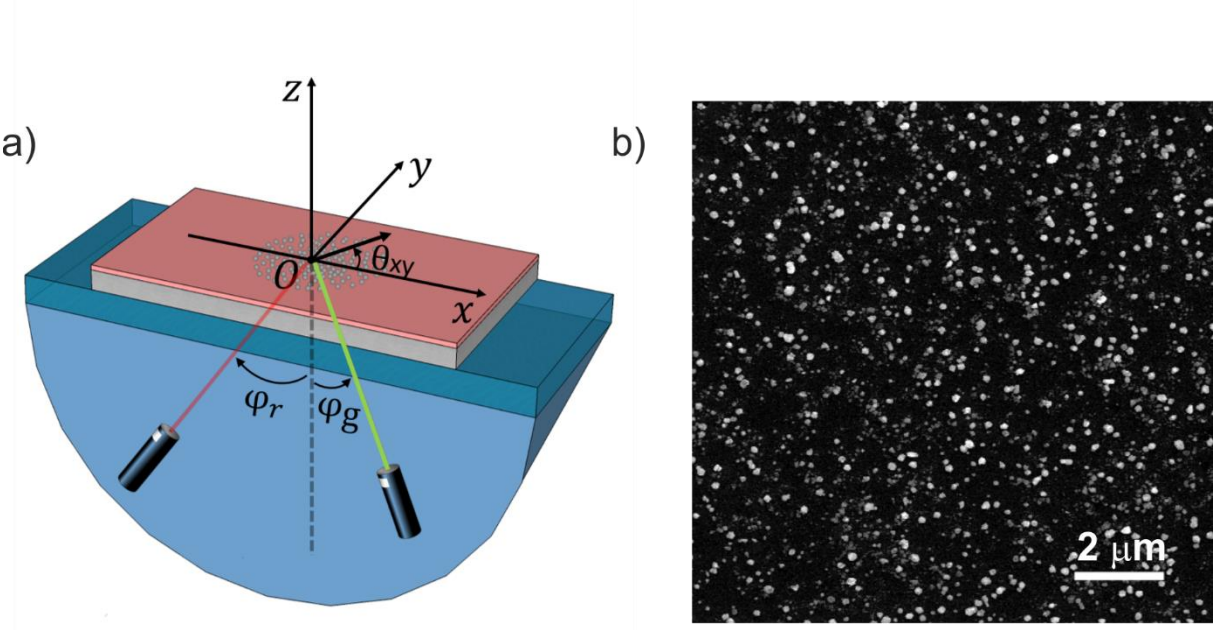

Figure 49: Engineering of ring features inside the reciprocal space by hybridized multi modes: a) experimental setup of a two-beam configuration: two lasers of 532 and 660 nm are set to different incident angles and used sequentially one after another after rotating the sample by $\Delta\theta_{xy}$ = 95° in xy-plane; b) the resulting SEM micrograph of the grown nanoparticles.

As discussed, the growth method is robust against surface imperfections and adapts to the electromagnetic environment during nanoparticle deposition. The resulting SEM micrograph after deposition with the corresponding histogram of the nanoparticle radii is analyzed. Two types of nanoparticles are distinguishable in a real-space SEM (Figure 49b). The histogram illustrates the two maxima of different radii that can be assigned to the individual wavelengths used for nanoparticle deposition (Figure 50a).

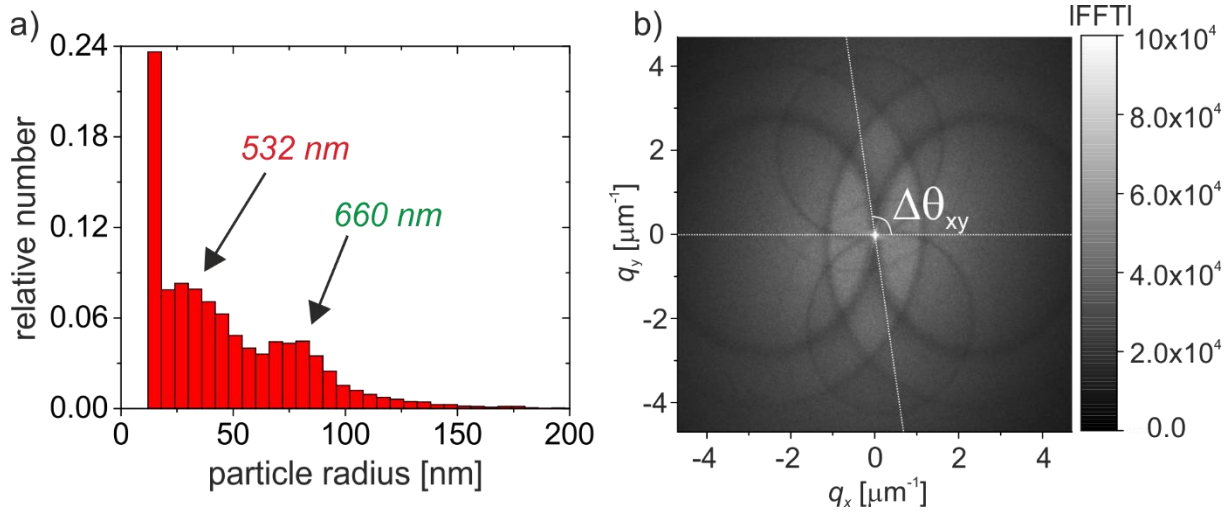

Figure 50: Fingerprints of the nanoparticles grown with two-beam configuration: a) histogram of the nanoparticle radii; b) averaged FTEMs of real-space SEMs.

At the same time, the FTEM reveals the fingerprints from four hybridized modes involved in the alignment process during nanoparticle growth from the ELD solution (Figure 50b). Every ring pair attributed to the lasers is rotated by around 95° to each other and symmetrically shifted with respect to the q_x and q_y axis in the FTEM. In this way, in addition to the electromagnetic environment, the information about the mechanical alignment with respect to the excitation light source is also stored in the form of the nanoparticle positions. Slight mechanical detuning of the substrate by a certain angle leads to a corresponding ring rotation in reciprocal space. The additional degree of freedom makes it possible to excite various hybrid modes propagating in different directions with corresponding mode profiles, depths of penetration, and effective mode indices. This opens a new avenue for further exploration of multiplasmonic sensing.

4.3 Robust Optical Sensors based on Disorder-Engineered Plasmonic Metasurfaces

In previous chapters, it was shown that strong coupling between SPP and LSP modes[140] leads to controlled nanostructuring on a microscopic scale, enabling the engineering of sharp features inside the reciprocal space. This allows for the direct application of plasmonic metasurfaces as optical refractive index sensors.

4.3.1 Disorder-Engineered Plasmonic Metasurfaces for Sensing Application

The development of the features inside the reciprocal space of a plasmonic metasurface during AgNP growth from ELD solution toward a sharp ring structure over time under SPP excitation was discussed in Section 4.1. The optimum deposition time was found to be between 5 and 7 min. Along with deposition time, the excitation efficiency of SPPs and incident power density are important parameters that impact the formation of the sharp ring structure in reciprocal space. The excitation efficiency of SPPs (η) is expressed with the following equation:

$$\eta = 1 - \frac{P(t=0)}{P_o}, \tag{1.63}$$

where P_o is the reflected power of the incident light measured before the ELD solution is dropped, and P is the reflected power of the incident light measured at the moment of deposition time $t = 0$ when the ELD solution is dropped onto the surface. The pronounced ring structure is obtained at the excitation efficiency of SPPs above 80%. Below this value, the rings are barely visible in reciprocal space and are not applicable for sensing applications. Figure 51 presents different growth scenarios at different excitation power densities.

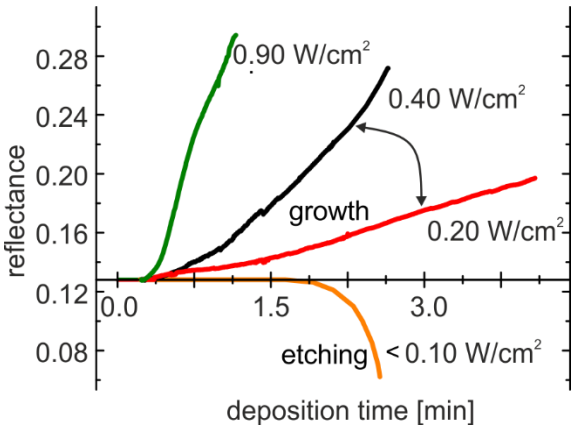

Figure 51: Reflectance measured during the growth induced by SPP excited at different power densities at an initial excitation efficiency above 80%.

Depending on the initial excitation power density, the slope of the reflectance curve varies. The optimum power density stays between 0.2 - 0.4 W/cm². At higher values, random chains and islands of AgNPs are formed. At a power density below 0.10 W/cm² (Figure 51, orange curve), a partial etching of the closed silver film is observed instead of growth. The corresponding reflected power drops down. Similar etching by ELD solution is observed without laser irradiation in darkness. Such behavior is observed for silver films exposed to the atmosphere for a certain time, particularly more than three days after PVD evaporation. No etching is observed for fresh samples either in darkness or under low power density. It could be explained as follows. The close silver film exposed to the atmosphere forms a native oxide layer AgO_x. In darkness or low power density, once the drop of ELD solution is cast on top of the SPP waveguide, it diffuses through the PMMA film and dissolves the AgO_x forming a diamine complex $Ag[(NH_3)_2]$. The thickness of the silver film is reduced, and the silver gets etched. At the same time, at SPPs excitation with sufficient power density, the reduction of silver oxide by glucose is enhanced, and the

native oxide layer is immediately reduced to silver. No dissolving of silver oxide appears. The plasmonic metasurface deposited for 6 min with SPPs excited at a power density of 0.20 W/cm², and an excitation efficiency of 82% on top of the SPP waveguide using an ATR setup is applied here for sensing an aqueous solution. The SEM micrographs of the prepared plasmonic metasurface with AgNPs, here referred to as structural elements, are shown in Figures 52a,c.

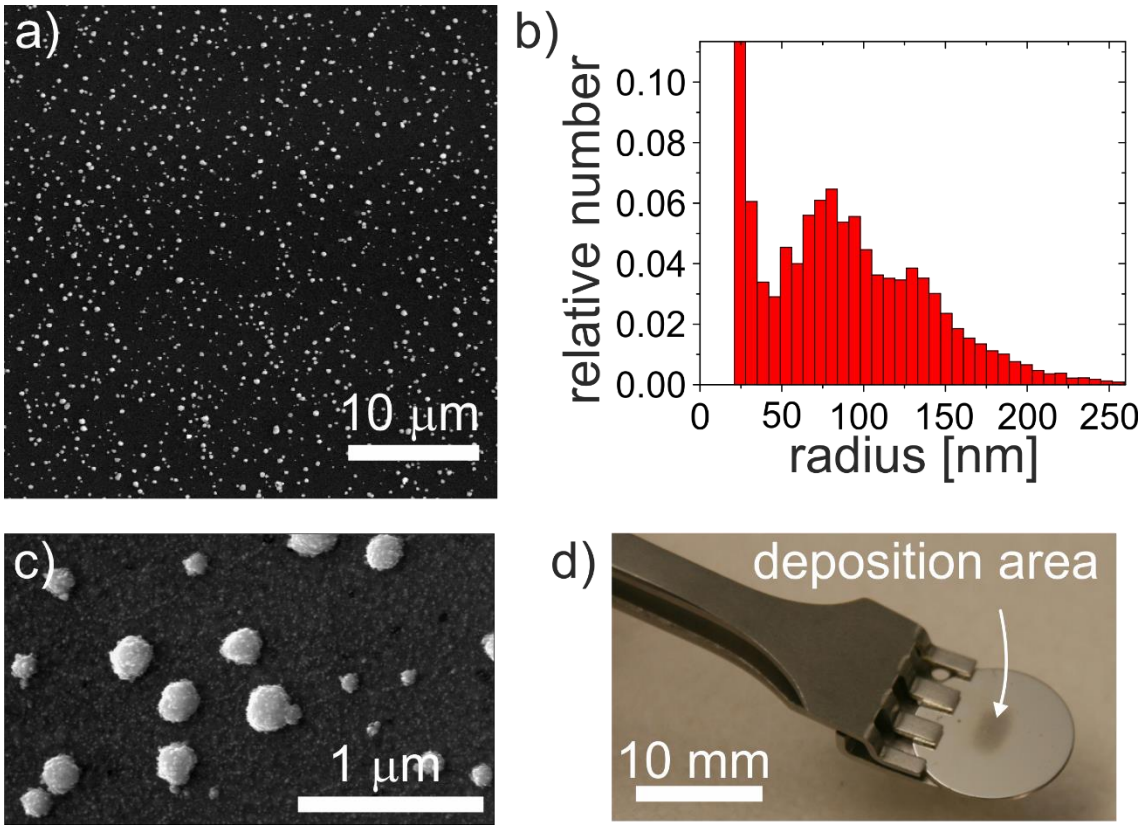

Figure 52: Analysis of the plasmonic metasurface after deposition of AgNPs: a) real-space SEM of the resulting nanostructures; b) the histogram of a relative number of particles with the corresponding radii; c) SEM micrograph with structural elements of the plasmonic metasurface; d) photograph of an entire sample after the deposition of AgNPs.

The nanoparticles have a broad distribution in size, as seen in the corresponding histogram in Figure 52b. The average nanoparticle radius is around 92 nm. Figure 52d displays a photograph of the entire sample after the deposition of AgNPs. At the same time, the corresponding FTEM of the plasmonic metasurface (Figure 53a) reveals two pronounced symmetrically shifted rings touching each other at $q_x = 0$ and $q_y = 0$ indicating an engineered disorder induced by SPPs during nanoparticle growth (see Section 4.1). Such rings are referred to as structure rings. The radius of the rings is denoted as $\hat{r}_S$, a shift from the center coordinates as $\hat{r}_{in}$, and the average width as $\Delta\hat{r}_s$, corresponding to the full width at half maximum of the profile cut of the Fourier amplitude. The radii $\hat{r}_{in}$ and $\hat{r}_S$ are equal and scaled with the SPP wavelength, see equation (1.62).

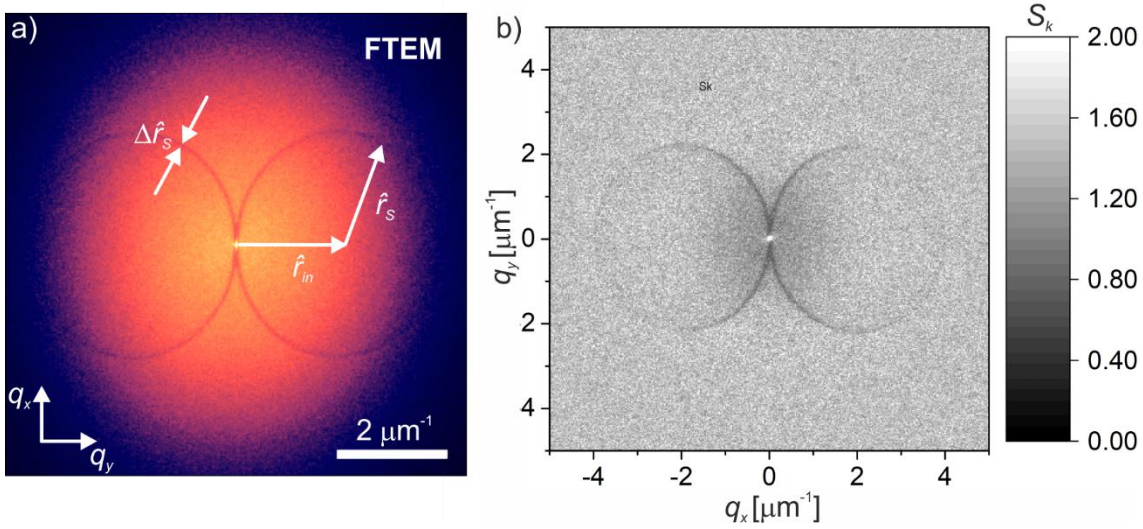

Figure 53: Structure rings representing the engineered sharp features inside the reciprocal space with respect to the nanoparticles and lattice points of the plasmonic metasurface through the calculated FTEM (a) and S_k(b), respectively.

Furthermore, to investigate the features of engineered disorder without the influence of

the particle size and shape, the structure factor S_k is calculated from the corresponding set of SEM micrographs according to the procedure described in Section 3.3.2. Similarly to the FTEM, structure rings are present in the structure factor S_k (Figure 53b), proving engineered features inside the reciprocal space with respect to the lattice points of the plasmonic metasurface.

The next step to examine is how the optical response of the plasmonic metasurface is related to its reciprocal space. The structure rings appear dark in the FTEM (Figure 53a), meaning that the Fourier amplitude $|\mathcal{F}(q_x, q_y)|$ values are reduced along the structure ring compared to the amplitude background of the FTEM. Since the scattering properties of AgNPs are associated with their Fourier amplitude, this observation can be explained in the following manner. The growing AgNPs inherently minimize the probability of converting an incident SPP into a scattered SPP. This assumption can be visualized in reciprocal space as follows. First, dark structure rings or the states of reduced scattering probability formed during AgNP growth are introduced in Figure 54. Next, the scattered SPPs with all possible states are represented by red rings of radius $\hat{r}_w$ and width $\Delta\hat{r}_w$.

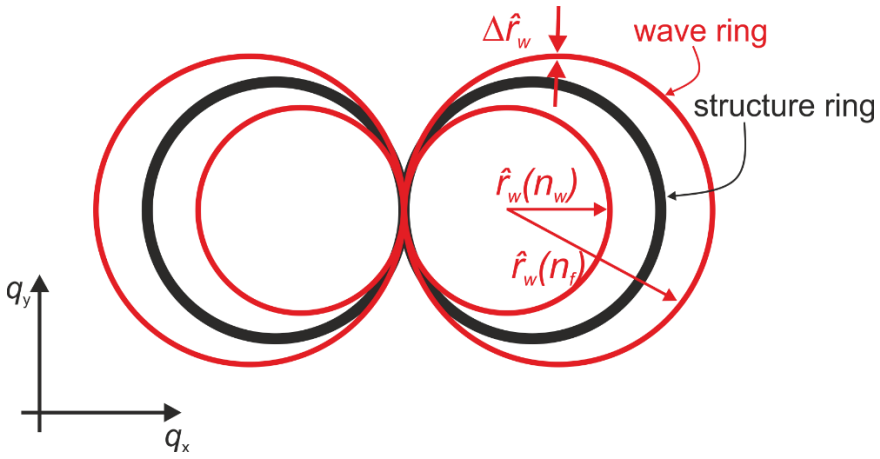

Figure 54: Representation of the optical response of the plasmonic metasurface in reciprocal space.

These rings are referred to as wave rings. The radius of the wave rings in the reciprocal space depends on the refractive index of the environment $\hat{r}_w(n)$. At slight changes of n, the radius of the wave rings can be approximated linearly as:

$$\hat{r}_w(n) \approx \hat{r}_w|_{n=n_{ELD}} + \left.\frac{\partial \hat{r}_w}{\partial n}\right|_{n=n_{ELD}} \Delta n, \tag{1.64}$$

with $\Delta n = n_{ELD} - n$, where n is the refractive index of the environment, n_{ELD} is the refractive index of the ELD solution ($n_{ELD} \approx 1.336$). The dispersion relation of an ideal SPP is used to simplify the calculation of the second term $\left.\frac{\partial \hat{r}_w}{\partial n}\right|_{n=n_{ELD}}$ and neglect the thin PMMA layer. The relative deviation between the simplified and precise values, including the PMMA layer, is below 2%, as verified by numerical simulations. According to the simplified model, the radius of the wave rings is expressed then as:

$$\hat{r}_w(n) = \hat{r}_{spp}(n) = {\lambda_{spp}}^{-1} = {\lambda_0}^{-1} \cdot n_{eff} = {\lambda_0}^{-1} \cdot \left[\frac{n_{Ag}^2 \cdot n^2}{n_{Ag}^2 + n^2}\right]^{1/2}, \tag{1.65}$$

where λ_{spp} is the SPP wavelength, n_{Ag} is the refractive index of the silver film. The corresponding change of $\hat{r}_w$ over n is calculated as:

$$\left.\frac{\partial \hat{r}_w}{\partial n}\right|_{n=n_{ELD}} = \frac{(-1)}{{\lambda_{spp}}^2} \cdot \left.\frac{\partial \lambda_{spp}}{\partial n}\right|_{n=n_{ELD}} = 1.74\ \mu\text{m}^{-1}. \tag{1.66}$$

When the refractive index of the surrounding environment n is changed from n_w to the higher refractive index of n_f, the structure rings remain fixed and unchanged (Figure 54). At the same time, this change in the effective refractive index can be represented by a change in wave ring radius scaled linearly with the effective refractive index of SPPs. The corresponding increase in wave ring radius from $\hat{r}_w(n_w)$ to $\hat{r}_f(n_f)$ is shown schematically in Figure 54. Following this idea, the scattering of incident SPPs into scattered SPPs is decreased when the structure rings (red circles) overlap with the wave rings (black

circles). In terms of reflectance, as less power is lost into scattered SPPs, more light is reflected. Moreover, any environmental changes or mechanical misalignments can detune the rings. In this case, the wave rings do not perfectly overlap with the structure rings, and the probability of scattering incident SPPs into scattered SPPs may increase. As a result, less power is reflected, leading to a decrease in reflectance. Therefore, reflectance from the plasmonic metasurface can be modeled by an overlap of the structure and the wave rings in reciprocal space.

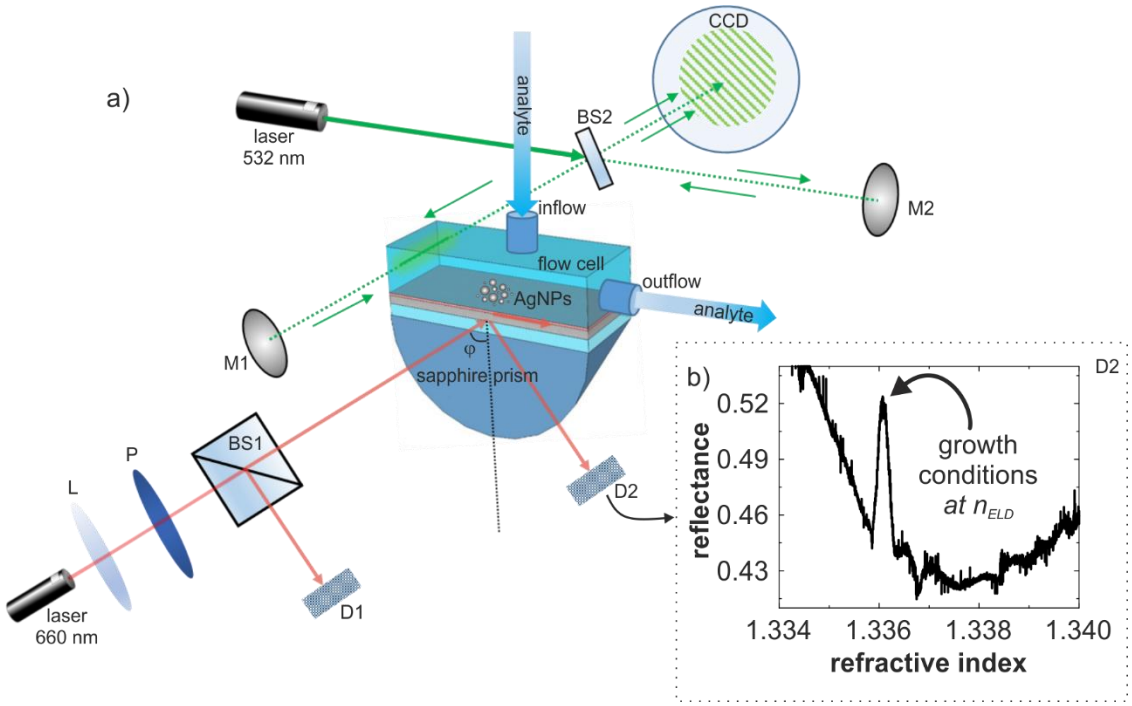

Figure 55: Principle of SPP-induced growth and probing of a plasmonic metasurface of engineered disorder for a sensing application: a) schematic illustration of the ATR setup, which is used for the excitation of SPPs with an additional flow cell equipped with a Michelson interferometer for the measurements of the refractive index change of the test analyte pumped through the flow cell; b) reflectance measured over refractive index change after AgNP deposition, which illustrates the resulting structural feature at the refractive index of ELD solution (growth condition) within the SPP resonance curve.

Based on this chain of thought, the refractive index sensor based on plasmonic metasurface with sharp rings in reciprocal space is developed. Figure 55a shows the experimental setup used for the deposition and characterization of the refractive index sensor. It consists of an ATR setup, a Michelson interferometer, and a flow cell with inflow and outflow for the analyte exchange. First, the flow cell is filled with water ($n_w = 1.333$). Then, the refractive index of the analyte is continuously changed by adding ethanol solution ($n_e = 1.364$) drop by drop to the water via an external reservoir connected to the flow cell (Figure 55a). In this way, the refractive index of solution up to $n_f = 1.340$ can be reached. Before the solution is pumped into the flow cell, it is thoroughly mixed by stirring to avoid inhomogeneity of the analyte, which strongly impacts the interferogram recorded on CCD. In this way, the swept range of the refractive indexes includes the dielectric properties of the ELD solution covering the growth conditions. During the analyte exchange, the ATR setup is unchanged and stays in the same configuration as during the deposition. The ATR setup is additionally equipped with a beam splitter (BS1) and a photodiode (D1) to reference measured signals on a photodiode (D2). The refractive index change inside the flow cell is constantly monitored using a Michelson interferometer (Section 3.2.3) through the change of the optical path in one of its arms, which goes through the flow cell (Figure 55a). The measured reflectance with D2 is shown in Figure 55b. In the beginning, when the refractive index is far from the growth condition ($n < n_{ELD}$), the background signal is governed by attenuated total reflection characteristic. Remarkably, at the refractive index corresponding to the environment during nanoparticle growth ($n = n_{ELD}$), the reflectance exhibits a sharp peak. The measured values of reflectance increase from approximately 44% to 52%. According to the data obtained by the Michelson interferometer, the full FWHM of this peak is around

$\Delta n_0 \approx 3 \cdot 10^{-4}$, which is about two orders of magnitude narrower than the theoretical FWHM of the SPP resonance. When the refractive index is further increased ($n > n_{ELD}$), the reflectance is again followed by a background signal defined by attenuated total reflection characteristic reaching the minimum at $n = 1.3381$ and further increasing afterward (Figure 55b).

4.3.2 Sensor Performance

In the next step, the sensing performance of the plasmonic metasurface is evaluated by calculating the discrete Figure of Merit* (FoM*), based on the measured reflectance (Figure 55b). The FoM* is defined as[89,141,142]

$$\mathrm{FoM}^* = \frac{1}{I}\left|\frac{\partial I}{\partial n_a}\right|, \tag{1.67}$$

where I is the measured intensity of the reflected laser beam at a fixed wavelength λ_0, n_a is the refractive index of the analyte corresponding to the dielectric environment of the grown plasmonic metasurface, and $\frac{\partial I}{\partial n_a}$ is the change of the measured intensity to an analyte refractive index change.[143] In Figure 56, the sensing performance in terms of FoM* is shown with respect to the refractive index of the analyte close to the observed reflectance peak.

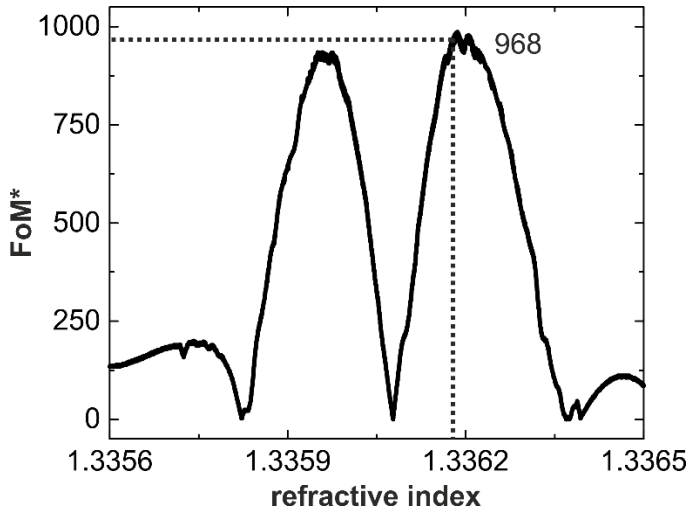

Figure 56: The FoM* of plasmonic metasurface versus the refractive index of an analyte.

The maximum value of FoM* is found to be 968. The plasmonic metasurface with such a high value of FoM* is found to have superior sensing performance compared to state of the art plasmonic sensors fabricated by cost- and labor-intensive, top-down fabrication methods listed in the following reports.[142,144–151]

4.3.3 Spatial Characteristics of Light and Plasmonic Metasurface in Real and Reciprocal Space

To evaluate the suggested model of the plasmonic metasurface reflectance based on an overlap between structure and wave rings, the overlap function (U) defined in Section 3.3.5 is used. As defined, U is 1 for perfect overlap between the rings and 0 when no overlap occurs. Following the procedure of Section 3.3.5, the widths of the structure and the wave rings as input parameters must be estimated. The width of the wave rings ($\Delta\hat{r}_w$) depends on laser beam divergence. In particular, considering the experimental parameters for the SPP excitation: the laser wavelength $\lambda_o = 660$ nm, the incident angle $\varphi_0 = 54°$ and the refractive index of the sapphire prism $n_{prism} = 1.7647$, the reciprocal

width of the laser beam and thus the width of the wave rings $\Delta\hat{r}_w$ in the reciprocal space is calculated from the change in lateral momentum k_x of the incident laser radiation:

$$\hat{r}_{in} = \frac{k_x}{2\pi} = \frac{1}{\lambda_o} n_{prism}\, sin(\varphi) \;\Rightarrow\; \frac{\partial \hat{r}_{in}}{\partial \varphi} = \frac{1}{\lambda_o} n_{prism}\, cos(\varphi)$$

$$\Rightarrow \Delta\hat{r}_w = 2\frac{\partial \hat{r}_{in}}{\partial \varphi}\Delta\gamma = 2\frac{1}{\lambda_o} n_{prism}\, cos(\varphi)\Delta\gamma \tag{1.68}$$

Substituting parameters for SPP excitation and the experimentally measured value of laser divergence $\Delta\gamma$ (Section 3.2.4) into the formula (1.68), the FWHM of the wave ring is calculated $\Delta\hat{r}_w \approx 1.72 \cdot 10^{-4}$ µm^{-1}.

Next, the structure ring width is determined. The actual width of the structure rings cannot be directly measured from the FTEMs due to the uncertainty principle, which limits the resolution of features in reciprocal space by the observation window size in real space. The measured structure ring width $\Delta\hat{r}_s$ theoretically scales with $1/d$, whereby d is the edge length of a square-shaped observation window. This is experimentally verified by measuring the FWHM of the structure ring widths for accessible observation windows with SEM between 92×92 µm² and 148×148 µm². The lower observation windows are obtained by cutting the SEM micrograph with an area of 148×148 µm² into smaller micrographs. The corresponding measured structure ring widths $\Delta\hat{r}_s$ versus observation windows are shown in Figure 57.

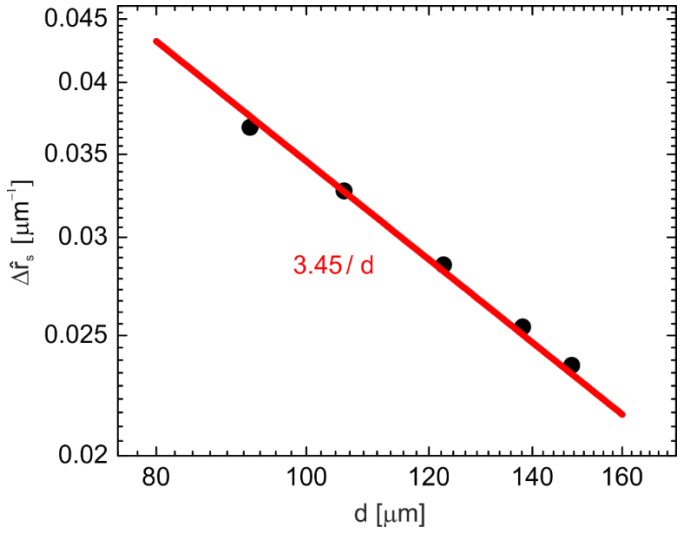

Figure 57. The measured structure ring widths (black points) fitted by a function $\frac{b}{d}$ (red line) with b as a fitting parameter plotted in a double logarithmic scale.

It is observed that the structure ring width gets narrower with increasing length of an observation window. The corresponding function is found to be $\Delta\hat{r}_s = \frac{3.45}{\mathrm{d}}$, shown as a red line in Figure 57. The optical characterization is conducted on much larger areas than the SEM characterization. In particular, the plasmonic metasurfaces appear homogenous over the entire illuminated area A of 33.4 mm². Therefore, the actual structure ring width must be corrected accordingly to describe the optical response of the entire plasmonic metasurface. To determine the corrected width of the structure rings $\Delta\hat{r}_{s,c}$, the length D attributed to the entire illuminated area A is first defined as $D = \sqrt{A}$. The corresponding corrected width of the structure ring is then estimated as $\Delta\hat{r}_{s,c} = \frac{3.45}{\sqrt{A}} \approx 5.97 \cdot 10^{-4}$ μm⁻¹.

4.3.4 Simulation Results of Sensor Response and Comparison to Experiment

The estimated corrected widths for structure ($\Delta\hat{r}_{s,c}$) and the wave ($\Delta\hat{r}_w$) rings are used to calculate the overlap function U according to the procedure described in Section 3.3.5.

The center coordinates (q'_x, q'_y) of the structure ring in reciprocal space are defined as follows:

$$\begin{cases} q'_x = \hat{r}_{spp}\big|_{n=n_{ELD}} + \frac{\Delta\hat{r}_{s,c}}{2} \\ q'_y = 0 \end{cases}. \tag{1.69}$$

with a radius of $\hat{r}_{spp}\big|_{n=n_{ELD}}$ which stays fixed for every value of the refractive index n. At the same time, the wave ring has the center coordinates (q''_x, q''_y) and it is varied with the radius $\hat{r}_{spp}(n)$:

$$\begin{cases} q''_x(n) = \hat{r}_{spp}(n) + \frac{\Delta\hat{r}_w}{2} \\ q''_y = 0 \end{cases}. \tag{1.70}$$

The simplification of using only one structure ring and one wave ring is done as both rings are mirror symmetrically in reciprocal space to the q_y-axis. The radius $\hat{r}_{spp}(n)$ of the wave ring is continuously increased with a step size of $2 \cdot 10^{-5}$. In this way, the wave ring probes the structure ring, as shown in Figure 54. At every refractive index n from $n_w = 1.333$ to $n_f = 1.339$, the overlap function U between the wave and the structure ring is calculated. The red curve in Figure 58b (right) shows the calculated values of $U(n)$ as a function of the refractive index. $U(n)$ is maximized at the refractive index n_{ELD}, corresponding to the refractive index of the ELD solution. The resulting peak has an FWHM of $\Delta n_s \approx 2.9 \cdot 10^{-4}$. It is important to note that the overlap function U defines the optical response depending on the widths of the structure and wave rings. At the same time, these are both controlled by the laser's divergence. Therefore, it is concluded that the performance of the sensor only depends on the laser's divergence, meaning intuitively that a more parallel laser beam yields a sensor of higher performance at a constant deposition area.

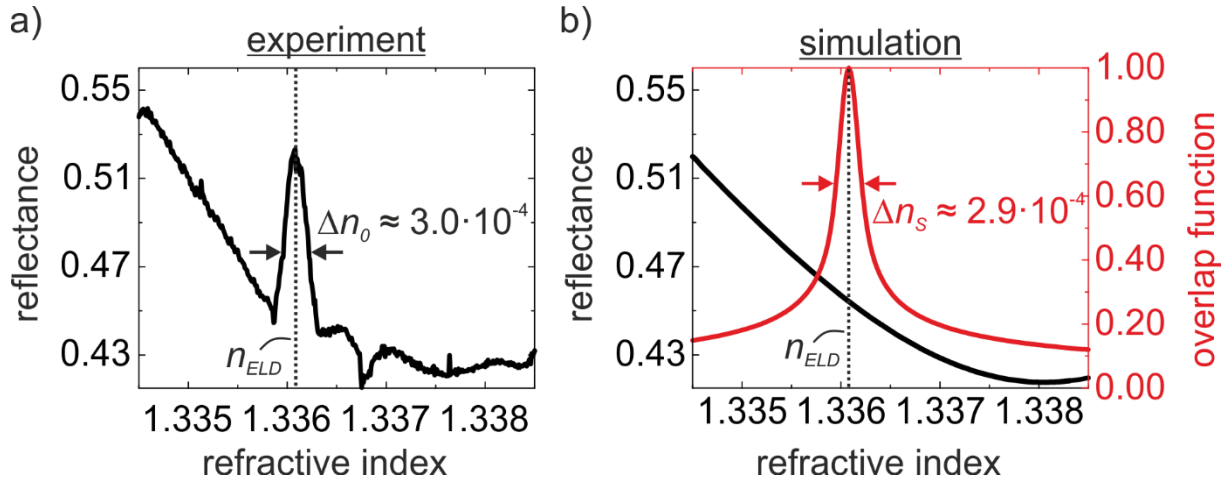

Figure 58: Comparison of simulation and experiment: a) measurement of the reflectance dependent on the refractive index close to the growth conditions (n_{ELD}); b) the overlap function (red curve) with a distinct peak at the refractive index corresponding to the growth conditions (n_{ELD}) and the fitted SPP resonance (black curve).

The measured values of reflectance in Figure 58a agree with the built model. The reflectance away from the growth conditions (n_{ELD}) is governed mainly by a background of an attenuated total reflection characteristic, shown in Figure 58b (black curve). To model it after AgNP deposition, the additional losses caused by the AgNPs are modeled by considering a lossy effective layer with a thickness of 200 nm on top of the silver film (see Section 3.3.5). The refractive index of the effective layer is $n_{layer} = n_{real} + in_{img}$. Figure 59a depicts the impact of the imaginary part of the refractive index n_{img} on the width of the SPP resonance at the fitted value of $n_{real} = 1.3381$.

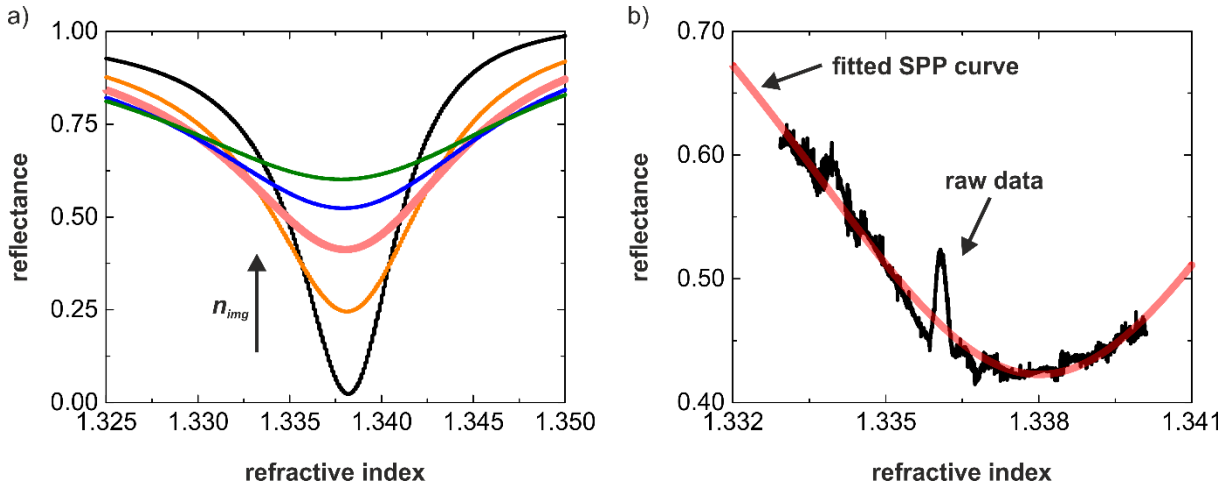

Figure 59: SPP resonance simulation results: a) reflectance at different values of the imaginary part n_{img} of the effective layer; b) fit to the experimental data.

The fit of the simulated attenuated total reflection characteristic to the experimental data (Figure 59b) yielded a value of the refractive index $n_{eff,layer} = 1.3381 + i0.0051$ for the effective layer, whereby positive imaginary values correspond to the loss in the effective layer.

4.3.5 Alignment Tolerance and Spectral Sensitivity of the Fabricated Sensor

In the current section, the alignment tolerance and spectral sensitivity of the built sensor is evaluated. First, the described procedure of using the overlap function U is used to evaluate the impact of mechanical misalignments of probing light on sensor response. The experiments demonstrate that even slight mechanical misalignments after deposition cause the plasmonic metasurface to lose its sensing capability. To analyze the tolerance to mechanical misalignments, the overlap function U of the structure and the wave rings is calculated with respect to changes in both the azimuthal (θ) and polar (φ) angles (Figure 60).

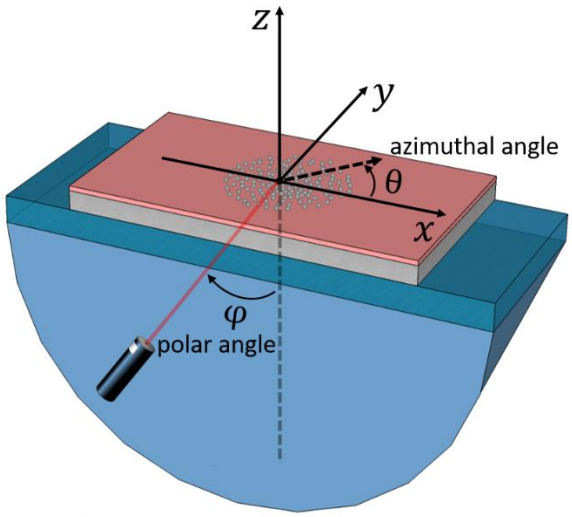

Figure 60: Simulation geometry highlighting azimuth (θ) and polar (φ) angles.

Similar to the procedure above, the center coordinates of the structure and the wave rings are defined first. By changing the azimuthal angle θ (Figure 61a), the center coordinates (q_x', q_y') of the structure ring shift in the reciprocal space to:

$$\begin{cases} q_x'(\theta) = \left[\hat{r}_{spp}\big|_{n=n_{ELD}} + \frac{\Delta\hat{r}_{s,c}}{2}\right] \cdot cos(\theta) \\ q_y'(\theta) = \left[\hat{r}_{spp}\big|_{n=n_{ELD}} + \frac{\Delta\hat{r}_{s,c}}{2}\right] \cdot sin(\theta) \end{cases}. \tag{1.71}$$

The overlap between the wave and the structure ring is calculated by changing the refractive index from $n_w = 1.333$ to $n_f = 1.339$ with a step size of $5 \cdot 10^{-5}$ at every azimuthal angle $\Delta\theta$ from 0.045° to 0.045° with a step size of 0.003. Figure 61c shows a tolerance map of the overlap function U of structure and wave rings to azimuthal angle misalignment. A similar procedure is conducted for the change in polar angle $\Delta\varphi$ (Figure 61b), representing the deviation from the incident angle φ_o. In this case, the structure ring remains unchanged, and only the wave ring is shifted along the q_x-axis to the center coordinates (q_x'', q_y''), defined as:

$$\begin{cases} q_x''(\varphi) = \frac{n_{prism}}{\lambda_o} \cdot \sin(\varphi_o + \Delta\varphi) + \frac{\Delta\hat{r}_w}{2} \\ q_y''(\varphi) = 0 \end{cases}, \tag{1.72}$$

where $\Delta\hat{r}_w = 2\frac{n_{prism}}{\lambda_o} cos(\varphi_o + \Delta\varphi)\Delta\gamma$. Here $\Delta\gamma$ is the beam divergence measured experimentally, see Section 3.2.4. As before, the overlap function U is calculated for a sweep of $\Delta\varphi$ from -0.045° to 0.045° with a step size of 0.003° in a similar refractive index interval from $n_w = 1.333$ to $n_f = 1.339$ with a step size of $5 \cdot 10^{-5}$.

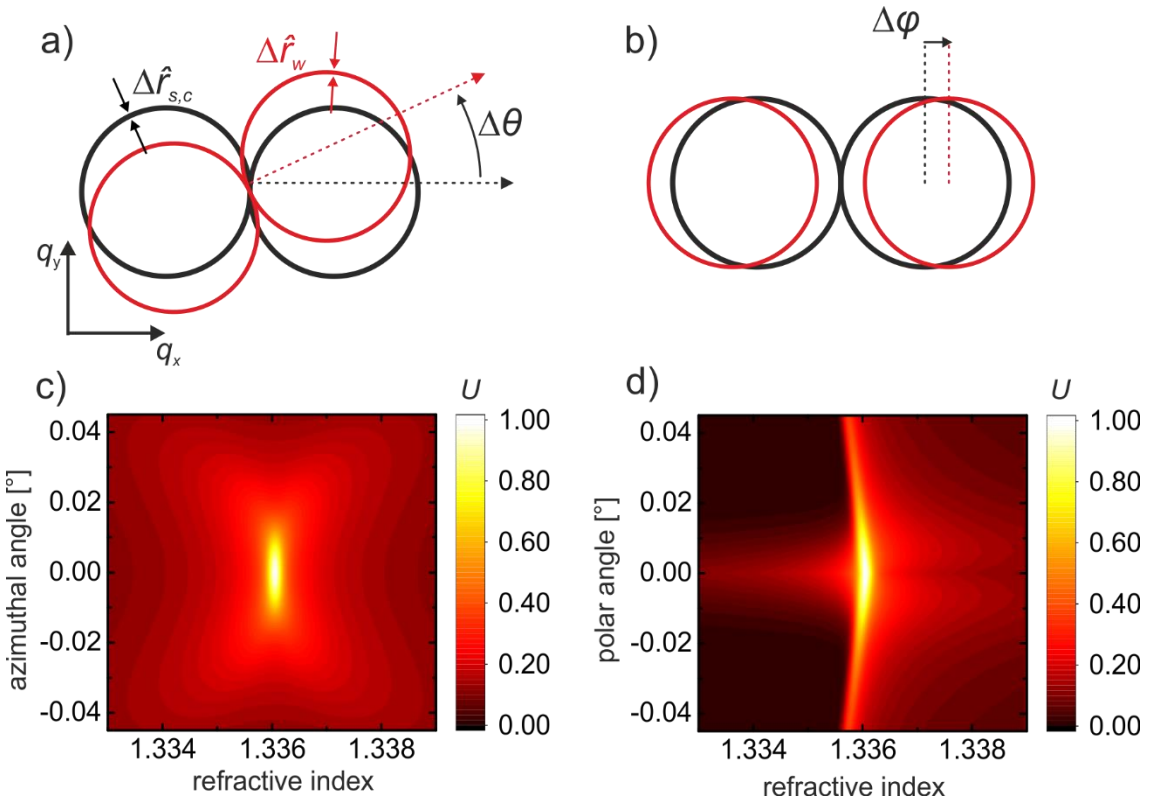

Figure 61: The principle of deriving the overlap function with respect to mechanical misalignments in azimuthal (a) and polar (b) angles with the corresponding simulated tolerance map indicating an impact on the overlap function of the structure and the wave rings towards changes in the azimuthal angle Δφ (c) and changes in the polar angle Δθ (d).

The corresponding tolerance map U is shown in Figure 61d. The simulations show that the overlap function is extremely sensitive to mechanical misalignments of azimuthal and polar angles. The maximum overlap drops down by approximately 50% for the azimuthal and polar angle misalignment of $\Delta\theta \approx 0.01°$ and $\Delta\varphi \approx 0.02°$, respectively. Low tolerance for mechanical misalignments highlights the benefits of instantaneous alignment of plasmonic metasurface during growth with respect to a probing light source without the need for post-process alignment. These properties of the plasmonic metasurface can be applied directly in real application scenarios.

Next, the overlap function is used to evaluate the spectral sensitivity of the fabricated plasmonic metasurface. The wave ring probes the structure ring. In this case, the radius of the wave rings is continuously increased from $\lambda_1 = 559.00$ nm to $\lambda_2 = 661.50$ nm with a step size of 0.03 nm as a function of $\hat{r}_{spp}(\lambda)$. At every wavelength, the overlap function U between the wave and the structure ring is calculated. Figure 62 shows the calculated values of U as a function of the wavelength.

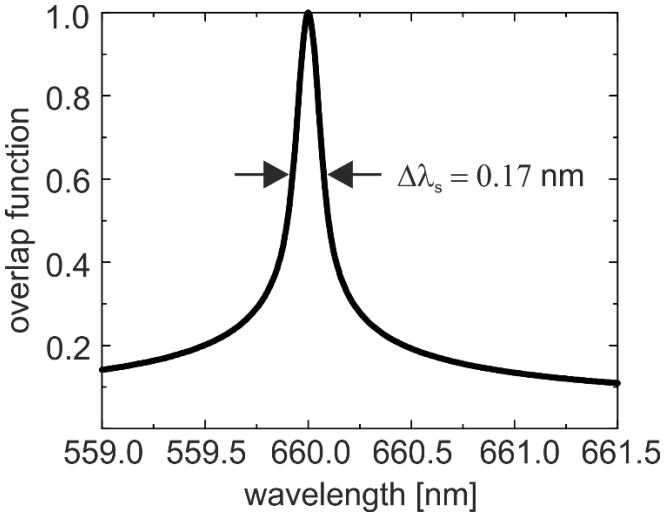

Figure 62: Spectral sensitivity of the fabricated plasmonic metasurface represented by the overlap function with respect to the incident wavelength.

The resulting peak has an FWHM of $\Delta\lambda_s \approx 0.17$ nm. It is important to note that the experimental characterization of spectral sensitivity using a broadband light source is hard to implement as it requires a sampling light source to be identical to the light source applied during sample preparation in terms of coherence and radiance. First, a coherent phase should be maintained over the entire plasmonic metasurface in the millimeters range, which is fulfilled by using the laser source with a length of approximately 30 m. As pointed out above, the sensor performance is proportional to its length. Using a broadband light source with a typical coherence length of about 10 μm to deposit nanoparticles is possible, however, it would lead to a loss of sensor sensitivity. Secondly, investigating the sensor sensitivity in the range of 0.01° requires applying a parallel beam that is not achievable with most broad-band light sources. In addition to the incidence angle (momentum) of both light sources (deposition and probing), their energy needs to match. Deviation by 0.1 nm under maintenance of the coherence and radiance would also lead to a loss of sensor sensitivity.

4.4 Hybrid Optical Structures Based on Spatial Ordering Plasmonic Metasurfaces

The light-controlled alignment of nanoparticles during growth occurs at hot spots of the substrate surface within the area, exposed to the laser beam. The hot spots are defined during the growth process (Section 2.3), resulting in a plasmonic metasurface of engineered disorder. No spatial order is observed in such experiments. In this section, the growth method is modified by introducing electromagnetic boundaries during nanoparticle growth.

First, a resonant mode of a thin film resonator induces nanoparticle growth on spatially varied hot spots, leading to the formation of spatial order in the distribution of the nanoparticles. In particular, the grown nanoparticles form periodic plasmonic gratings with a morphology controlled by the mode of a thin film resonator. In such a way, thin film resonators and AgNPs form a hybrid optical structure. It is shown that the near and far field response of such a hybrid optical structure can be significantly enhanced and modified due to the maximized interaction between the dielectric mode and grown AgNPs, which will be discussed in Section 4.4.1. Here, it is essential to note that the observed differences in interaction between AgNPs and the corresponding modes, such as SPP and dielectric modes, might arise from several factors. Firstly, SPPs exhibit highly localized fields confined to the metal-dielectric interface, resulting in a minimized interaction with plasmonic nanoparticles due to limited spatial overlap. Secondly, the propagation characteristics of SPPs strongly depend on the environment and nanoparticle morphology. During specific stages of nanoparticle growth, it can lead to phase mismatches that strongly reduce interaction[152,153]. In contrast, dielectric modes have more extended field distributions within the dielectric material, promoting a

stronger interaction with AgNPs positioned in proximity[154].

Second, the spatial order of hot spots can be ensured by nanoparticles during their growth, allowing the formation of self-organized periodic plasmonic nanostructures. The self-organized growth of AgNPs is demonstrated experimentally using an asymmetric dielectric waveguide, as described in Section 4.4.2.

4.4.1 Hybrid Optical Structures: Simulation Results and Experimental Realization

The increasing interest in using hybrid optical structures is caused by two factors: high localization of light and low loss propagation. In particular, dielectric-based optics generally have long-range propagation lengths, yielding high-quality resonators [155,156]. On the other hand, plasmonic nanoparticles show strong interaction with light, enabling the confinement of light at the nanoscale. Due to the strong absorption of plasmonic nanoparticles, especially in the visible spectrum, it is possible to explore this localization effect in optoelectronic devices such as optical sensors, solar cells, or photocatalytic cells. To minimize losses, it is possible to use hybrid optical structures where the light can first be focused with low-loss dielectric-based optics and the plasmonic nanoparticles are placed only in that focus afterward. Figure 63a illustrates schematically the principle of such a hybrid optical structure, where plasmonic nanoparticles are placed on well-defined hot spots of the dielectric resonator.

The following numerical simulations are conducted with CST Studio Suite (Section 3.3.4) to show the benefits of nanoparticle positioning into such hot spots. First, 20 nm AgNPs are placed on a flat dielectric substrate and directly illuminated from the bottom side with a plane wave. The cross-section of the electric field distribution in Figure 63b demonstrates optical confinement and field enhancement of the incident light by

nanoparticles. The corresponding absolute values of the electric field strength on the dielectric surface are plotted in Figure 63f (red curve). The light enhancement effect can be further maximized by integrating the AgNPs on top of a dielectric resonator. Here, a dielectric resonator based on the Bragg reflector is used (Section 3.3.3) to excite the standing wave inside (Figure 63c). The corresponding cut of electric field strength along the resonator surface is shown in Figure 63f (black curve). Next, the AgNPs are placed at the spots where the evanescent tails of the standing wave have maximum electric field strength (Figure 63d). In this case, the electric field is significantly enhanced (Figure 63f, blue line). By slightly misaligning AgNPs from the spots of enhanced interaction (Figure 63e), the field strength becomes even lower than for the AgNPs on the dielectric substrate (Figure 63f, green line). On the one hand, these results of numerical simulations highlight the importance of plasmonic nanoparticles being aligned with respect to the dielectric resonator. On the other hand, these results also emphasize the technological challenge related to the cost-effective fabrication of such hybrid optical structures. This technological challenge is addressed in this section and solved by applying the light-controlled growth method. In particular, the growth of AgNPs is induced at the well-controlled spots of maximum intensity generated by the mode of a thin film resonator, schematically illustrated in Figure 64a.

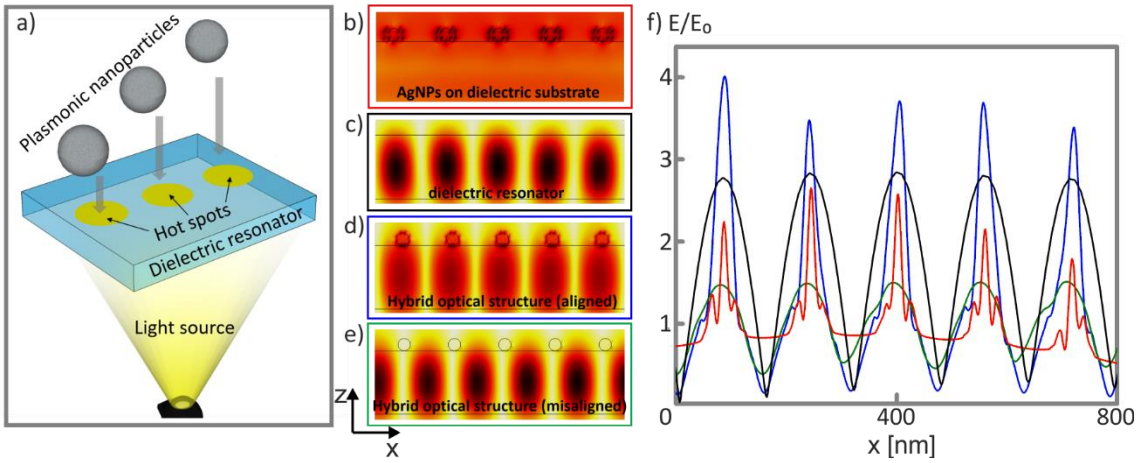

Figure 63: Combination of the AgNPs and dielectric resonators into a hybrid optical structure: a) schematic illustration of the challenge related to hybrid optical structures in the positioning of plasmonic nanoparticles at the hot spots of the dielectric resonator; b) 20 nm AgNPs directly illuminated on a dielectric substrate; c) the coupled mode of the dielectric resonator; d) 20 nm AgNPs placed on dielectric resonator at the places of maximum evanescent field strength; e) 20 nm AgNPs placed on the dielectric resonator and shifted to the positions of minimum evanescent field strength; f) normalized electric field strength on the surface of the dielectric substrate with AgNPs on top (red curve), dielectric resonator without AgNPs (black curve), dielectric resonator with aligned (blue curve) and misaligned (green curve) AgNPs.

A thin film resonator produced by spin-coating and transfer printing (Section 3.1.2) is chosen here to demonstrate the general use of the suggested approach. First, the optical properties of the fabricated thin film resonator are studied numerically with CST Studio Suite (Section 3.3.3). When such a thin film resonator is illuminated with a plane wave in TM polarization from the bottom side of the glass, plasmonic SPP modes can be excited, propagating on both interfaces of the silver film from the gaps. By varying the period of

the gaps of the thin film resonator, interference of SPPs is introduced.

On the other hand, at TE polarization, TE dielectric modes are excited at the gaps and coupled into the polymer film. This way, the presented structure of the thin film resonator supports both SPP and dielectric modes. This section focuses on the resonant excitation of TE dielectric modes in a polymer film. Simulation results show that by illuminating the thin film resonator with a TE-polarized plane wave at the wavelength of 405 nm, around 12 - 14% of the light is transmitted, depending on the polymer film thickness (Figure 64b). There is a sharp drop in transmission down to 6% at a polymer film thickness of around 205 nm. At this thickness, incident light is coupled into TE modes and guided inside the polymer film, forming a mode resonance. The resonator cavity formed between two gaps is shown in Figure 64a. A slight change in the thickness of the polymer film leads to a loss of resonance. The resonator TE mode has pronounced tails of evanescent waves decaying over 130 nm into the water-based environment in z-direction (Figure 64c). The electric field strength in the evanescent tail in a water-based environment is three times higher compared to the incident plane wave. This evanescent wave serves as a driver of the nucleus formation and further plasmon-mediated growth of AgNPs from the ELD solution on the surface of the polymer film. As can be seen, the evanescent wave amplitude varies harmonically with the distance from the gap in the ±x-direction, which can be viewed from the surface side of the thin film resonator in Figure 64d.

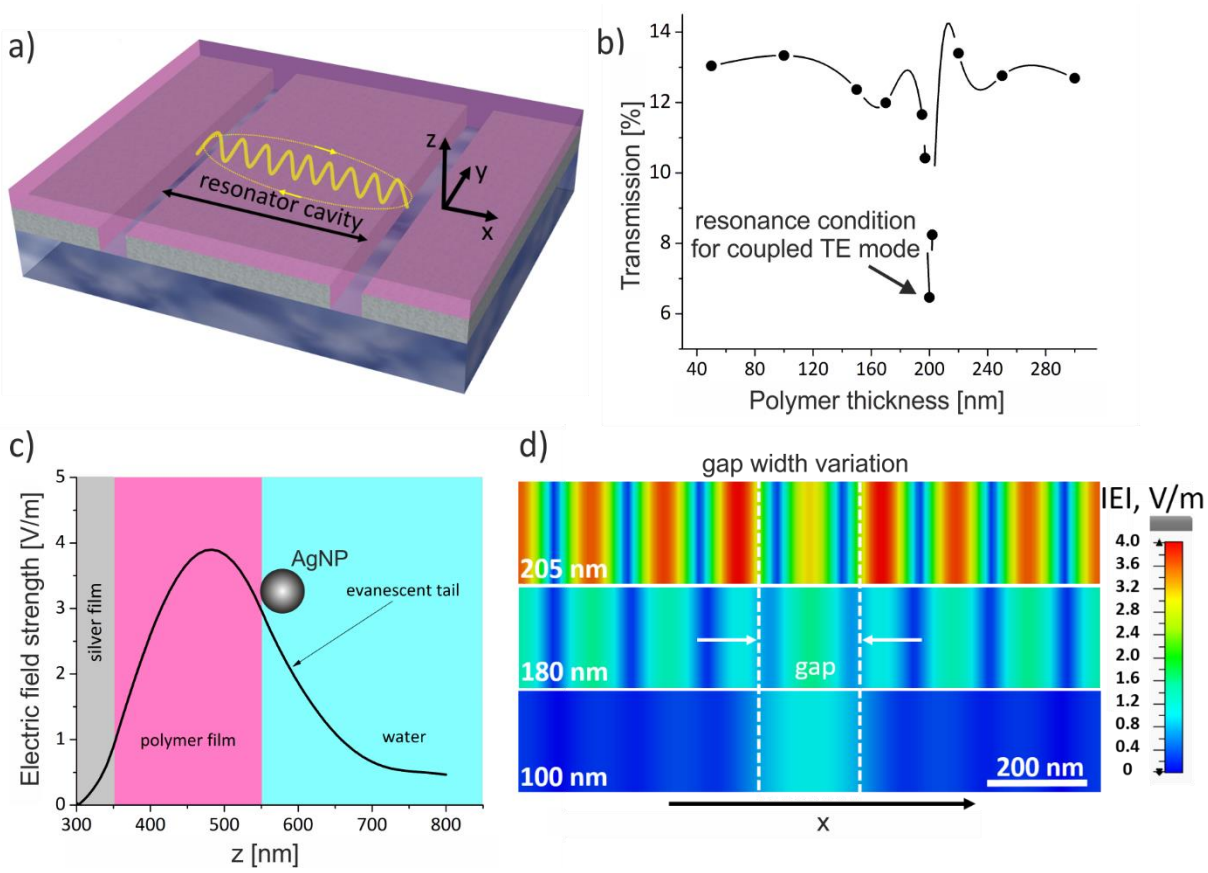

Figure 64: Results of the numerical simulation of a thin film resonator: a) schematic illustration of the resonator cavity in the polymer film; b) transmittance of TE-polarized light through the thin film resonator at different polymer film thickness; c) evanescent wave of the resonator mode as a driving mechanism for AgNP growth on a polymer surface; d) 2D cut of the absolute value of the electric field strength distribution on the polymer film surface at different thicknesses of 100, 180, and 205; the white dashed line indicates the border of the gap of silver grating.

The simulations show that the found resonance is also very sensitive to variations by a few percent in the gap width. In particular, the electric field strength of the evanescent wave on the polymer surface is compared for three thicknesses: 100, 180, and 205 nm.

The field distribution with maximum field strength has a period of 145 nm, corresponding to the wavelength of the film mode of 290 nm. This value fits the wavelength of the wave propagating in the polymer film between the silver film and water environment with an effective refractive index of $n_{eff} = 1.39$, calculated using the transfer matrix method.

Next, the experimental realization of a hybrid optical structure is performed as follows. The ELD solution is cast on the surface of the 180 nm polystyrene film of the thin film resonator and is illuminated from beneath by a CW laser with a wavelength of 405 nm in TE polarization (Figure 65a) through the glass, at a perpendicular angle to the glass surface. Growth occurs at hot spots on the polystyrene film surface where the evanescent wave of the resonator mode has maximum electric field strength values. The obtained distribution of AgNPs after 1 min of illumination is shown in the SEM micrograph (Figure 65b).

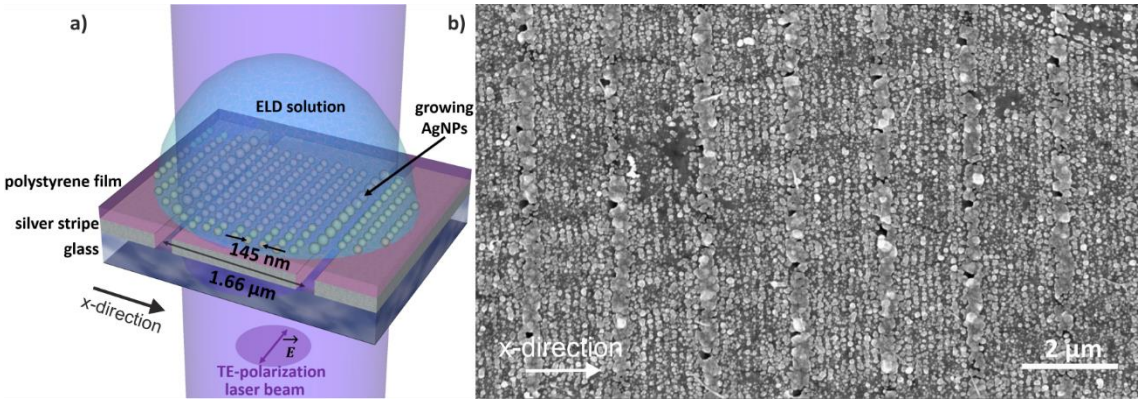

Figure 65: Experimental realization of a hybrid optical structure: a) schematic illustration of AgNP growth on top of the polystyrene film of the thin film resonator; b) SEM micrograph of the AgNPs on polystyrene.

Two types of lines are distinguishable in the SEM micrograph: thick lines with a period of 1.66 µm and thin lines in between with a period of around 145 nm. The SEM micrograph

is analyzed using FFT to determine the line periods. The thick lines formed by coalescing AgNPs have a width fitting the width of the gap of 200 nm. At the same time, the thin lines consist of closely spaced AgNPs with an average diameter of around 40 nm. The period of thin lines corresponds to half the simulated wavelength of an evanescent wave on the surface of polystyrene film. This value corresponds to the resolution limit found in light-induced nanopatterning defined as: $\lambda_0/(2 \times n_{eff})$. The number of thin lines between gaps matches the simulated number of maxima shown in Figure 64d.

The partial removal of the nanoparticles from the places between the gaps is observed after 10 min of treatment. After the next 5 min, the thin lines are almost entirely removed, while the thick lines above the gaps remain unchanged. The morphology development of the plasmonic metasurface is shown in the SEM micrographs in Figures 66a - c. These experiments illustrate that light exposure locally increases the adhesion of AgNPs on the substrate through plasmon-mediated photooxidation, and adhesion increases with the intensity of the light confined at a hot spot. These observations agree with other reports[157,158].

According to the simulation result (Figure 64d), decreasing the polymer film thickness from 180 to 100 nm leads to suppression of the TE mode of the resonator. There is a certain cut-off thickness at which the light cannot be guided. This is confirmed by the experiment at the polystyrene thickness of 100 nm, where the AgNPs are found only above the gaps (Figure 67). No growth between the gaps is observed, confirming that the dielectric mode of the resonator drives AgNP growth. The nanoparticle lines are observed on the area of 2 mm, restricted by the beam size.

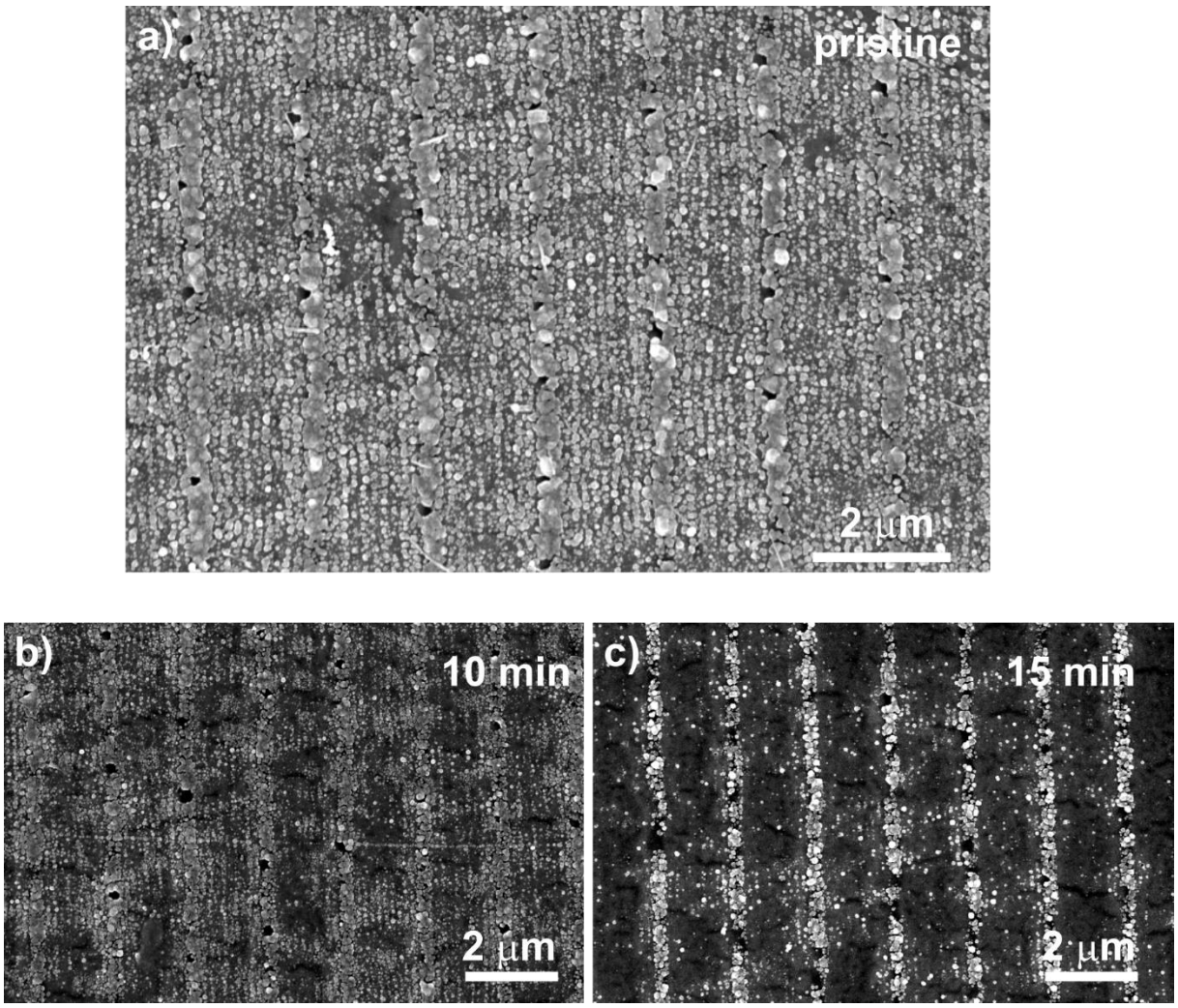

Figure 66: SEM micrographs of AgNPs on a polystyrene surface after 0 min (a), 10 min (b), and 15 min (c) in an ultrasonic bath at room temperature, compared with pristine morphology.

The width of the formed lines is slightly higher than 200 nm due to the light diffraction at the gaps. A slight coalescence of AgNPs is also observed, which can be further controlled by deposition time and the concentration of silver ions in the solution[158]. The diameter of nanoparticles stays between 50 to 60 nm. Another observation is the non-spherical shape of nanoparticles.

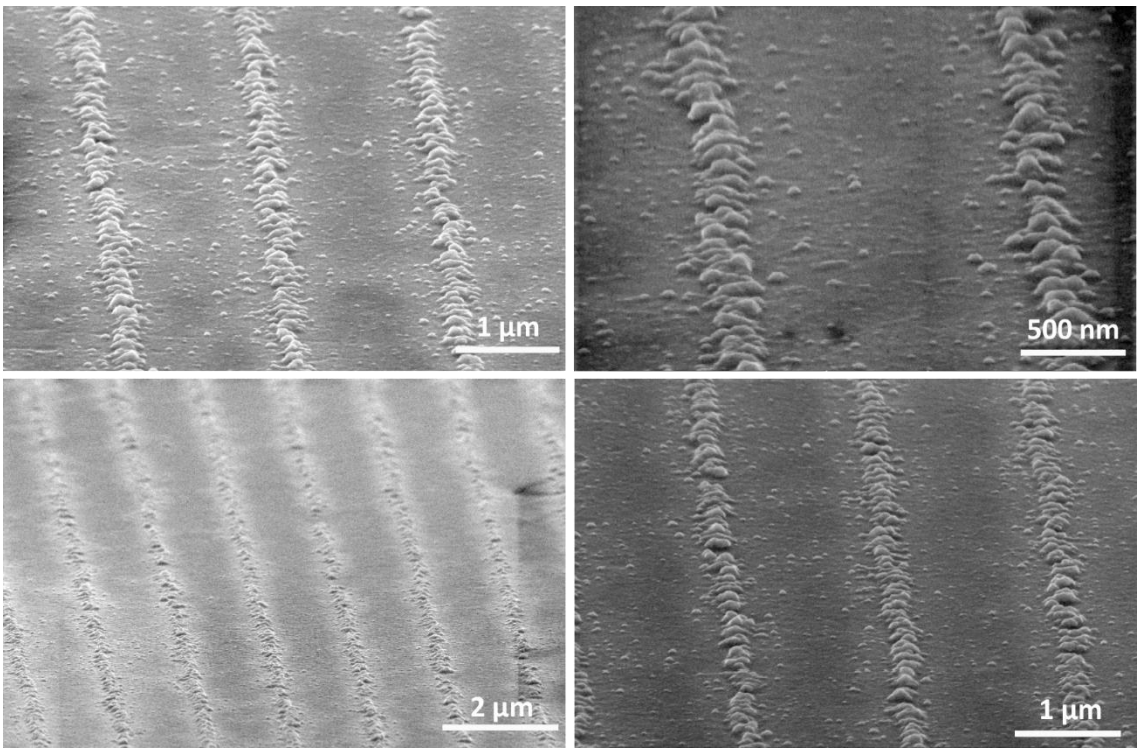

Figure 67: SEM of AgNPs growing above the gaps on 100 nm polystyrene film.

As is generally known, the surface tension impacts the shape of the formed nanoparticles. The more hydrophobic the surface, the more the shape becomes spherical. The non-spherical morphology of nanoparticles formed on the hydrophobic polystyrene film, which has a surface energy of 52 mN/m, can be attributed to plasmon-mediated growth mechanisms.

Next, the near and far-field optical properties of the experimentally realized hybrid optical structure consisting of the thin film resonator with AgNPs on top are studied using numerical simulations (Section 3.3.3). Two opposite scenarios are considered here: the AgNPs are placed first at maximum and then at minimum electric field strength of the evanescent wave. AgNPs of radius 20 and 40 nm are considered. Figures 68b and c show the strength of the evanescent electric field on the surface of the polymer for three

different cases: pure thin film resonator without AgNPs (black curves), thin film resonator with AgNPs at minimum strengths of the evanescent wave (green curves), and thin film resonator with AgNPs at maximum strengths of the evanescent wave (blue curves). The strongest interaction is observed for the 40 nm AgNPs placed at a maximum strength of the evanescent electric field, which can be seen in Figure 68b (blue curve). This case is also demonstrated in the 3D cut of the polymer film surface in Figure 68a, illustrating the electric field confinement by AgNPs. The simulated hybrid optical structure with AgNPs at maximum interaction shows efficient confinement of the incoming light for the AgNPs with a radius corresponding to efficient LSP excitation. The resonant scattering and absorption of incoming light are observed in the presence of 40 nm AgNPs in a water environment, as their LSP closely aligns with the utilized 405 nm wavelength. In addition, a slight shift away from the maximum interaction spots leads to a strong reduction in interaction between the modes of the thin film resonator and AgNPs. The mode shape remains almost unchanged when the 40 nm AgNPs are moved to minimum evanescent field strength spots (Figure 68b, green curve). At the same time, 20 nm AgNPs at the places with a minimum strength of the evanescent wave interact weakly with the resonator mode through evanescent tails, leaving the initial strength and mode shape almost unaffected (Figure 68c, green curve). Furthermore, shifting AgNPs to the positions of maximized interaction significantly modifies the far-field scattering directions.

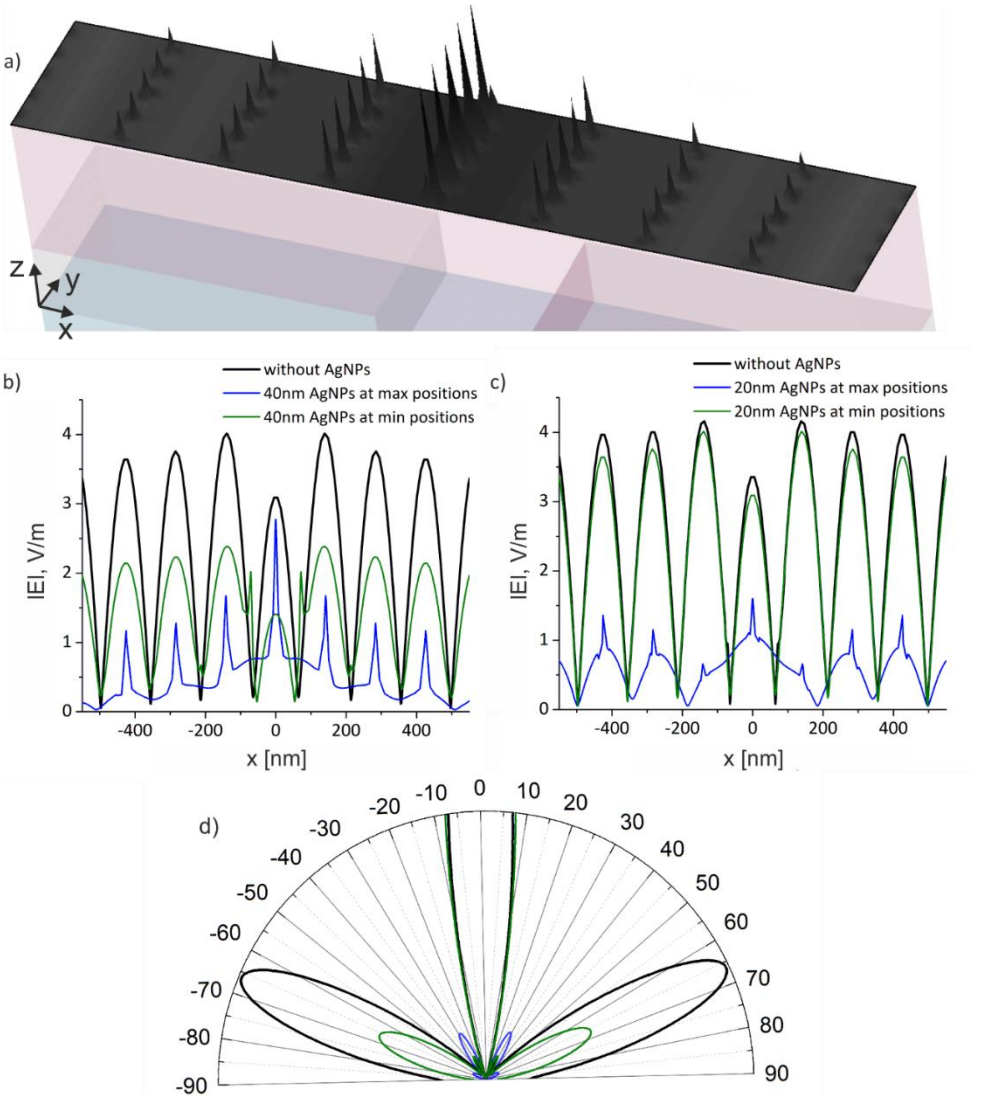

Figure 68: Near- and far-field response of the hybrid optical structure: a) the electric field confinement on the polymer film surface with 40 nm AgNPs placed at a maximum evanescent field strength of TE mode; b) and c) evanescent waves extracted for 40 and 20 nm AgNPs respectively which are placed at maximum (blue curve) and minimum (green curve) positions of the evanescent field strength, and evanescent waves without AgNPs (black line); d) far-field scattering diagram at zero degrees of the azimuth angle of the hybrid optical structure with AgNPs placed at maximum (blue line) and minimum (green line) evanescent field strength, and without AgNPs (black line).

A scattering diagram at an azimuth angle of zero degrees is shown in Figure 68d. The scattering behavior of AgNPs in regions of minimal interaction (green curve) is comparable to that observed in the absence of AgNPs (black line), as they scatter in similar directions. In contrast, by shifting AgNPs to the places where the local field strength is at its maximum, some scattering directions get suppressed at a meridian angle of 65°, while others become sharper and more pronounced at 30° (blue curve).

4.4.2 Grating Formation on a Waveguide Surface and the Impact of Boundaries

There is an alternative way to fabricate a hybrid optical structure without requiring resonators. The self-organized growth of nanoparticles into a periodic plasmonic grating on top of the dielectric waveguide can be implemented without the need for resonant boundary conditions to form a predefined interference pattern before casting the ELD solution. The periodic modulation of the electric field on a waveguide surface can be formed during nanoparticle growth from the ELD solution. In particular, the nanoparticles are grown into a periodic plasmonic grating at the places defined by the interferences between an incident wave and an SPP wave scattered along the waveguide surface. SPPs are excited at surface roughness induced by AgNPs during growth. An important condition here is that both modes having different phase velocities propagate along the waveguide surface in one direction.

The entire process of such self-organized growth into a specially ordered plasmonic grating on top of the dielectric waveguide can be divided into three parts: mode-induced growth of nanoparticles on top of the waveguide surface, excitation of the SPP waves at already grown nanoparticles, interference between SPP and incident waves, and subsequent further growth of nanoparticles in the places of maximum intensity of the

resulting interference pattern. In this way, the period of the formed interference pattern (Λ) or the period of the plasmonic grating formed by AgNPs (Figure 69a) can be expressed mathematically as follows. First, it is assumed that the SPP wave excited at the grown AgNPs has a wave vector k_{spp}, which can be expressed as:

$$k_{spp} = \eta \cdot k_{m,x}, \tag{1.73}$$

where $k_{m,x}$ is the projection of the wave vector of the propagating waveguide mode $\boldsymbol{k}_m$ on the x-axis (Figure 69a), η is a coefficient of proportionality. By assuming that the amplitude of both waves is equal, the resulting electric field can be expressed as a sum:

$$E_{res} = \frac{E_0}{2}\left(\underbrace{e^{ik_{m,x}x}}_{waveguide\ mode} + \underbrace{e^{ik_{spp}x}}_{SPP\ mode}\right) = \frac{E_0}{2}e^{ik_{m,x}x}(1 + e^{ik_{m,x}(\eta-1)x}). \tag{1.74}$$

The resulting intensity of interference of both waves is then:

$$I \sim |E_{res}|^2 \sim (1 + \cos(\underbrace{k_{m,x}(\eta - 1)}_{k_{eff}}\, x)). \tag{1.75}$$

The term $(1 + \cos(k_{m,x}(\eta - 1)x))$ describes the standing wave with the period of Λ linked to $k_{m,x}$ and k_{spp} as:

$$k_{eff} = k_{m,x}(\eta - 1) = \frac{2\pi}{\Lambda} \text{ or } k_{spp} - k_{m,x} = \frac{2\pi}{\Lambda}. \tag{1.76}$$

Taking the expression for the wave vector of the SPP mode k_{spp}, and assuming that the SPP wave propagates at the interface between silver (ε_m) and the dielectric waveguide (ε_{oc}), the following expression from (1.76) can be obtained:

$$\frac{2\pi}{\Lambda} = \frac{2\pi}{\lambda_0}\sqrt{\frac{\varepsilon_m \varepsilon_{oc}}{\varepsilon_m + \varepsilon_{oc}}} - k_{m,x}. \tag{1.77}$$

Here $k_{m,x}$ is expressed as $k_{m,x} = \frac{2\pi}{\lambda_0}\sin(\varphi_m)\, n_m$, where λ_0 is the light wavelength, n_m is an effective refractive index of the mode propagation inside Ormocore, and φ_m is the internal

mode angle of φ_m, which is derived from the mode excitation condition via the period Λ_{gr} of the coupling grating (see Section 2.1.3). In the end, the period of the resulting interference pattern is then calculated as follows:

$$\Lambda = \lambda_0 \left[\sqrt{\frac{\varepsilon_m \varepsilon_{oc}}{\varepsilon_m + \varepsilon_{oc}}} - \sin(\varphi_m)\, n_m \right]^{-1}. \tag{1.78}$$

The self-organized growth of nanoparticles into the periodic plasmonic grating with the period Λ defined by (1.78) is proved experimentally using the OrmoCore waveguide prepared according to the procedure described in Section 3.1.3 and electroless deposition on top of that waveguide. The experimental setup described in Section 3.2.1 is used to excite the corresponding mode and monitor AgNP growth. In detail, the TM-polarized laser beam with a wavelength of $\lambda_0 = 405$ nm is focused at the edge of the OrmoCore grating with a period of $\Lambda_{gr} = 555$ nm. The power density is around 1.5 W/cm^2. The corresponding TM_0 mode is excited at an incident angle of $\varphi_{in} = 58°$ (Figure 69a). This way, the TM_0 mode propagates in OrmoCore of thickness 1600 nm between OrmoClad of thickness 100 nm and air. Once the TM_0 mode is excited, the ELD solution is cast on top of the waveguide (Figure 69b) for nanoparticle deposition. The challenging experimental issue is to make sure that the edge of the ELD drop is perpendicular to $k_{m,x}$. In this case, the wave fronts of the interfering waves are parallel to each other. After 5 min of deposition, the ELD solution is removed from the waveguide surface.

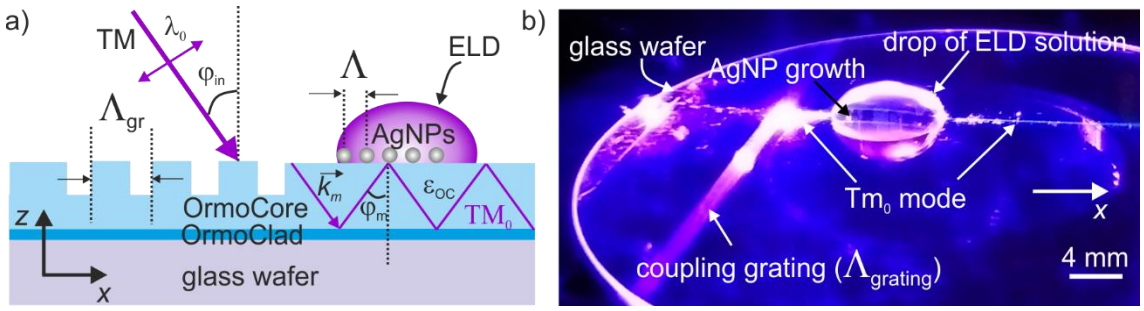

Figure 69: Self-organized growth of AgNPs into periodic plasmonic grating on the surface of the asymmetric dielectric waveguide: a) schematic illustration of the experimental setup: the incident light (λ_0) at the angle of φ_{in} in TM polarization state; coupling grating with a period of Λ_{gr} and corresponding TM_0 mode with the wave vector of $\boldsymbol{k}_m$ and internal propagation angle of φ_m; a drop of ELD solution causing AgNPs to form a periodic plasmonic grating with a period of Λ; b) a photograph of the experiment with a drop of ELD solution placed on the waveguide surface where the TM_0 mode is excited.

The obtained plasmonic metasurface is shown below in the SEM micrograph (Figure 70a) with an underlined area of the ELD drop border (Figure 70b). The corresponding FTEM is shown in Figure 70c. Two features are distinguished: two symmetric dark rings, indicating a formation of engineered disorder in nanoparticle distribution (Section 2.4), and bright Bragg peaks, indicating the formation of spatial order in the form of the periodic plasmonic grating. It is assumed that the engineered disorder occurs at the beginning of the deposition. The manifestation of Bragg peaks occurs after a critical nanoparticle density on the surface, at which excitation of the SPP wave takes place with subsequent interference. Thus, after a certain time of deposition (around 1 - 2 min), the grating formation process dominates, making the Bragg peaks much more pronounced

than the dark ring features (Figure 70c).

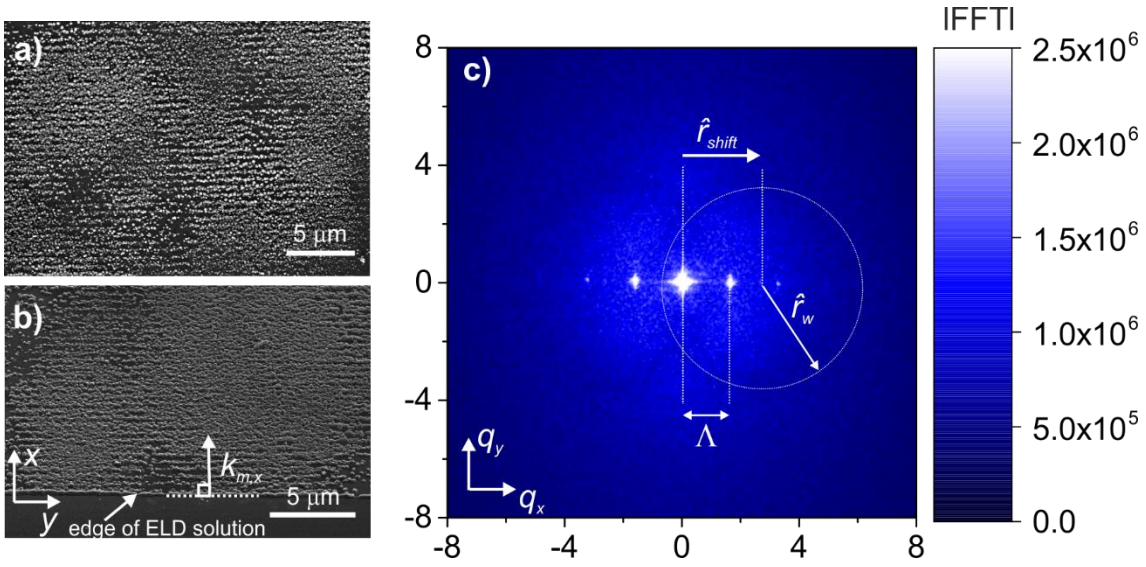

Figure 70: Fabrication of periodic plasmonic grating on the surface of the asymmetric dielectric waveguide: a) the SEM micrograph of the waveguide surface after 5 min of deposition; b) the SEM micrograph indicating the edge of the ELD solution drop; c) the corresponding FTEM with two distinguishable features: dark rings and Bragg peaks.

The shift of the rings ($\hat{r}_{shift}$) from the center coordinate in FTEM corresponds to the projection of the coupled mode wave vector on the x-axis:

$$\hat{r}_{shift} = \frac{k_{m,x}}{2\pi} = \frac{1}{\lambda_0}\sin(\varphi_m)\, n_m. \tag{1.79}$$

By calculating an effective refractive index of the TM_0 mode ($n_m = 1.57$) using the transfer matrix method, the total internal angle of the mode can be extracted ($\varphi_m \approx 66°$). The radius of the ring $\hat{r}_w$ in FTEM is found to be 3.25 μm^{-1}, which fits the material wavelength of $\lambda_w = \frac{\lambda_0}{n_{ELD}} = 305$ nm. At the same time, the period of the formed plasmonic grating calculated using formula (1.78) equals to $\Lambda_0 = 506$ nm, which fits well with the extracted value from FTEM of $\Lambda = 501$ nm.

Conclusion

The thesis presents a novel approach to disorder engineering of plasmonic metasurfaces on a large-scale using light-controlled deposition of nanoparticles from a solution. Through the precise control of experimental growth parameters and properties of illuminating light, this bottom-up method allows the creation of both broad and narrow, tunable features inside the reciprocal space. Having tunable features inside the reciprocal space of a plasmonic metasurface enables the precise control of the optical properties of the metasurfaces.

The thesis showcases three experimental implementations of the method: deposition in darkness, under polarized light illumination, and via surface plasmon polaritons excitation. These implementations are expected to facilitate the straightforward fabrication of plasmonic metasurfaces on significantly larger area scales than those achievable by current top-down techniques.

It was shown that plasmonic metasurface fabricated in darkness possesses broad characteristics inside reciprocal space with features of hyperuniformity, which can be transformed to a stronger form of hyperuniformity to isotropic or anisotropic stealthy hyperuniformity when illuminated by light.

Furthermore, narrow characteristic features in reciprocal space were found by adjusting the growth parameters during the deposition under plasmon polaritons excitation. Following the deposition process, the metasurface exhibits inherent sensitivity to variations in the electromagnetic environment compared to the conditions during its growth. Although high sensitivity to electromagnetic environment changes often implies reduced tolerance for mechanical misalignments, in this case, the metasurface is naturally aligned to the specific wavefronts of a fixed light source employed for the plasmon-

induced growth. This allowed for developing a novel design for refractometry plasmonic sensors with outstanding performance. The first experimental demonstration of such a sensor in this work shows a remarkably high figure of merit. The concept is based on utilizing a sharp resonance curve observed in the reflection signal as a function of the refractive index of the water-based analyte solution. The width of the resonance was found to be around two orders of magnitude narrower than the SPP resonance. Moreover, the resonance is governed by the divergence of the laser, which was used for the fabrication and probing of the reflection signal. A more parallel light source can produce a plasmonic metasurface with even sharper features inside the reciprocal space. This enhances sensing performance further without additional adjustments or complex alignment procedures. With this novel concept, it might be possible to surpass the performance of state-of-the-art plasmonic sensors fabricated with top-down lithographic approaches and to enhance the quality factor of plasmonic sensors significantly.

Further exploring nanoparticle growth under surface plasmon excitation scheme in ultra-thin films allowed us to excite short-range and long-range SPP modes at the same excitation spot during the nanoparticle growth. Applying the same sensing concept will further optimize sensor performance in terms of sensitivity and selectivity in detecting a slight change of analyte in close proximity to the surface.

Additionally, it was shown that this approach facilitates a seamless transition to engineering of ordered plasmonic structures over a large area. The nanoparticles grown directly on a dielectric resonator or waveguide by excited mode were demonstrated to form well-ordered plasmonic chains of nanoparticles. In this way, ordered nanoparticle arrays are aligned to the propagating resonance mode making it worthwhile to fabricate

hybrid optical structures for enhanced interaction between dielectric and plasmonic parts.

The thesis represents a valuable contribution to the fields of plasmonic sensors and disorder engineering. Its findings have the potential to drive advancements in the development of next-generation optoelectronic devices. The presented results open up possibilities for enhanced design flexibility, such as exploiting additional states of light polarization, multiple incident waves, or nonlinear optical effects. Overall, this research lays the groundwork for advancements in optical metasurface fabrication and exploring innovative optical functionalities.

References

[1] C. De Rosa, F. Auriemma, C. Diletto, R. Di Girolamo, A. Malafronte, P. Morvillo, G. Zito, G. Rusciano, G. Pesce, A. Sasso, *Phys. Chem. Chem. Phys.* **2015**, *17*, 8061.

[2] J. H. Park, J. Park, K. R. Lee, Y. K. Park, *Adv. Mater.* **2020**, *32*, 1903457.

[3] S. Torquato, *Phys. Rep.* **2018**, *745*, 1.

[4] S. Yu, C. W. Qiu, Y. Chong, S. Torquato, N. Park, *Nat. Rev. Mater.* **2020**, *6*, 226.

[5] M. Rothammer, C. Zollfrank, K. Busch, G. von Freymann, *Adv. Opt. Mater.* **2021**, *9*, 2100787.

[6] E. Moyroud, T. Wenzel, R. Middleton, P. J. Rudall, H. Banks, A. Reed, G. Mellers, P. Killoran, M. M. Westwood, U. Steiner, S. Vignolini, B. J. Glover, *Nature* **2017**, *550*, 469.

[7] H. Yin, B. Dong, X. Liu, T. Zhan, L. Shi, J. Zi, E. Yablonovitch, *Proc. Natl. Acad. Sci.* **2012**, *109*, 10798.

[8] D. S. Wiersma, *Nat. Photonics* **2013**, *7*, 188.

[9] R. H. Siddique, Y. J. Donie, G. Gomard, S. Yalamanchili, T. Merdzhanova, U. Lemmer, H. Hölscher, *Sci. Adv.* **2017**, *3*, e1700232.

[10] K. Vynck, R. Pacanowski, A. Agreda, A. Dufay, X. Granier, P. Lalanne, *Nat. Mater.* **2022**, *21*, 1035.

[11] O. Leseur, R. Pierrat, R. Carminati, *Optica* **2016**, *3*, 763.

[12] J. Ricouvier, P. Tabeling, P. Yazhgur, *Proc. Natl. Acad. Sci.* **2019**, *116*, 9202.

[13] P. M. Piechulla, B. Fuhrmann, E. Slivina, C. Rockstuhl, R. B. Wehrspohn, A. N. Sprafke, *Adv. Opt. Mater.* **2021**, *9*, 1.

[14] W. Man, M. Florescu, E. P. Williamson, Y. He, S. R. Hashemizad, B. Y. C. Leung, D. R. Liner, S. Torquato, P. M. Chaikin, P. J. Steinhardt, *Proc. Natl. Acad. Sci.*

2013, *110*, 15886.

[15] M. Castro-Lopez, M. Gaio, S. Sellers, G. Gkantzounis, M. Florescu, R. Sapienza, *APL Photonics* **2017**, *2*, 061302.

[16] Z. Fusco, R. Bo, Y. Wang, N. Motta, H. Chen, A. Tricoli, *J. Mater. Chem. C* **2019**, *7*, 6308.

[17] M. C. Van Lare, A. Polman, *ACS Photonics* **2015**, *2*, 822.

[18] H. Zhang, Q. Cheng, H. Chu, O. Christogeorgos, W. Wu, Y. Hao, *Appl. Phys. Lett.* **2021**, *118*, 101601.

[19] N. Tavakoli, R. Spalding, A. Lambertz, P. Koppejan, G. Gkantzounis, C. Wan, R. Röhrich, E. Kontoleta, A. F. Koenderink, R. Sapienza, M. Florescu, E. Alarcon-Llado, *ACS Photonics* **2022**, *9*, 1206.

[20] S. Gorsky, W. A. Britton, Y. Chen, J. Montaner, A. Lenef, M. Raukas, L. Dal Negro, *APL Photonics* **2019**, *4*, 110801.

[21] R. Degl'Innocenti, Y. D. Shah, L. Masini, A. Ronzani, A. Pitanti, Y. Ren, D. S. Jessop, A. Tredicucci, H. E. Beere, D. A. Ritchie, *Sci. Rep.* **2016**, *6*, 19325.

[22] J. Park, K. R. Lee, Y. K. Park, *Nat. Commun.* **2019**, *10*, 1304.

[23] M. Haghtalab, M. Tamagnone, A. Y. Zhu, S. Safavi-Naeini, F. Capasso, *ACS Photonics* **2020**, *7*, 991.

[24] O. U. Uche, F. H. Stillinger, S. Torquato, *Phys. Rev. E - Stat. Physics, Plasmas, Fluids, Relat. Interdiscip. Top.* **2004**, *70*, 9.

[25] E. Chertkov, R. A. Distasio, G. Zhang, R. Car, S. Torquato, *Phys. Rev. B* **2016**, *93*, 064201.

[26] D. Chen, S. Torquato, *Acta Mater.* **2018**, *142*, 152.

[27] M. Pelton, J. Aizpurua, G. Bryant, *Laser Photonics Rev.* **2008**, *2*, 136.

[28] T. J. Merkel, K. P. Herlihy, J. Nunes, R. M. Orgel, J. P. Rolland, J. M. Desimone, *Langmuir* **2010**, *26*, 13086.

[29] J. Henzie, M. H. Lee, T. W. Odom, *Nat. Nanotechnol.* **2007**, *2*, 549.

[30] P. M. Piechulla, L. Muehlenbein, R. B. Wehrspohn, S. Nanz, A. Abass, C. Rockstuhl, A. Sprafke, *Adv. Opt. Mater.* **2018**, *6*, 1.

[31] M. Salvalaglio, M. Bouabdellaoui, M. Bollani, A. Benali, L. Favre, J. B. Claude, J. Wenger, P. De Anna, F. Intonti, A. Voigt, M. Abbarchi, *Phys. Rev. Lett.* **2020**, *125*, 126101.

[32] T. Ma, H. Guerboukha, M. Girard, A. D. Squires, R. A. Lewis, M. Skorobogatiy, *Adv. Opt. Mater.* **2016**, *4*, 2085.

[33] S. A. Maier, *Plasmonics: Fundamentals and Applications*, Springer, **2007**.

[34] Kan Yao and Yongmin Liu, *Nanofabrication Handb.* **2012**, *3*, 437.

[35] K. A. Willets, A. J. Wilson, V. Sundaresan, P. B. Joshi, *Chem. Rev.* **2017**, *117*, 7538.

[36] S. Sun, Q. He, S. Xiao, Q. Xu, X. Li, L. Zhou, *Nat. Mater.* **2012**, *11*, 426.

[37] H. A. Atwater, A. Polman, *Nat. Mater.* **2010**, *9*, 205.

[38] Y. Fang, M. Sun, *Light Sci. Appl.* **2015**, *4*, e294.

[39] T. J. Davis, D. E. Gómez, A. Roberts, *Nanophotonics* **2017**, *6*, 543.

[40] Y. Lee, S. J. Kim, H. Park, B. Lee, *Sensors* **2017**, *17*, 1726.

[41] A. Polywka, A. Vereshchaeva, T. Riedl, P. Görrn, *Part. Part. Syst. Charact.* **2014**, *31*, 342.

[42] M. Meudt, T. Jakob, A. Polywka, L. Stegers, S. Kropp, S. Runke, M. Zang, M. Clemens, P. Görrn, *Adv. Mater. Technol.* **2018**, *3*, 1800124.

[43] A. Polywka, C. Tückmantel, P. Görrn, *Sci. Rep.* **2017**, *7*, 45144.

[44] A. Polywka, T. Jakob, L. Stegers, T. Riedl, P. Görrn, *Adv. Mater.* **2015**, *27*, 3755.

[45] I. Shutsko, C. M. Böttge, J. Von Bargen, A. Henkel, M. Meudt, P. Görrn, *Nanophotonics* **2019**, *8*, 1457.

[46] I. Shutsko, M. Buchmüller, M. Meudt, P. Görrn, *Adv. Opt. Mater.* **2022**, *10*, 2102783.

[47] I. Shutsko, M. Buchmüller, M. Meudt, P. Görrn, *Adv. Mater. Technol.* **2022**, *7*, 2200086.

[48] Y. Xu, P. Bai, X. Zhou, Y. Akimov, C. E. Png, L. K. Ang, W. Knoll, L. Wu, *Adv. Opt. Mater.* **2019**, *7*, 1801433.

[49] A. Talbi, S. Kaya-Boussougou, A. Sauldubois, A. Stolz, C. Boulmer-Leborgne, N. Semmar, *Appl. Phys. A Mater. Sci. Process.* **2017**, *123*, 463.

[50] M. Huang, F. Zhao, Y. Cheng, N. Xu, Z. Xu, *ACS Nano* **2009**, *3*, 4062.

[51] A. J. Pedraza, J. D. Fowlkes, D. A. Blom, H. M. Meyer, *J. Mater. Res.* **2002**, *17*, 2815.

[52] L. Novotny, B. Hecht, *Principles of Nano-Optics*, Cambridge University Press, **2006**.

[53] K. Kołątaj, J. Krajczewski, A. Kudelski, *Environ. Chem. Lett.* **2020**, *18*, 529.

[54] B. T. Draine, J. C. Weingartner, *Astrophys. J.* **1996**, *470*, 551.

[55] O. M. Maragò, P. H. Jones, P. G. Gucciardi, G. Volpe, A. C. Ferrari, *Nat. Nanotechnol.* **2013**, *8*, 807.

[56] K. L. Kelly, E. Coronado, L. L. Zhao, G. C. Schatz, *J. Phys. Chem. B* **2003**, *107*, 668.

[57] H. Raether, *Surface Plasmons on Smooth and Rough Surfaces and on Gratings*, Springer, **1988**.

[58] F. Abeles, T. Lopez-Rios, in *Mod. Probl. Condens. Matter Sci.*, North-Holland Publishing Company, **1982**.

[59] J. D. Jackson, *Classical Electrodynamics*, John Wiley & Sons, Inc., **1962**.

[60] C. Rizal, S. Pisana, I. Hrvoic, *Photonics* **2018**, *5*, 15.

[61] P. Berini, *Adv. Opt. Photonics* **2009**, *1*, 484.

[62] F. Liu, Y. Rao, Y. D. Huang, W. Zhang, J. De Peng, *Chinese Phys. Lett.* **2007**, *24*, 3462.

[63] M. Bera, M. Ray, *5th Int. Conf. Comput. Devices Commun.* **2012**, *3*, 1.

[64] V. K. Sharma, *Eng. Res. Express* **2021**, *3*, 035039.

[65] F. Yang, J. R. Sambles, G. W. Bradberry, *Phys. Rev. B* **1991**, *44*, 5855.

[66] L. Brigo, E. Gazzola, M. Cittadini, P. Zilio, G. Zacco, F. Romanato, A. Martucci, M. Guglielmi, G. Brusatin, *Nanotechnology* **2013**, *24*, 155502.

[67] M. Lorente-Crespo, C. Mateo-Segura, *IEEE Photonics J.* **2016**, *8*, 1.

[68] Q. Liu, J. S. Kee, M. K. Park, *IEEE Photonics Technol. Lett.* **2013**, *25*, 1420.

[69] T. Søndergaard, V. Siahpoush, J. Jung, *Phys. Rev. B - Condens. Matter Mater. Phys.* **2012**, *86*, 085455.

[70] D. J. Griffiths, *Introduction to Electrodinamic*, Prentice-Hall, **1999**.

[71] V. Serov, *Fourier Series, Fourier Transform and Their Applications to Mathematical Physics*, Springer, **2017**.

[72] I. Juvells, S. Vallmitjana, A. Carnicer, J. Campos, *Am. J. Phys.* **1991**, *59*, 744.

[73] S. Arunachalam, S. M. Khairnar, B. S. Desale, *Appl. Math. Sci.* **2015**, *9*, 2221.

[74] E. O. Brigham, *The Fast Fourier Transform and Its Applications*, Prentice-Hall, **1988**.

[75] M. R. Langille, M. L. Personick, C. A. Mirkin, *Angew. Chemie - Int. Ed.* **2013**, *52*,

13910.

[76] J. Zhang, S. Li, J. Wu, G. C. Schatz, C. A. Mirkin, *Angew. Chemie - Int. Ed.* **2009**, *48*, 7787.

[77] C. Zhan, M. Moskovits, Z. Q. Tian, *Matter* **2020**, *3*, 42.

[78] C. Zhang, J. Qi, Y. Li, Q. Han, W. Gao, Y. Wang, J. Dong, *Nanomaterials* **2022**, *12*, 1329.

[79] H. Manoharan, D. Kc, V. V. R. Sai, *Plasmonics* **2020**, *15*, 51.

[80] L. V. Besteiro, A. Movsesyan, O. Ávalos-Ovando, S. Lee, E. Cortés, M. A. Correa-Duarte, Z. M. Wang, A. O. Govorov, *Nano Lett.* **2021**, *21*, 10315.

[81] V. K. La Mer, *Ind. Eng. Chem.* **1952**, *44*, 1270.

[82] N. T. K. Thanh, N. Maclean, S. Mahiddine, *Chem. Rev.* **2014**, *114*, 7610.

[83] A. Paul, B. Kenens, J. Hofkens, H. Uji-i, *Langmuir* **2012**, *28*, 8920.

[84] P. Sutter, Y. Li, C. Argyropoulos, E. Sutter, *J. Am. Chem. Soc.* **2017**, *139*, 6771.

[85] A. J. Haes, C. L. Haynes, A. D. Mcfarland, G. C. Schatz, *Mater. Res. Bull.* **2005**, *30*, 368.

[86] V. Amendola, O. M. Bakr, F. Stellacci, *Plasmonics* **2010**, *5*, 85.

[87] H. Guo, L. He, B. Xing, *Environ. Sci. Nano* **2017**, *4*, 2093.

[88] Eric C. Le Ru, P. G. Etchegoin, *Principles of Surface-Enhanced Raman Spectroscopy*, Elsevier, **2009**.

[89] K. M. Mayer, J. H. Hafner, *Chem. Rev.* **2011**, *111*, 3828.

[90] A. Shalabney, I. Abdulhalim, *Laser Photonics Rev.* **2011**, *5*, 571.

[91] J. Homola, S. S. Yee, G. Gauglitz, *Sensors Actuators, B Chem.* **1999**, *54*, 3.

[92] S. Torquato, *Phys. Rev. E* **2016**, *94*, 022122.

[93] Z. Ma, S. Torquato, *J. Appl. Phys.* **2017**, *121*, 244904.

[94] D. Chen, S. Torquato, *Acta Mater.* **2018**, *142*, 152.

[95] R. Lin, V. Mazzone, N. Alfaraj, J. Liu, X. Li, A. Fratalocchi, *Laser Photonics Rev.* **2020**, *14*, 1800296.

[96] R. D. Batten, F. H. Stillinger, S. Torquato, *J. Appl. Phys.* **2008**, *104*, 033504.

[97] C. E. Zachary, Y. Jiao, S. Torquato, *Phys. Rev. Lett.* **2011**, *106*, 178001.

[98] C. E. Zachary, Y. Jiao, S. Torquato, *Phys. Rev. E* **2011**, *83*, 051308.

[99] J. Kim, S. Torquato, *Phys. Rev. E* **2019**, *99*, 052141.

[100] J. Kim, S. Torquato, *Phys. Rev. E* **2021**, *103*, 012123.

[101] S. Torquato, *J. Phys. Condens. Matter* **2016**, *28*, 414012.

[102] T. Jakob, A. Polywka, L. Stegers, E. Akdeniz, S. Kropp, M. Frorath, S. Trost, T. Schneider, T. Riedl, P. Görrn, *Appl. Phys. A Mater. Sci. Process.* **2015**, *120*, 503.

[103] S. Möllenbeck, N. Bogdanski, H. C. Scheer, J. Zajadacz, K. Zimmer, *Microelectron. Eng.* **2009**, *86*, 608.

[104] C. Steinberg, K. Dhima, D. Blenskens, A. Mayer, S. Wang, M. Papenheim, H. C. Scheer, J. Zajadacz, K. Zimmer, *Microelectron. Eng.* **2014**, *123*, 4.

[105] M. R. Ammar, G. Legeay, A. Bulou, J. F. Bardeau, *Liris.Cnrs.Fr* **2005**, 3.

[106] K. Dhima, C. Steinberg, A. Mayer, S. Wang, S. Möllenbeck, H. C. Scheer, *Microelectron. Eng.* **2012**, *100*, 37.

[107] Y. Saito, J. J. Wang, D. A. Smith, D. N. Batchelder, *Langmuir* **2002**, *18*, 2959.

[108] G. Frens, *Nat. Phys. Sci.* **1973**, *241*, 20.

[109] J. Turkevich, P. C. Stevenson, J. Hillier, *Discuss. Faraday Soc.* **1951**, *11*, 55.

[110] J. J. Fendley, *Phys. Educ.* **1982**, *17*, 209.

[111] S. S. Leong, W. M. Ng, J. K. Lim, S. P. Yeap, in *Handb. Mater. Charact.*, **2018**, pp. 77–111.

[112] T. W. M. Jin, F. Thomsen, T. Skrivanek, in *Adv. Contact Angle, Wettability Adhes.*, **2006**, pp. 419–437.

[113] B. T. Draine, P. J. Flatau, *J. Opt. Soc. Am. A* **1994**, *11*, 1491.

[114] J. C. Draine, B. T. & Weingartner, *Astrophys. J.* **1996**, *470*, 551.

[115] L. Roach, A. Hereu, P. Lalanne, E. Duguet, M. Tréguer-Delapierre, K. Vynck, G. L. Drisko, *Nanoscale* **2022**, *14*, 3324.

[116] J. Kim, S. Torquato, *Proc. Natl. Acad. Sci. U. S. A.* **2020**, *117*, 8764.

[117] D. Chen, E. Lomba, S. Torquato, *Phys. Chem. Chem. Phys.* **2018**, *20*, 17557.

[118] Z. Ma, S. Torquato, *Phys. Rev. E* **2019**, *99*, 022115.

[119] Y. A. Krutyakov, A. A. Kudrinskiy, A. Y. Olenin, G. V Lisichkin, *Russ. Chem. Rev.* **2008**, *77*, 233.

[120] V. Giannini, A. I. Fernández-Domínguez, Y. Sonnefraud, T. Roschuk, R. Fernández-García, S. A. Maier, *Small* **2010**, *6*, 2498.

[121] Z. Liu, G. Vitrant, Y. Lefkir, S. Bakhti, N. Destouches, *Phys. Chem. Chem. Phys.* **2016**, *18*, 24600.

[122] D. V. Goia, E. Matijević, *New J. Chem.* **1998**, *22*, 1203.

[123] L. Kvítek, R. Prucek, A. Panáček, R. Novotný, J. Hrbáč, R. Zbořil, *J. Mater. Chem.* **2005**, *15*, 1099.

[124] M. Chen, W. Ding, Y. Kong, G. W. Diao, *Langmuir* **2008**, *24*, 3471.

[125] M. H. Manghnani, A. Hushur, T. Sekine, J. Wu, J. F. Stebbins, Q. Williams, *J. Appl. Phys.* **2011**, *109*, 113509.

[126] T. A. Dolenko, S. A. Burikov, S. A. Dolenko, A. O. Efitorov, I. V. Plastinin, V. I. Yuzhakov, S. V. Patsaeva, *J. Phys. Chem. A* **2015**, *119*, 10806.

[127] J. Shao, M. Lin, Y. Li, X. Li, J. Liu, J. Liang, H. Yao, *PLoS One* **2012**, *7*, e48127.

[128] I. Delfino, C. Camerlingo, M. Portaccio, B. Della Ventura, L. Mita, D. G. Mita, M. Lepore, *Food Chem.* **2011**, *127*, 735.

[129] J. Kaminský, J. Kapitán, V. Baumruk, L. Bednárová, P. Bouř, *J. Phys. Chem. A* **2009**, *113*, 3594.

[130] G. Qi, Y. Wang, B. Zhang, D. Sun, C. Fu, W. Xu, S. Xu, *Anal. Bioanal. Chem.* **2016**, *408*, 7513.

[131] I. O. Osorio-Román, V. Ortega-Vá Squez, C. Victor Vargas, R. F. Aroca, *Appl. Spectrosc.* **2011**, *65*, 838.

[132] W. Man, M. Florescu, K. Matsuyama, P. Yadak, G. Nahal, S. Hashemizad, E. Williamson, P. Steinhardt, S. Torquato, P. Chaikin, *Opt. Express* **2013**, *21*, 19972.

[133] H. Altug, S. Oh, S. A. Maier, J. Homola, *Nat. Nanotechnol.* **2022**, *17*, 5.

[134] M. M. Mahan, A. L. Doiron, *J. Nanomater.* **2018**, *2018*, 5837276.

[135] K. Sztandera, B. Klajnert-maculewicz, *Mol. Pharm.* **2019**, *16*, 1.

[136] S. Siddique, J. C. L. Chow, *Appl. Sci.* **2020**, *10*, 3824.

[137] A. Lakhtakia, *Nanostructured Thin Film. IV* **2011**, *8104*, 810403.

[138] S. E. Swiontek, D. P. Pulsifer, A. Lakhtakia, *Tribut. to H. John Caulf.* **2013**, *8833*, 883309.

[139] H. Fadakar, A. Z. Nezhad, A. Borji, *9th Iran. Conf. Electr. Eng.* **2011**, 468.

[140] T. Maurer, P. M. Adam, G. Lévêque, *Nanophotonics* **2015**, *4*, 363.

[141] J. Becker, A. Trügler, A. Jakab, U. Hohenester, C. Sönnichsen, *Plasmonics* **2010**, *5*, 161.

[142] N. Liu, M. Mesch, T. Weiss, M. Hentschel, H. Giessen, *Nano Lett.* **2010**, *10*, 2342.

[143] J. Becker, A. Trügler, A. Jakab, U. Hohenester, C. Sönnichsen, *Plasmonics* **2010**, *5*, 161.

[144] J. Chen, F. Gan, Y. Wang, G. Li, *Adv. Opt. Mater.* **2018**, *6*, 1701152.

[145] Y. Gao, Z. Xin, B. Zeng, Q. Gan, X. Cheng, F. J. Bartoli, *Lab Chip* **2013**, *13*, 4755.

[146] B. D. Thackray, V. G. Kravets, F. Schedin, G. Auton, P. A. Thomas, A. N. Grigorenko, *ACS Photonics* **2014**, *1*, 1116.

[147] B. Liu, S. Chen, J. Zhang, X. Yao, J. Zhong, H. Lin, T. Huang, Z. Yang, J. Zhu, S. Liu, C. Lienau, L. Wang, B. Ren, *Adv. Mater.* **2018**, *30*, 1706031.

[148] B. Ai, P. Basnet, S. Larson, W. Ingram, Y. Zhao, *Nanoscale* **2017**, *9*, 14710.

[149] S. Kim, H.-M. Kim, Y.-H. Lee, *Opt. Lett.* **2015**, *40*, 5351.

[150] Z. L. Cao, S. L. Wong, S. Y. Wu, H. P. Ho, H. C. Ong, *Appl. Phys. Lett.* **2014**, *104*, 171116.

[151] Y. Shen, J. Zhou, T. Liu, Y. Tao, R. Jiang, M. Liu, G. Xiao, J. Zhu, Z. K. Zhou, X. Wang, C. Jin, J. Wang, *Nat. Commun.* **2013**, *4*, 2381.

[152] S. Safiabadi Tali, W. Zhou, *Nanophotonics* **2019**, *8*, 1199.

[153] E. Cao, W. Lin, M. Sun, W. Liang, Y. Song, *Nanophotonics* **2018**, *7*, 145.

[154] F. Bernal Arango, A. Kwadrin, A. F. Koenderink, *ACS Nano* **2012**, *6*, 10156.

[155] D. P. Cai, J. H. Lu, C. C. Chen, C. C. Lee, C. E. Lin, T. J. Yen, *Sci. Rep.* **2015**, *5*, 1.

[156] J. K. S. Poon, *Nat. Photonics* **2018**, *12*, 255.

[157] A. Callegari, D. Tonti, M. Chergui, *Nano Lett.* **2003**, *3*, 1565.

[158] M. José-Yacamán, C. Gutierrez-Wing, M. Miki, D. Q. Yang, K. N. Piyakis, E. Sacher, *J. Phys. Chem. B* **2005**, *109*, 9703.

List of Publications

[1] Buchmüller, M., Shutsko, I., Schumacher, S. O., and Görrn, P. "Harnessing Short-Range Surface Plasmons in Planar Silver Films via Disorder-Engineered Metasurfaces." ACS Applied Optical Materials **2023**, 1 (11), 1777-1782.

[2] Buchmüller, M., Shutsko, I., and Görrn, P. "Light-Controlled Disorder Engineering for Functional Optical Metasurfaces." 5th World Congress of Advanced Materials Science, Barcelona, Spain, **2023**.

[3] Shutsko, I., Buchmüller, M., Meudt, M., Görrn, P. "Light-Controlled Fabrication of Disordered Hyperuniform Metasurfaces." Adv. Mater. Technol. **2022**, 7, 2200086.

[4] Shutsko, I., Buchmüller, M., Meudt, M., Görrn, P. "Plasmon-Induced Disorder Engineering for Robust Optical Sensors." Adv. Optical Mater. **2022**, 10, 2102783.

[5] Pourdavoud, N., Häger, T., Mayer, A., Cegielski, P. J., Giesecke, A. L., Heiderhoff, R., Olthof, S., Zaefferer, S., Shutsko, I., Henkel, A., Becker-Koch, D., Stein, M., Cehovski, M., Charfi, O., Johannes, H.-H., Rogalla, D., Lemme, M. C., Koch, M., Vaynzof, Y., Meerholz, K., Kowalsky, W., Scheer, H.-C., Görrn, P., Riedl, T. "Room-Temperature Stimulated Emission and Lasing in Recrystallized Cesium Lead Bromide Perovskite Thin Films." Adv. Mater. **2019**, 31, 1903717.

[6] Shutsko, I., Böttge, C., von Bargen, J., Henkel, A., Meudt, M., Görrn, P. "Enhanced Hybrid Optics by Growing Silver Nanoparticles at Local Intensity Hot Spots." Nanophotonics, **2019**, Vol. 8, Issue 9, 1457-1464.

[7] Shutsko, I., Meudt, M., Polywka, A., Tückmantel, C., Görrn, P. "Light-Controlled Assembly of Silver Nanoparticles." NANOP International Conference, Rome, Italy, OS1b-1, **2018**.

[8] Hoffmann, L., Brinkmann, K. O., Malerczyk, J., Rogalla, D., Becker, T., Theirich, D., Shutsko, I., Görrn, P., Riedl T. "Spatial Atmospheric Pressure Atomic Layer Deposition of Tin Oxide as Impermeable Electron Extraction Layer for Perovskite Solar Cells with Enhanced Thermal Stability." ACS Applied Mater. & Interfaces **2018**, 10, 6006.

[9] Shutsko, I., Böttge, C., Meudt, M., Henkel, A., Hoffmann, T. H., Görrn, P. "Plasmon-Driven Alignment of Silver Nanoparticles." MRS Fall Meeting, Boston, USA, NM02.05.04, **2018**.

[10] Pourdavoud, N., Mayer, A., Buchmüller, M., Brinkmann, K., Häger, T., Hu, T., Heiderhoff, R., Shutsko, I., Görrn, P., Chen, Y., Scheer, H.-C., Riedl, T. "Distributed Feedback Lasers Based on MAPbBr3." Adv. Mater. Technol. **2018**, 3, 1700253.

[11] Riedl, T.J., Pourdavoud, N., Mayer, A., Häger, T., Heiderhoff, R., Shutsko, I., Scheer, H.C., Görrn, P. "Ultra-Smooth Perovskite Thin Films for Lasers." In Physical Chemistry of Semiconductor Materials and Interfaces XVII **2018**, Vol. 10724, p. 107240C.

[12] Becker, T., Trost, S., Behrendt, A., Shutsko, I., Polywka, A., Görrn, P., Reckers, P., Das, C., Mayer, T., Di Carlo Rasi, D., Hendriks, K. H., Wienk, M. M., Janssen, R. A. J., Riedl, T. "Adv. Energy Mater. **2018**, 8, 1702533.

[13] Sergeev, O.V., Neumüller, A., Shutsko, I., Vehse, M., Agert, C. "Doped Microcrystalline Silicon as Front Surface Field Layer in Bifacial Silicon Heterojunction Solar Cells." Energy Procedia. **2017**, 124, 371-378.

[14] Preissler, N., Töfflinger, J.A., Shutsko, I., Gabriel, O., Calnan, S., Stannowski, B., Rech, B., Schlatmann, R. "Interface Passivation of Liquid-Phase Crystallized Silicon on Glass Studied with High-Frequency Capacitance–Voltage Measurements." Phys. Status Solidi A **2016**, 213: 1697-1704.

[15] Tivanov, M., Shutsko, I. "New Optical Method for Determination of Refractive Index at the Edge of Absorption Zone for Semiconductor Thick Films." **2016**, Patent № 19962 C2 G 01N 21/00, 107-108.